

Energy Loss of Heavy Quarks Passing Hot Deconfined Matter

**Energieverlust schwerer Quarks
beim Durchlaufen von heisser Deconfinement-Materie**

Diplomarbeit
zur Erlangung des akademischen Grades
Diplom-Physiker

vorgelegt von
Henry Schade
geboren am 23. Dezember 1980 in Zittau

Institut für Theoretische Physik
Fachrichtung Physik
Fakultät für Mathematik und Naturwissenschaften
der Technischen Universität Dresden



Oktober 2006

Eingereicht am 9. 10. 2006

1. Gutachter: Prof. Dr. R. Schmidt
2. Gutachter: Prof. Dr. B. Kämpfer

Abstract

The radiation of gluons off heavy and light quarks passing through a deconfined and hot strongly interacting medium is calculated in various scenarios. The interaction of the jet-like quarks with the ambient deconfined medium is simulated either as scattering at a static Debye-potential or as quark-quark scattering. Perturbative processes of colliding on-shell quarks are evaluated on tree-level.

The focus is on energy loss in scalar QCD with regard to different medium modifications and kinematic parameters. Therefore, individual contributions to the single-gluon emission spectrum are considered; thereby, effects of interferences are included in detail. The relevance of different integration areas of the gluon emission spectrum is analysed and the phase space distribution is considered. Divergences and their attendance within the framework of screening described by effective parameters are discussed. In particular, the dead-cone effect for heavy quarks is outlined.

Kurzfassung

Die Abstrahlung von Gluonen beim Durchgang von schweren und leichten Quarks durch ein stark wechselwirkendes Medium wird in verschiedenen Szenarien berechnet. Dabei ist die Wechselwirkung von Jet-ähnlichen Quarks in einem umgebenden Medium im Deconfinement-Zustand entweder als Streuung von Quarks an einem statischen Debye-Potential oder als einfache Quark-Quark Streuung betrachtet worden. Die störungstheoretischen Prozesse kollidierender "on-shell" Quarks werden auf dem Niveau von Baumgraphen ausgewertet.

Das Hauptaugenmerk wird dabei im Rahmen der skalaren QCD auf den Energieverlust des einlaufenden Teilchens bezüglich verschiedener Medium-Modifikationen und kinematischer Parameter gelegt. Dazu werden einzelne Beiträge des Ein-Gluonemissionsspektrums hinsichtlich signifikanter Interferenzeffekte im Detail untersucht. Desweiteren wird auf die Relevanz verschiedener Integrationsbereiche des Gluonspektrums aufmerksam gemacht und Probleme bei der Behandlung des Phasenraums analysiert. Auftretende Divergenzen und deren Behandlung im Rahmen einer Abschirmung durch effektive Parameter werden diskutiert, wobei dem "dead-cone" Effekt für schwere Quarks besonderer Bedeutung zuteil wird.

Contents

1	Introduction	7
1.1	The QCD phase diagram	7
1.2	Relativistic Heavy-Ion Collisions	9
1.3	Quark-Gluon Plasma	9
1.4	Jet Quenching	10
1.4.1	Experimental Background	10
1.4.2	Theoretical Ideas	12
1.5	Outline of the Thesis	15
2	Scattering Processes in Deconfinement Matter	17
2.1	Cross Section and Radiation Amplitude	17
2.2	Quark-Quark Scattering	18
2.3	The Potential Model	20
2.4	Multiple Scattering: The Landau-Pomeranchuk-Migdal (LPM) Effect	21
2.5	Ter-Mikaelian (TM) Effect	27
3	Single Quark Scattering	29
3.1	Kinematics for Potential Model with One-Gluon Emission	29
3.1.1	Elastic Potential Scattering	30
3.1.2	Inelastic Potential Scattering	31
3.2	QCD Radiation Amplitude	34
3.2.1	Abelian Contributions	35
3.2.2	Non-Abelian Contributions	37
3.3	Dead Cone Factor with In-Medium Extension	40
3.4	Kinematic Corrections	41
3.5	Gunion-Bertsch Limit of Quark-Quark Scattering	44
4	Radiative Energy Loss	47
4.1	Divergences	47
4.2	Gluon Distribution	50
4.3	Average Energy Loss	51
4.3.1	Definition	51
4.3.2	Integration over Phase Space Distribution	55
4.4	The Running Coupling Constant	62
4.5	Radiative vs. Collisional Energy Loss	64
5	Summary and Outlook	69

Appendices	70
A Notation and Conventions	71
B Light-cone Variables, Dirac Matrices and Spinors	73
B.1 Light-cone Variables	73
B.2 Dirac Matrices and Spinors	73
C Colour Algebra in QCD	75
D Feynman Rules	79
E Scalar QCD versus Spinor Calculation	83
F General Aspects of Gauges	85
F.1 Gauge Invariance for Polarisation Vectors	85
F.2 Linear and Circular Polarisations	87
F.3 Gauge Invariance of the Gluon Propagator	87
G Numerical Integration and C++ Code	89
Bibliography	91

1 Introduction

Modern physics provides us two fundamental concepts: On one hand the standard model of particle physics with the principle of local gauge invariance, on the other hand the Big Bang cosmology on the basis of the principles of general relativity. Up to now, it is an open question what happened at the very beginning of the universe. In this first few microseconds after the birth of the universe, a primordial kind of matter, called quark-gluon plasma (QGP) dominates this phase of evolution.

The fundamental theory for describing the dynamics of strongly interacting elementary particles, the quarks (spin- $\frac{1}{2}$ fermions) and gluons, is perceived to be quantum chromodynamics (QCD). Nuclear matter in ground state consists of protons and neutrons, belonging to the group of hadrons, which mainly interact strongly. Protons and neutrons consist of a mixture of quarks and gluons. These latter elementary particles are often named as partons. The quarks exist in six different types or so-called flavours. These flavours are combined in three families or generations of quarks. The first family consists of the up and down quarks, the second one is built of charm and strange flavours, and in the third top and bottom quarks form the third family, which are classified by their different electronic charges and masses. In contrast to the theory of electromagnetic interaction (QED), QCD belongs to non-Abelian gauge theories. Interactions of quarks are mediated by the exchange of spin-1 bosons named gluons, which carry colour charges. Thus, they can interact with each other, contrary to gauge bosons of the QED (photons). Additionally, quarks carry three colour charges, nicknamed by the fundamental colours in nature: red, green and blue. Actually, those are the three states of the fundamental representation of the colour gauge group $SU(3)_c$. The gluons obey the adjoint representation of $SU(3)_c$, i.e. they appear in eight colour states. A noteworthy peculiar fact is the confinement of quarks. It means that quarks can not exist alone - they always need at least one partner with opposite colour charge to form a colour singlet. Such quark-antiquark pairs ($q\bar{q}$) are called mesons. It is also possible for quarks to combine in triple states as baryons (qqq) and exotic multiquark states, pentaquark ($uudd\bar{s}$) for instance. All multiple quark-states follow the rule of colourless combinations. Similarly, composites of gluons - glue balls - must be colourless, too. Another important feature of QCD is asymptotic freedom, meaning that the interaction of quarks and gluons at high energies or small interparticle spacing becomes weak.

1.1 The QCD phase diagram

Now we consider various special conditions of strongly interacting matter, e.g. comparable to those in the early universe, shortly after Big Bang, or in the core of superdense stars. QCD suggests a phase transition of ordinary hadron matter made of pions, kaons, etas,

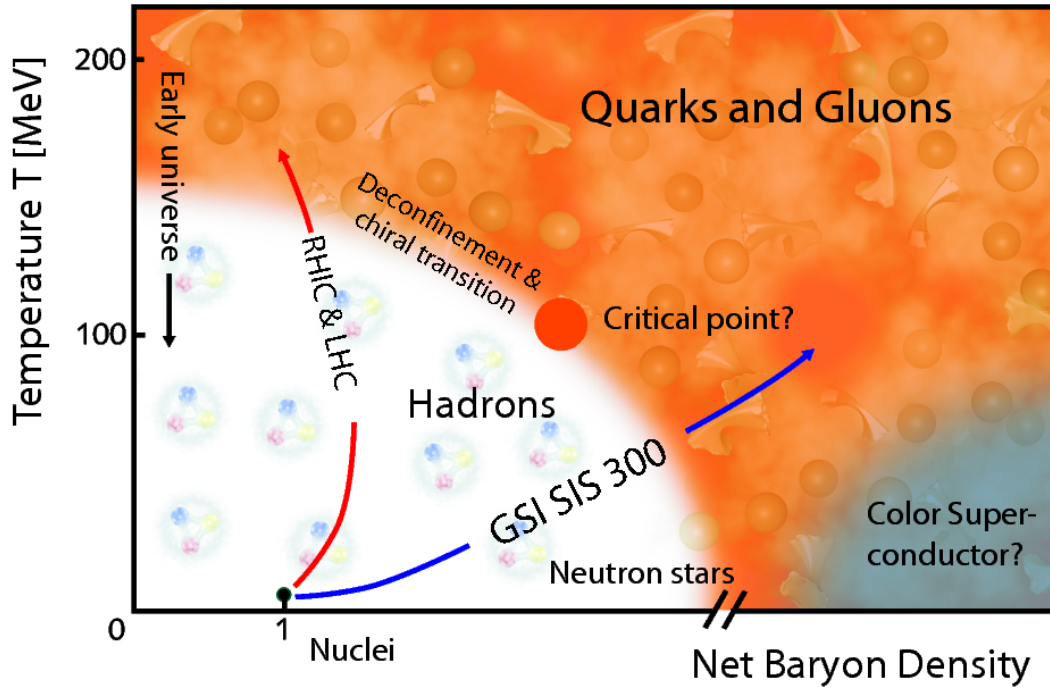


Figure 1.1: Schematic plot of the QCD phase diagram of strongly interacting matter. From [GS11].

neutrons and protons etc. to a hot plasma of quarks and gluons, for temperatures larger than 10^{12} K, and to a cold QGP for densities larger than 10^{12} $\text{kg} \cdot \text{cm}^{-3}$. This behaviour of nuclear matter is sketched in Fig. 1.1 in a plane of temperature T versus net baryon density. For increasing temperature and/or baryon density the quarks and gluons becomes the relevant degrees of freedom, while at lower temperature and density, hadrons are the important building blocks of strongly interacting matter. The details of this transition from the confined phase of strongly interacting matter to the QGP phase are still matter of debate. The order of phase transition is possibly first, second or a crossover (i.e. no phase transition at all), depending on the quark masses and the number of active quark flavours. The transition from the confinement to the deconfinement area is marked in Fig. 1.1 as transition from white to orange. Particularly interesting is the possible existence of a critical point where a line of first-order phase transition ends.

The transition between hadronic matter and QGP can also be characterised by chiral symmetry. It is spontaneously broken in both vacuum and nuclear matter under normal conditions. For high temperatures and densities the chiral condensate $\langle \bar{\psi}\psi \rangle$ is approximately zero or, in other words, the chiral symmetry is restored assuming the light quark masses vanish. The expectation value of the chiral condensate, $\langle \bar{\psi}\psi \rangle$, is an order parameter of chiral phase transition. The pseudo-critical temperature separates the confined phase and the deconfinement area at baryon chemical potential $\mu = 0$. It is also determined by a rapid change of the expectation value of the Polyakov loop. An evaluation by lattice theory yields that the temperatures of these two effects might fall together for vanishing net baryon densities.

For regions of low temperatures and very high densities one expects a colour-superconducting phase with quark Cooper pairs.

1.2 Relativistic Heavy-Ion Collisions

With the aim of investigating the QCD phase diagram (Fig. 1.1) at high net baryon densities and temperatures, especially chiral symmetry restoration and deconfinement transition, many heavy-ion programs have been carried out. In 1987, the Alternating Gradient Synchrotron (AGS) started at Brookhaven National Laboratories (BNL), New York, reaching heavy-ion beams of energy in the range 10 - 15 AGeV¹. In Europe, CERN (Conseil Européen pour la Recherche Nucléaire) puts the Super Proton Synchrotron (SPS) into operation. Since 1994, after a modification for accelerating heavy ions, beam energies up to 200 AGeV were available for the first time. Furthermore, at BNL with the Relativistic Heavy Ion Collider (RHIC), the first heavy-ion collider, Au+Au collisions at centre-of-mass (CMS) energies² of 200 AGeV were achieved.

Presumably in 2007, experiments with very high energies of $\sqrt{s_{NN}} = 5.6$ TeV, provided by Pb+Pb collisions, will start out at the Large Hadron Collider (LHC), which is under construction in the previous LEP (Large Electron-Positron collider) tunnel at CERN, Geneva.

Around 2010, the new accelerator complex FAIR (Facility for Antiproton and Ion Research) will be set in operation at GSI (Gesellschaft für Schwerionenforschung) in Darmstadt, Germany. The CBM (Compressed Baryon Matter) experiment is part of the FAIR project. Among the primary goals are searching for the origin of mass of hadrons and matter in a region near to or covering the QGP. A part of FAIR is a synchrotron facility named SIS300, which operates in contrast to RHIC and LHC in an intermediate energy range, thus reaching also intermediate temperatures but aiming at achieving maximum baryon densities.

1.3 Quark-Gluon Plasma

The transition from hadronic matter to a quark-gluon and vice versa is fairly fascinating, in particular, if it would be a phase transition. To explore this novel state of strongly interacting matter in the laboratory, the above mentioned heavy-ion experiments have been or will be performed. The intriguing question was and still is, what is a unique signature of the quark-gluon plasma. First ideas were guided by the asymptotic freedom of QCD and relied on pictures of nearly non-interacting quarks and gluons. The new experiment series at RHIC resulted in an opposite view: the quark-gluon plasma is strongly coupled, at least under conditions achieved at RHIC. The hydrodynamical flow pattern observed for many hadron species, for instance, supports strongly such a picture. However, hadrons emerge from the plasma by hadronisation; only the 'partonic flow' of the primordial plasma is imprinted to the subsequently formed hadrons. A more direct probe is looked for. As such, photons and dileptons may serve. These do not participate in the strong interaction but leave the strongly interacting matter, in particular the early plasma, undisturbed. Over many years, these penetrating probes have been considered as promising tools for a plasma diagnostics. Unfortunately, the electromagnetic signals are convolutions over the full time evolution of the matter in heavy-ion collisions, and it is fairly difficult (and even

¹We follow the usual convention for an indication of energy per nucleon with an 'A'.

²Henceforth, CMS energies per nucleon pair is denoted as $\sqrt{s_{NN}}$ for convenience.

model dependent) to disentangle plasma radiation from real and virtual photons emitted from the later hadronic stages; additionally, hard initial (Drell-Yan like) processes also contribute to the full spectra.

1.4 Jet Quenching

Among further signals from the plasma is 'jet-quenching'. The underlying idea is as follows. In the very first state of the high-energy heavy-ion collisions, hard processes create quarks and gluons with large transverse momenta. The latter ones stem from a kinematical reshuffling from the longitudinal momenta to the transverse momenta in quasi-free parton-parton scatterings. Such hard processes are rare. The transversally moving jet-like partons are surrounded by strongly interacting matter in heavy-ion collisions. There are various hints that the strongly interacting matter surprisingly fast thermalises and constitutes the QGP. That means, the jet traverses the plasma. When coming near the boundary, the parent jet parton hadronises and continues moving outwards. The jet, before hadronising, may undergo interactions with the ambient strongly interacting matter produced in soft processes. The general expectation is that a jet traversing a deconfined medium (quark-gluon plasma) experiences another interaction with the ambient medium than a jet propagating through confined (hadron) matter. This is the qualitative picture of jet tomography. Once knowing the jet modification one can diagnose the medium created in high-energy heavy-ion collisions.

The basic feature of the described scenario of jet quenching has been experimentally confirmed at RHIC: In a deuteron-gold collision, where no QGP with large space-time extent is expected, the jet properties differ substantially from those in a gold-gold collision, where the creation of a plasma is generally believed to happen. Once the basic properties are clarified, one proceeds to study in more detail the beam energy dependence, the system size and centrality dependence etc. A further interesting aspect for such a systematic investigation is the mass dependence of the parent jet quark. This is the major topic of this thesis. Before presenting a few theoretical ideas, let us survey the experimental situation.

1.4.1 Experimental Background

Besides the PHENIX collaboration at RHIC, the STAR group measures electrons and positrons from heavy flavour decays in Au+Au collisions as well as for p+p collisions at $\sqrt{s_{NN}} = 200$ GeV. Thus, one can introduce a so-called nuclear modification factor in order to characterise the medium-induced suppression of high p_T -electrons

$$R_{AA} = \frac{dN_{Au+Au}}{\langle T_{AA} \rangle d\sigma_{p+p}}, \quad (1.1)$$

which compares the production of electrons in AA collisions with those from pp collisions. Here, the integral $\langle T_{AA} \rangle$ stands for the average number of inelastic nucleon-nucleon collisions in a given centrality class. Note that the definition of R_{AA} is general; it is used for many other particle species and their momentum dependencies. Here we focus on 'non-photon electrons' which is a short hand notation for inclusive electrons and positrons after removal of unwanted sources from light mesons.

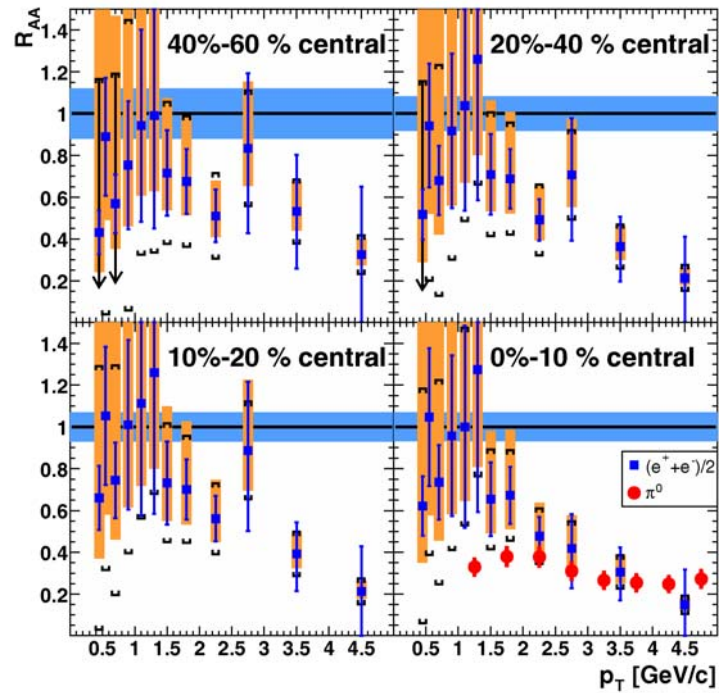


Figure 1.2: The nuclear modification factor R_{AA} for electrons from heavy quark flavour non-photonic decays as a function of the measured electron transverse momentum $p_T \equiv p_{\perp}$ (blue boxes) perpendicular to the heavy-ion collision axis in Au+Au collisions at RHIC $\sqrt{s_{NN}} = 200$ GeV for different centrality classes. We take our focus on the most central collisions, which are shown in the lower right hand panel, albeit the data for small peripheral collisions differs not significantly. The figure is taken from [Adl06a].

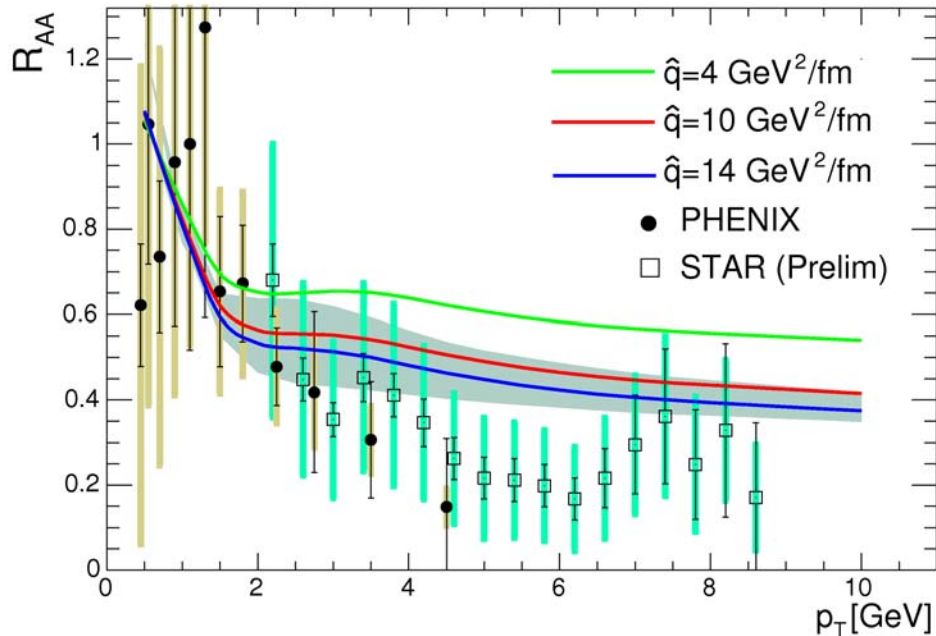


Figure 1.3: Central Au+Au collisions at RHIC for $\sqrt{s_{NN}} = 200$ GeV: R_{AA} for heavy-flavoured electrons from [Wie06]. A suppression at $p_T \geq 4$ GeV compared with theoretical estimates (solid lines) for different parton-averaged transport coefficients \hat{q} is obvious. The shaded band indicates the theoretical uncertainty of the perturbative baseline for $\hat{q} = 14$ GeV²/fm.

This factor R_{AA} is exhibited in Fig. 1.3 for non-photonic electrons for quenched heavy quark (charm and bottom) jets, comparing PHENIX and preliminary STAR data in central Au+Au reactions at 200 GeV³. A nuclear modification factor $R_{AA} < 1$ is shown over the whole range of electron transverse momenta, which provides a clear evidence for strong medium effects. Additionally, it is easy to see that a significant discrepancy between the experimental data and the theoretical prediction is observed in the region $p_T \sim 4 - 8$ GeV. One can try to solve this problem of strong suppression of the heavy-quark decay electrons by 'filling the gap' between theoretical estimates and experimental data by a greater heavy quark energy loss probability. This it is outlined in the next section.

Jet quenching is a generic feature in hadron spectra at RHIC energies. To demonstrate this, we exhibit in Fig. 1.4 the transverse momentum spectra of identified \bar{p} , π^- , Λ , K_s^0 . With increasing centrality, the spectra become steeper, meaning a reshuffling of high momentum hadrons towards lower momenta. While the spectra shown in Fig. 1.4 are primarily meant to highlight a particularity of mesons versus baryons, they can be used to construct the corresponding R_{AA} for various hadrons. The latter ones exhibit the suppression similar to that in Fig. 1.3.

The shown transverse momentum spectra (Fig. 1.4) are for hadrons composed of u, d and s quarks. Correspondingly, one expects that the parent partons are also such quarks, i.e. such ones which are also created in softer processes. As strangeness seems to stay near to chemical equilibrium at RHIC energies, these quark flavours can be contrasted as 'normal' constituents of matter. The next heavier quark species, charm, however is created, according to most estimates, only in initial hard processes. In so far, charm may serve as distinct probe with a well defined production process. Besides charmed baryons, charm may combine with u, d quarks and s quarks as well forming D and D_s mesons. D mesons need special identification tools. One possibility is their semi-leptonic decay, e.g. $D^+ \rightarrow e^+ + \text{anything}$ which has the large branching ratio of 17.2 %. These decay electrons or positrons are measurable indirectly by subtracting the other sources which are supposed to be known. In present terminology, charm mesons are attributed to 'non-photonic sources', as mentioned above. The decay electrons and positrons are intimately related to the kinematics of the parent charm mesons. In this way, valuable information on the momentum space distribution of charm meson can be gained.

1.4.2 Theoretical Ideas

Let us now concentrate on the framework for the treatment of jet quenching for D mesons. The quenched lepton spectra are calculated from the generic convolution

$$E_e \frac{d^3\sigma(e)}{dp^3} = E_i \frac{d^3\sigma(Q)}{dp_i^3} \otimes P(E_i \rightarrow E_f) \otimes D(Q \rightarrow H_Q) \otimes f(H_Q \rightarrow e) \quad (1.2)$$

in a perturbative QCD framework, as mentioned in [Wic06]. Here, e denotes the spectral electron and H_Q stands for the hadronised quark. Furthermore, the first term is the initial quark spectrum created in hard processes. The fragmentation of a quark to a hadron is described by the function $D(Q \rightarrow H_Q)$ and is convoluted with the hadron decay function $f(H_Q \rightarrow e)$. This describes the production process of the finally detected electron. If

³At LHC energies of 5.5 TeV, heavy quark decays are expected to dominate the electron spectrum up to $p_T \approx 30 - 35$ GeV, where W decay contributions take over.

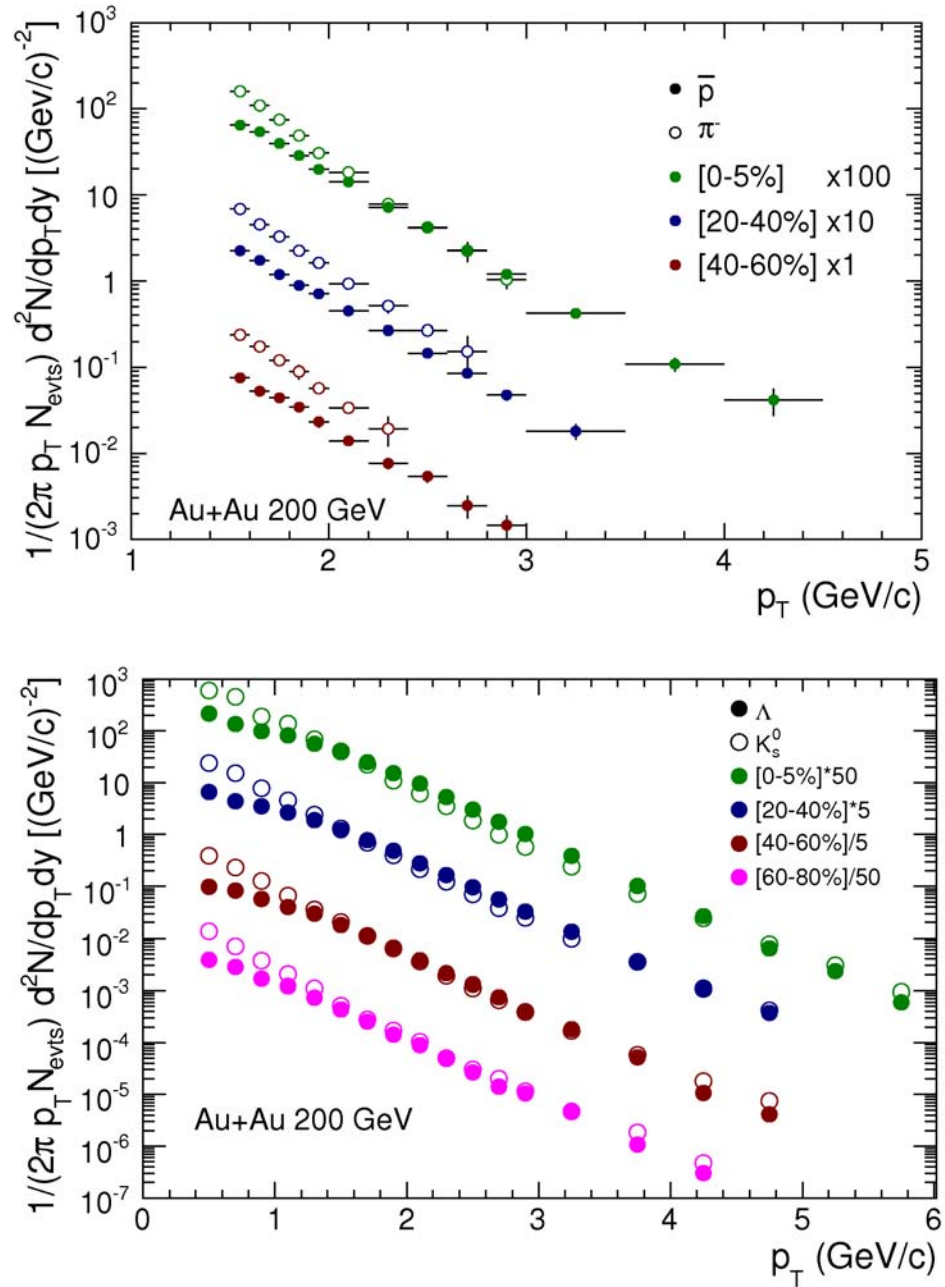


Figure 1.4: Upper panel: \bar{p} (full symbols) and π^- (open symbols) spectra as a function of both centrality and low transverse momentum p_T , produced in Au+Au collisions at $\sqrt{s_{NN}} = 200$ GeV. Lower panel: The same as in the upper panel, but for the hadrons Λ (full symbols) and K_s^0 (open symbols). The figure is taken from the STAR collaboration [Ada06] which shows that jet quenching increases with centrality.

we approximate the important energy loss probability by fixing the effective quark path length L it yields according to [Wic06]

$$P(E_i \rightarrow E_f; L) \approx P_{rad}(E_i \rightarrow E_f; L) \otimes P_{el}(E_i \rightarrow E_f; L), \quad (1.3)$$

meaning jet quenching is performed via two independent branching processes. In this context P_{rad} is the energy loss probability for the radiation process while P_{el} describes the collisional energy loss probability. Now, we concentrate only on the radiative energy loss, albeit the recent works ([Ala06, Djo06b]) predict a more involved situation: another dependence: The corresponding STAR and PHENIX data [Bie05, Adl06a, Adl06b, Adl06c] seem to falsify the assumption that heavy quark energy loss is dominated by radiative energy loss alone when the bulk QCD parton matter is constrained by the observed $dN/dy \approx 1000$ rapidity density of produced hadrons. Despite this restriction, our aim is the investigation of the radiative part of heavy quark energy loss in Eq. (1.3) with the help of a C++ program for taking into account the precise kinematic of inelastic scattering processes.

Recently, some approximations are developed to deal with the problem of radiative energy loss of a jet parton; all basing on the potential model which was introduced by Gyulassy and Wang [Gyu94, Wan95] (see also Section 2.3 in this thesis).

We shortly present two different analytical limits and elucidate their key ideas. They differ in their assumptions for the density of the deconfined medium, encoded in the mean number of jet's scatterings. It is also termed as the opacity of the medium $\bar{n} = L/\lambda$ with L as its traversed size, and λ denotes the average mean free path of the parton. The first approach of thick media ($\bar{n} \gg 1$) was given by Baier, Dokshitzer, Mueller, Peigné and Schiff (BDMPS) in [Bai98]. They found an ansatz firstly for a static medium but later they generalised this for expanding matter according to Bjorken's hydrodynamical model which yields a higher energy loss compared to the non-expanding medium. This estimate of energy loss - with the restriction to the high-energy limit - is growing with the square of the medium thickness L , but it is independent of the initial parton energy.

In contrast to this, Gyulassy, Levai and Vitev (GLV) developed an approach for thin media in the high-energy eikonal approximation, meaning an assumed parton which remains on a straight-line trajectory to evaluate all relevant diagrams recursively for an arbitrary number of elastic and inelastic scatterings. This recursion is carried out via a reaction operator, which is worked out in [Gyu00a, Gyu00b, Gyu01, Gyu02, Wie00]. Additionally, the GLV formalism considers the interaction of the parton's production amplitude what makes it difficult to compare with our numerical results without interference effects according to the production process.

But in the combination with the Landau-Pomeranchuk-Migdal effect, outlined in Section 2.4, only the first order of the opacity expansion is sufficient for determining basically the radiative energy loss. This is based on the reduction of the mean number of scatterings to an efficient value, respectively the rapid convergence of the opacity expansion. So, the induced energy loss reads in first order of opacity

$$\Delta E_{GLV}^{(1)} = \frac{C_R \alpha_s \mu_D^2}{N(E_i) \lambda_g} \cdot L^2 \cdot \log \frac{E_i}{\mu_D} \quad (1.4)$$

with C_R as a colour factor, μ_D denotes the Debye screening mass, α_s is the strong coupling constant and λ_g describes the mean free path length of a gluon. E_i stands for the initial energy of the parton, and it yields for the numerical factor $N(E_i) \rightarrow 4$ in the limit of

$E_i \rightarrow \infty$, as shown in [Gyu00b]. The proportionality of $\log(E_i)/E_i$ to the fractional energy loss causes a decrease for higher initial energies. Including finite kinematic boundaries, may cause $N(E_i)$ to deviate considerably from this asymptotic value. Another possible access to the problem of radiative energy loss is given by Zakharov in [Zak98] by using the path integral approach.

1.5 Outline of the Thesis

Given the above motivation, the goal of this thesis is to investigate the influence of the parent quark mass on jet attenuation in a deconfined hot medium. To simplify the following consideration we consider only a part of the full jet physics schematically depicted in Eq. (1.2), i.e. we focus on the section as $P(E_i \rightarrow E_f)$. That means, we cut out the energy loss of a quark when traversing the medium. By separating the jet creation process we also neglect the initial virtuality and interference effects with the production, i.e. the jet quarks are assumed to be on-shell and are created in the far past. We furthermore do not consider the hadronisation and possible subsequent semi-leptonic decay. Of course, these are severe simplifications which need to be improved in a realistic treatment of the complete process. In restricting ourselves on the idealised process of energy loss by gluon radiation we hope to isolate most clearly the mass effect of the parent jet quark. Along this line, we are going to contrast the gluon radiation of light and heavy quarks. Even the radiation process itself is highly simplified: We consider here only the one-gluon emission, again with the motivation of exploring a first step towards a more realistic description but with the hope to highlight most transparently the quark mass effect.

Since gluon emission in our scenario must be induced by an interaction with the ambient medium we deal here also with a schematic model widely used in previous literature: The surrounding medium is modelled as a colour scattering centre. As step towards a more realistic description we compare the scattering at a static centre with a scattering on a dynamical quark taking into account recoil effects and gluon emission from the scattering partner.

In contrasting gluon emission from light and heavy jet-like quarks [Dok06], our presentation is heavily guided by the discussion of the dead cone effect. Since we consider here the exact kinematics, within the given other idealisations, we can quantify to which extend the global dead cone suppression factor from [Dok01] is justified in a tree-level, on-shell description of the induced single-gluon emission process.

The thesis is organised as follows. In Chapter 2 we investigate various scattering events with single-gluon emission in the background of a surrounding deconfined medium. The basic instruments to handle scattering processes - the differential cross section and the radiation amplitude - are introduced at first. Always with the restriction of single quark scattering, we take our attention on quark-quark scattering and compare it with the simplified potential model by Gyulassy and Wang [Gyu94, Wan95]. Finally in this chapter, we study multiple scatterings in successive stages (LPM effect) from an electromagnetic point of view, and later on we focus on the medium polarisation (TM effect), i.e. the emitted photon is affected. This is to elucidate similarities and differences of Abelian and non-Abelian gauge theories.

The next Chapter 3 provides the kinematical framework by calculating the radiation amplitude for the elastic and inelastic scattering. We evaluate the QCD radiation ampli-

tude for Abelian and non-Abelian contributions, which contain of the full colour structure. Kinematical limits by means of analytical approaches, e.g. soft gluons and massless quarks, lead us to an approach for the radiation amplitude by Gunion and Bertsch [Gun82]. In order to remedy these analytical approximations, we give some suggestions in form of additional correction factors. A brief discussion of quark-quark scattering kinematic is given in the last section of this chapter.

The main goal of the thesis is represented in Chapter 4. It contains an evaluation of the radiative energy loss by launching our numerical calculation. This procedure includes the exact kinematics and colour algebra in contrast to other works (cf. [Gyu02, Käm00, Wie05, Xia04, Tho03]). In these previous works, various approaches are used in order to find full- or semi-analytical expressions for the averaged radiative energy loss. Furthermore, some details of multiple scatterings and opacity expansions are discussed with the aim of requiring the separation between the emitted gluon and the parton and considering a finite thickness of an amorphous medium. We illuminate aspects of the running coupling strength and compare radiative energy loss with the collisional ones at the end of this main chapter.

The conclusions can be found afterwards in Chapter 5. Technical details are relegated to appendices.

2 Scattering Processes in Deconfinement Matter

2.1 Cross Section and Radiation Amplitude

The differential cross section for scattering processes in the form of $1 + 2 \rightarrow n$ particles generally reads

$$d\sigma = d\beta |M|^2 \frac{(2\pi)^4 \delta^4 \left(p_1 + p_2 - \sum_{i=1}^n p'_i \right)}{\bar{v}_{rel}} \left(\frac{N_1}{2E_1} \right) \left(\frac{N_2}{2E_2} \right) S, \quad (2.1)$$

following [?] with the definition of the Lorentz-scalar flux factor

$$\bar{v}_{rel} = \frac{\sqrt{(p_1 \cdot p_2)^2 - m_1^2 m_2^2}}{E_1 E_2} \quad \text{and} \quad d\beta \equiv \prod_{i=1}^n \frac{N'_i d^3 p'_i}{2E'_i (2\pi)^3}. \quad (2.2)$$

We denote initial particle energies and momenta with E_k and p_k , whereas final particle energies and momenta are denoted by E'_k and p'_k . In the case of collinear collisions of the initial particles, considered here, the relative velocity in Eq. (2.1) changes to the expression $\bar{v}_{rel} = |\vec{v}_1 - \vec{v}_2|$. Furthermore, the factors N_i contain spin features of the particles as

$$N_i = \begin{cases} 1 & \text{Bose particles (e.g. photons and gluons),} \\ 2m_i & \text{Dirac particles (e.g. quarks).} \end{cases} \quad (2.3)$$

The spinors are normalised to 1 in the Dirac case. The statistical factor

$$S = \prod_i \frac{1}{l_i!} \quad (2.4)$$

accounts for the case of l_i identical particles of sort i in final state.

Now we evaluate a relation for describing two-to-three parton scattering by including one-gluon emission in the event $1 + 2 \rightarrow 1' + 2' + 3$, as sketched in Fig. 2.1.

The probability of radiating a single gluon as particular scattering process is given by the ratio between elastic and inelastic differential cross section. The corresponding inelastic cross section as special case of Eq. (2.1) is given by

$$d\sigma_{inel} = \frac{S \cdot (2\pi)^4 \delta^{(4)}(p_1 + p_2 - p'_1 - p'_2 - k)}{|\vec{v}_1 - \vec{v}_2|} \left(\frac{N_1}{2E_1} \right) \left(\frac{N_2}{2E_2} \right) |M_{inel}|^2 \\ \times \frac{N'_1 d^3 p'_1}{2E'_1 (2\pi)^3} \frac{N'_2 d^3 p'_2}{2E'_2 (2\pi)^3} \frac{d^3 k}{2\omega (2\pi)^3}, \quad (2.5)$$

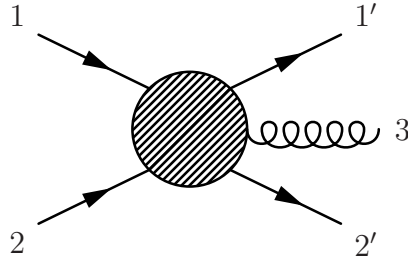


Figure 2.1: Schematic scattering diagram for the process $1+2 \rightarrow 1'+2'+3$. It describes an event where two initial quarks scatter each other resulting into two final quarks and a single radiated gluon. The blob stands for the matrix element of the process.

where the four vector $k = (\omega, \vec{k})$ is for the emitted gluon with wave three-vector \vec{k} and energy ω . The elastic differential cross section for the process $1 + 2 \rightarrow 1' + 2'$ is

$$d\sigma_{el} = \frac{S \cdot (2\pi)^4 \delta^{(4)}(p_1 + p_2 - p'_1 - p'_2)}{|\vec{v}_1 - \vec{v}_2|} \left(\frac{N_1}{2E_1} \right) \left(\frac{N_2}{2E_2} \right) |M_{el}|^2 \times \frac{N'_1 d^3 p'_1}{2E'_1 (2\pi)^3} \frac{N'_2 d^3 p'_2}{2E'_2 (2\pi)^3}. \quad (2.6)$$

Of course, one has to perform the sum and averaging of squared matrix elements (indicated with an overline) before implementing in the differential cross section. Now, the gluon number distribution, i.e. the ratio of elastic and inelastic contributions, follows from Eqs. (2.5) and (2.6) as

$$dn_g = \frac{\overline{d\sigma}_{inel}}{\overline{d\sigma}_{el}} = \frac{\overline{|M_{inel}|^2}}{\overline{|M_{el}|^2}} \cdot \frac{d^3 k}{2\omega (2\pi)^3}, \quad (2.7)$$

This approach holds only true for small gluon momenta compared with momenta of the other particles (soft-gluon limit). Thus, the phase space distribution describing the probability of single-gluon emission under the condition that a quasi-elastic scattering with soft gluon emission event has occurred reads as

$$R = \omega \frac{dn_g}{d^3 k} = \frac{1}{2(2\pi)^3} \frac{\overline{|M_{inel}|^2}}{\overline{|M_{el}|^2}} \equiv R_{total} \quad (2.8)$$

which is used in further numerical calculations.

In the tree-level approximation the mentioned matrix elements $|M_{el}|$ and $|M_{inel}|$ are given by the Feynman diagrams depicted in Figs. 2.2 - 2.5. In what follows we rely on these diagrams when considering quark-quark scattering. Particular emphasis is put on diagram Fig. 2.5, where the non-Abelian character of QCD by the triple-gluon vertex shows up.

2.2 Quark-Quark Scattering

All scattering events take place in the tree level approximation with the exception of the running coupling discussed in Section 4.6, i.e. self energy contributions and vertex correc-

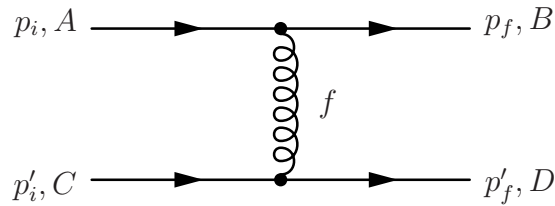


Figure 2.2: Elastic quark-quark scattering diagram.

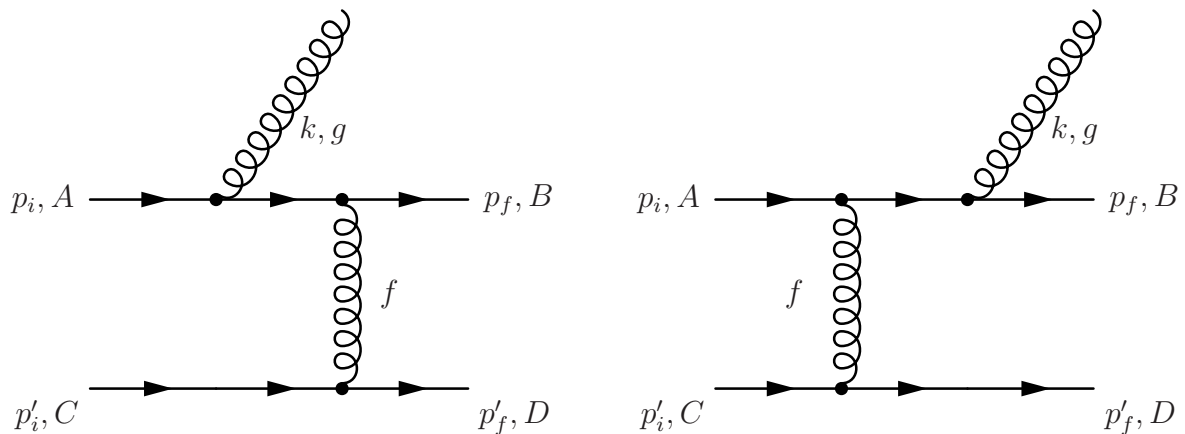


Figure 2.3: One-gluon emission from projectile line.

tions are not taken into consideration. Please note that in this thesis we completely neglect the production amplitude $J(p)$ ¹ by assuming only on-shell quarks as initial particles.

For inelastic scattering we consider four Abelian diagrams with a single gluon emission besides of the fundamental elastic scattering diagram. Due to the possibility of gluon self-interaction the only non-Abelian diagram Fig. 2.5 has to take into account in deriving the total radiation amplitude. In Section 3.4, various kinematic situations are investigated in order to find analytical approaches for the Abelian and non-Abelian matrix elements. Here, we are indexing the matrix elements as $M_{n,m,l}$ from [Gyu00b]; this notation is explained in detail in Appendix A.

The elastic scattering event with a single exchanged gluon is described in Fig. 2.2, using the outlined notation and conventions in Appendices A and F. The Abelian inelastic process is represented by the mentioned Feynman diagrams in Figs. 2.3 and 2.4 where we differentiate for the sake of shorthand notation whether the gluon is emitted before (pre) and after (post) scattering of the projectile quark with the target one. The diagrams in Figs. 2.2 - 2.5 clarify also our momentum and colour conventions.

Of course, the QCD expressions for quark-quark scattering with emitting a single gluon can be easily reduced to the QED case by neglecting colour algebra and considering

¹This effective jet source current is due to the quarks formed from hadron jets; it is studied in [Gyu00a, Djo03b].

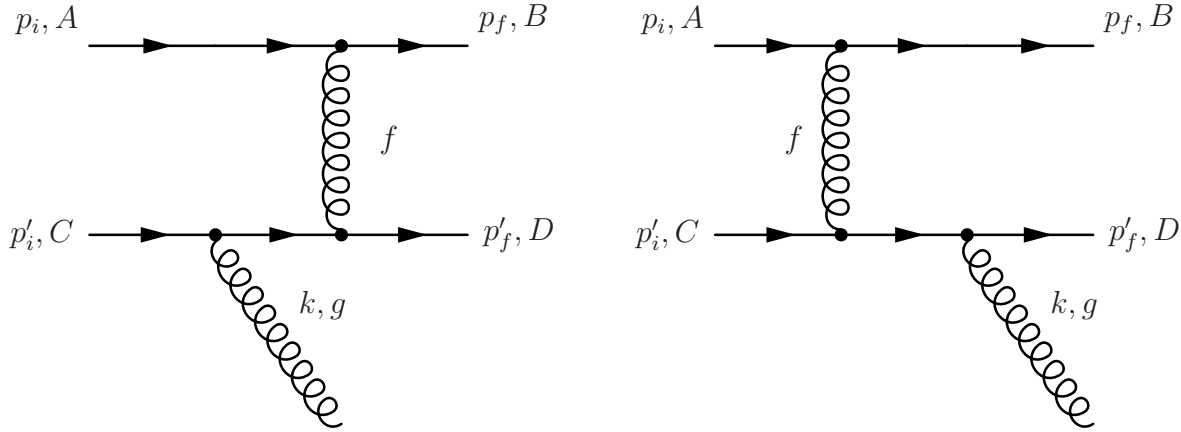


Figure 2.4: One-gluon emission from target line.

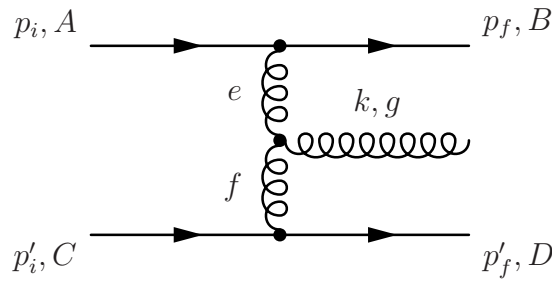


Figure 2.5: Three-gluon contribution in quark-quark scattering.

electromagnetic coupling; diagram 2.5 does not occur in QED.

2.3 The Potential Model

In order to simplify further the quark-quark scattering, the potential model was employed firstly by Gyulassy and Wang in [Gyu94, Wan95]. It is based on the following ideas.

In A^+ -gauge (see Appendix F) one can neglect target contributions, i.e. the diagrams in Fig. 2.4, compared to projectile and three-gluon radiation. To model this situation, target partons are considered as heavy particles, with masses much larger than projectile quark masses. Asymptotically, no energy transfer between several heavy-light collisions happens; that means only a spatial momentum transfer is allowed.

We start with localised scattering centres at \vec{x}_i in configuration space which create in their surrounding areas a classical static screened Coulomb potential in the form

$$\tilde{\varphi}(\vec{x}) = \frac{Q}{4\pi|\vec{x} - \vec{x}_i|} e^{-\tilde{\mu}|\vec{x} - \vec{x}_i|}. \quad (2.9)$$

In order to change to the momentum space representation of the Yukawa type potential, one uses the Fourier transformation $f(\vec{q}) = \int d^3x \tilde{f}(\vec{x})$ to get

$$\varphi(\vec{q}) = Q \cdot \frac{e^{-i\vec{q}\vec{x}}}{\vec{q}^2 + \tilde{\mu}^2}. \quad (2.10)$$

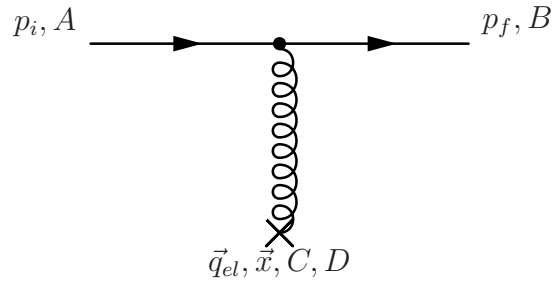


Figure 2.6: Elastic scattering diagram.

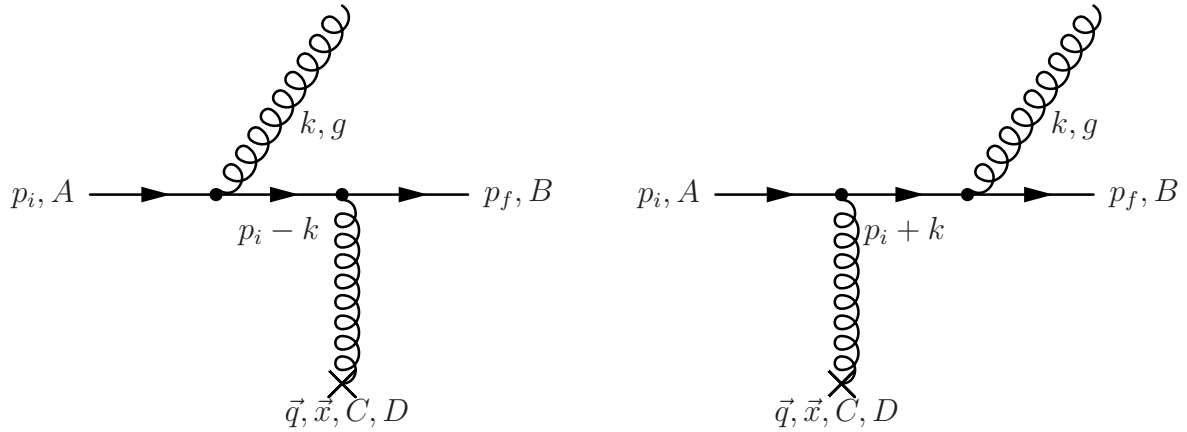


Figure 2.7: a) Pre-projectile emission.

b) Post-projectile emission.

Generalising to the QCD case we have to replace the charge Q by the strong interaction strength g and target colour factor T_{AB}^a . Now, the static potential screened by a modified Debye mass $\tilde{\mu}$, defined in Appendix D, reads as

$$V_{AB}^a(\vec{q}) = gT_{AB}^a \cdot \frac{e^{-i\vec{q}\vec{x}}}{\vec{q}^2 + \tilde{\mu}^2}. \quad (2.11)$$

According to a separation between two successive scatterings we assume

$$\lambda_p \gg \tilde{\mu}^{-1}, \quad (2.12)$$

where $\tilde{\mu}^{-1}$ denotes the modified Debye screening length and λ_p is the mean free path length of the incident projectile parton. The important role of the modified screening parameter due to its regularisation character in the denominator is discussed in Section 2.6.

The Feynman diagrams for scattering at a Debye screened potential (without target radiation contributions, of course) are obtained as shown in Figs. 2.6, 2.7 and 2.8, following the restriction scheme for quark-quark scattering.

2.4 Multiple Scattering: The Landau-Pomeranchuk-Migdal (LPM) Effect

In order to better understand the radiative energy loss of quarks undergoing subsequent scatterings we turn now to scattering from an electromagnetic point of view in a classical

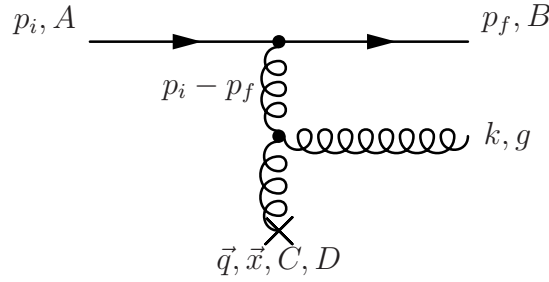


Figure 2.8: Three-gluon contribution.

context, as discussed in [Pav97, Mül99] for example. For simplicity, we study the single scattering (SS) at first, that is to say incoming particles scatter at one centre. Later on, the extension to double (DS)- and multiple (MS) scattering scenarios is sketched. Note that we write explicitly the speed of light c to emphasise limits for particles with velocities close to c .

We start with an expression for the differential intensity I as a function of the energy ω and the solid angle Ω with respect to the radiated photon. This equation, following expressions in Chapter 14 of the standard textbook for classical electrodynamics [Jac98], reads as

$$\frac{d^2 I}{d\omega d\Omega} = \frac{e^2 k^2}{4\pi^2} \left| \int_{-\infty}^{\infty} dt [\vec{n} \times \vec{v}(t)] e^{i\omega t - i\vec{k} \cdot \vec{r}(t)} \right|^2, \quad (2.13)$$

where

$$\vec{n} = \frac{\vec{k}}{|\vec{k}|} \quad \text{and} \quad \vec{v}(t) = \frac{d}{dt} \vec{r}(t) \quad (2.14)$$

with $\vec{v}(t)$ as the velocity of a charged particle travelling along the trajectory $\vec{r}(t)$. The elementary charge e is related to the Sommerfeld's finestructure constant by $\alpha = e^2/4\pi \cong 1/137$. Additionally, the vacuum dispersion relation $\omega = |\vec{k}|$ as a function of the wave vector \vec{k} is used. Furthermore, a noteworthy fact is that the integration time thresholds $t = \pm\infty$ are covered by an additional convergence factor, $e^{-\epsilon|t|}$, and going to the limit $\epsilon \rightarrow 0$ after evaluating the integral function.

With the aim of describing a dilute medium the particle is assumed to move piecewise on a straight line without disturbance and constant velocity unless in the centre point of scattering. In physical terms, this means that we are interested in wavelengths being much larger than the spatial extension of the scattering process. The details of the scattering event itself are not resolved by such large wavelengths, and consequently, one can neglect its spatial structure and shrink it to a point. This approximation can not be justified for short wavelengths.

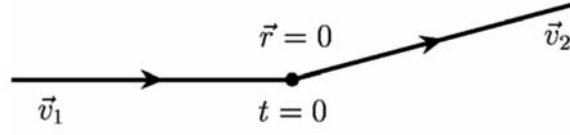


Figure 2.9: Simplified single scattering event. The collision process is concentrated in the point $\vec{r} = 0$ at the time $t = 0$.

Now, we investigate the process of

SINGLE SCATTERING

as sketched in Fig. 2.9. We have to integrate Eq. (2.13) over infinite times and yield

$$\begin{aligned} \left(\frac{d^2 I}{d\omega d\Omega} \right)_{SS} &= \frac{e^2}{4\pi^2 c^2} \left| [\vec{n} \times \vec{v}_1] \int_{-\infty}^0 dt e^{i\omega(1-\vec{n}\vec{v}_1/c)t} + [\vec{n} \times \vec{v}_2] \int_0^{\infty} dt e^{i\omega(1-\vec{n}\vec{v}_2/c)t} \right|^2 \\ &= \frac{e^2}{4\pi^2 c^2} \left| \frac{\vec{n} \times \vec{v}_1(t)}{(1 - \frac{\vec{n}\vec{v}_1}{c})} - \frac{\vec{n} \times \vec{v}_2(t)}{(1 - \frac{\vec{n}\vec{v}_2}{c})} \right|^2 \end{aligned} \quad (2.15)$$

with help of $\omega \rightarrow \omega + i\epsilon$. One can derive a prevailed emission radiation direction of the intensity spectrum in Eq. (2.15), which is shown in Fig. 2.10 for different particle velocities. If the radiation is focused in direction $\vec{v}_{1,2}$, i.e. the denominators of Eq. (2.15) become small, the spectrum is peaked in forward direction for ultra-relativistic electrons, so to say for $|\vec{v}| \rightarrow c$, whereas the radiation vanishes perpendicular to the particle velocity in this configuration.

DOUBLE SCATTERING

The consideration of a double scattering process goes in the same manner as single scattering. After an idealisation referring to the medium density we obtain for the radiation intensity of electron scattering at two centre points, as exhibited in Fig. 2.11,

$$\begin{aligned} \left(\frac{d^2 I}{d\omega d\Omega} \right)_{DS} &= \frac{e^2}{4\pi^2 c^2} \left| \frac{\vec{n} \times \vec{v}_1(t)}{(1 - \frac{\vec{n}\vec{v}_1}{c})} + \frac{\vec{n} \times \vec{v}_2(t)}{(1 - \frac{\vec{n}\vec{v}_2}{c})} \left(e^{i\omega(1-\frac{\vec{n}\vec{v}_2}{c})\Delta t} - 1 \right) \right. \\ &\quad \left. - \frac{\vec{n} \times \vec{v}_3(t)}{(1 - \frac{\vec{n}\vec{v}_3}{c})} e^{i\omega(1-\frac{\vec{n}\vec{v}_3}{c})\Delta t} \right|^2. \end{aligned} \quad (2.16)$$

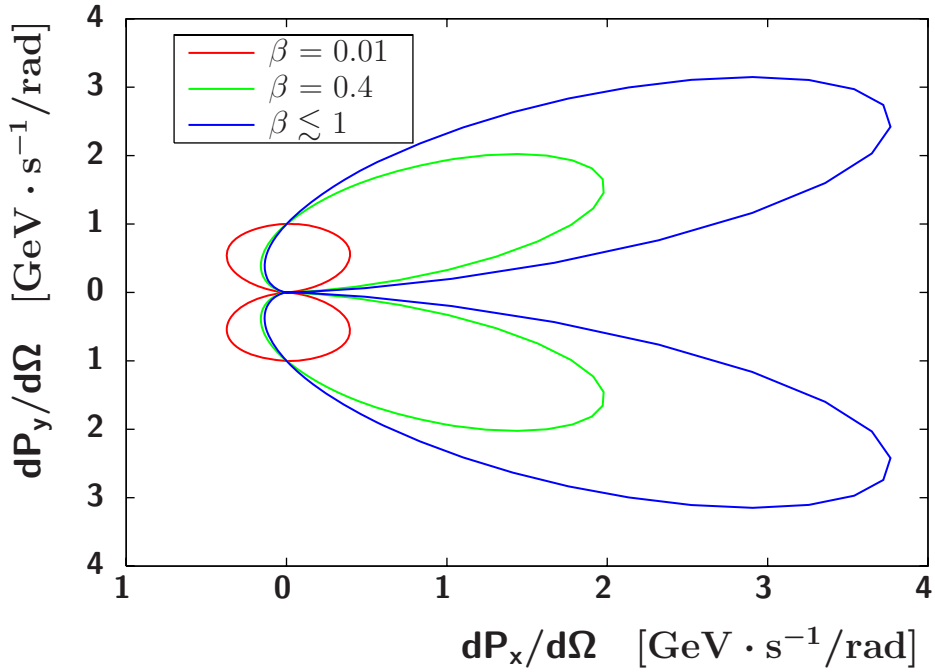


Figure 2.10: The club-shaped radiation cone in a polar plot of the gluon radiation angle ϑ for different parameters of $|\beta| = |\vec{v}|/c$. The particle's velocity vector $\vec{v}(t)$ is orientated horizontally. The red curve shows the spectrum for a slowly particle ($\beta \simeq 0$), whereas the strongly peaked cone is for $\beta = 0.6$ in forward direction (blue line), $\beta = 0.4$ is an intermediate case. The club represents the radiated power per infinitesimal spatial angle element $dP(t)/d\Omega \propto \sin^2 \vartheta / (1 - \beta \cos^5 \vartheta)$ (see [Jac98]).

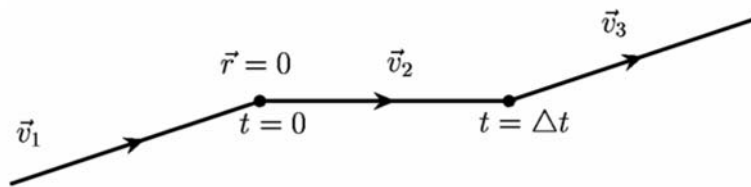


Figure 2.11: Schematic representation of a double scattering process.

If we are now interested in the soft photon limit, $\omega \rightarrow 0$, it yields only two dominant contributions in Eq. (2.16), corresponding to the initial electron before the first scattering and the final electron after the second collision. Thus, we encounter a condition for the formation time as

$$\tau_f \equiv \frac{1}{\omega \left(1 - \frac{\vec{n}\vec{v}_2}{c}\right)} \gg \Delta t, \quad (2.17)$$

which hence allows us to neglect the intermediate part between the two interactions. Indeed, for this soft photon approximation one can speak about a destructive interference if the formation length l_f is much larger than the distance d between two scattering events, i.e.

$$l_f \equiv |\vec{v}_2| \cdot \tau_f \gg d. \quad (2.18)$$

Owing to this, the double scattering looks effectively like a single scattering.

For the opposite case of relation Eq. (2.18), $l_f \ll d$, the double scattering process is expressed like a sum of two independent single scatterings, each in form of Eq. (2.15), due to fluctuations in the exponential factors of Eq. (2.16) which cancel interference terms.

MULTIPLE SCATTERING

We study the scattering at N centres as displayed in Fig. 2.12. Referring to SS and DS scenarios, the intensity spectrum is now evaluated in a similar way. We find in an generalisation of DS from Eq. (2.16) an expression for the formation length

$$l_f \equiv \frac{|\vec{v}_\parallel|}{\omega \left(1 - \frac{\vec{n}\vec{v}_\parallel}{c}\right)} \gg d \quad (2.19)$$

with a dependency of the electron's velocity projection \vec{v}_\parallel in the initial direction of the particle \vec{v}_i . We now consider a medium with thickness L with an anticipated effective number of scatterings given by

$$N_{eff} = \frac{L}{l_f} \quad \text{assuming} \quad l_f < L, \quad (2.20)$$

reading as a superposition of effective single spectra, labelled with \overline{SS} . Due to this fact, the resulting spectrum factorises and is a multitude of SS:

$$\left(\frac{d^2 I}{d\omega d\Omega}\right)_{MS} = N_{eff} \cdot \left(\frac{d^2 I}{d\omega d\Omega}\right)_{\overline{SS}}. \quad (2.21)$$

The standard approach to bremsstrahlung effects was presented by Bethe and Heitler (BH). It is based on a Born approximation for relativistic electrons. In the limit of $N_{eff} \rightarrow N$ the BH limit yields Eq. (2.21), as shown in standard literature [Lan86].

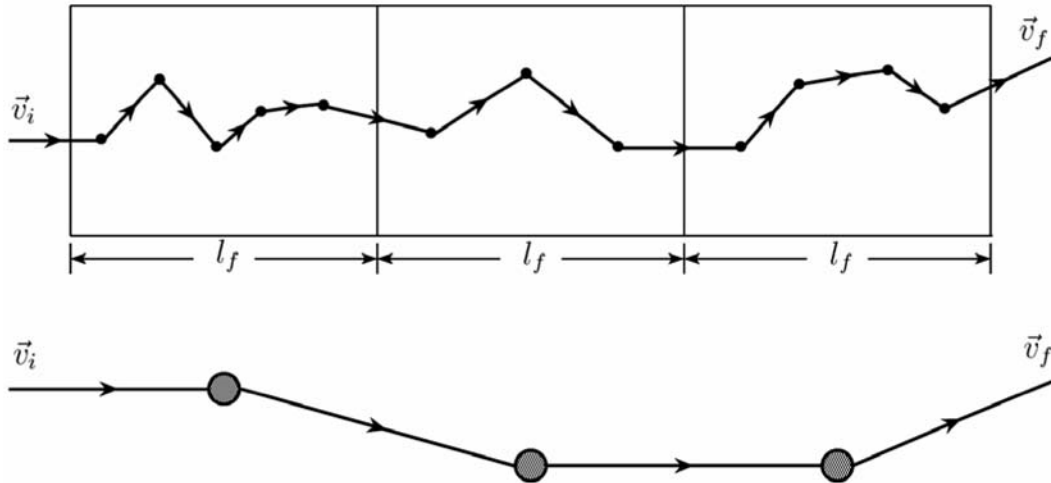


Figure 2.12: Multiple scattering in the LPM regime within an amorphous medium. The effective single scattering centres are displayed in the lower picture as filled points. The number of this points is labelled by N_{eff} , in contrast to the number of real scatterings which is sketched in the upper graphics with small black points, situated within the formation length l_f .

Now, we give some further explanations and comments with respect to the radiation cone exhibited in Fig. 2.10 and comments to conditions of the LPM effect.

The typical relation of the average (squared) emission angle for relativistic radiation is

$$\theta_{rad} \equiv \langle \theta_{rad}^2 \rangle^{1/2} = \frac{1}{\gamma} = \frac{mc^2}{E} \quad (2.22)$$

with the electron's mass m and its energy E . This implies a separation of the photon and electron over the same distance, called formation length l_f . Hence, the process of emission can be disturbed, e.g. by the scattering of electrons. This is actually called LPM effect. If the electron scatters out of the radiation cone, $\overline{\theta_s^2} \gg \theta_{rad}^2$, an estimate for the mean squared scattering angle $\overline{\theta_s^2}$ in a random walk picture can be given [Pav97]. It yields a relation of this average angle to the formation length

$$l_f \propto \frac{\sqrt{\omega}}{E}, \quad (2.23)$$

and thus the intensity, respectively the energy spectrum Eq. (2.21), becomes proportional to the inverse formation length. In the other case, i.e. for $\overline{\theta_s^2} < \theta_{rad}^2$, the spectrum in BH limit becomes constant.

In a comprehensive notation, the proper LPM effect denotes the electron scattering off the forward radiation cone due to multiple scatterings after a particular distance, respectively the formation length l_f . As a result, the radiation becomes suppressed due to destructive interferences. For the interested reader we refer to [Mig56, Ter72, Akh96] for further details. Very often, each destructive interference is denoted as LPM effect.

In the following section, the influence of the intensity spectrum by the medium polarisation is discussed.

2.5 Ter-Mikaelian (TM) Effect

We further continue our explanation on an electromagnetic analogue by considering bremsstrahlung effects, basing on ultra-relativistic electrons. In order to outline the basic ideas of this effect, first described by Ter-Mikaelian [Ter72], we start with an estimate for the in-medium gluon dispersion relation and follow later classical coherence arguments by Galitsky and Gurevich in [Gal64] in addition to qualitative estimates for the formation length.

The proper TM effect refers to photons, but having in mind the QCD analogue, we apply the corresponding notions already here to gluons. The dispersion relation in a medium between gluon energy ω and the spatial momentum \vec{k} becomes

$$\omega \equiv \omega(k) = \frac{|\vec{k}|}{\sqrt{\varepsilon}}, \quad (2.24)$$

in contrast to the vacuum relation $\omega = |\vec{k}|$ with the 'dielectrical' medium parameter ε . This dielectrical 'constant' becomes in the high-frequency approximation

$$\varepsilon = \left(1 - \frac{\omega_0^2}{2\omega^2}\right)^2 \approx 1 - \frac{\omega_0^2}{\omega^2} \quad (2.25)$$

following ideas from [Ter72]. Here, we associate the effective gluon mass parameter ω_0 with a constant value directly related to the plasma frequency ω_p of the surrounding medium. We are not taking into account asymptotic- and dynamical masses (for this, see [Djo03a, Djo03b]). We combine Eqs. (2.24) and (2.25) and yield nothing else but the on-shell condition for gluons traversing a medium,

$$k^2 = \omega^2 - |\vec{k}|^2 = \omega_0^2. \quad (2.26)$$

This dispersion relation expresses the modification of gluonic excitations propagating through a medium. The vacuum case is recovered by $\omega_0 \rightarrow 0$. Equation (2.26) is the input and constitutes the basis of modified kinematical expressions and propagators for calculating the total radiation amplitude, compared to those in vacuum.

The basic idea from Galitsky and Gurevich is based on a geometrical condition,

$$l(\omega, \vartheta) = \frac{\lambda v \cdot \overline{\cos \vartheta_s}}{2 \left(\frac{1}{\sqrt{\varepsilon}} - v \cos \vartheta \cdot \overline{\cos \vartheta_s} \right)}, \quad (2.27)$$

to maintain coherence². This length l can be defined as the pathlength the emitting electron travels over which the radiation remains coherent and is identified over the formation length given by Eq. (2.19) in the previous section. It corresponds, apart from a constant factor π , only by setting $\varepsilon = 1$ for the vacuum, $\lambda = 2\pi/\omega$ as the wavelength and $|\vec{v}_{||}| = v \cdot \cos \vartheta_s$, where ϑ_s denotes the multiple scattering angle of the electron (in contrast to ϑ as the radiation emission angle) with $\overline{\cos \vartheta_s}$ as its average value. Now, the

²The additional modification term $1/\sqrt{\varepsilon}$ in Eq. (2.27) stands for the increased phase velocity of the emitted bremsstrahlung

radiation intensity can be expressed in terms of the BH intensity by a reduction factor $q \equiv I(\omega)/I_{BH}(\omega) = l(\omega, 0)/l^{vac}(\omega, 0)$. It is the ratio of the forward emission ($\cos \vartheta \approx 1$) coherence length in medium and the length l^{vac} in the absence of medium effects ($\varepsilon = 1$ and $\cos \vartheta_s = 1$). Hence, one finally obtains with the help of some approximations and under the assumption $\varepsilon \approx 1$ the relation

$$q = \frac{\omega^2}{\omega^2 + \omega_0^2 \left(\frac{E^2}{m^2} \right)} < 1, \quad (2.28)$$

with the already introduced definitions of m and E as electron mass and energy. This behaviour shows a strong suppression of the electron spectrum for low energies, thus removing the infrared divergences for $\omega \rightarrow 0$.

This reduction of the formation length can also be seen in electrodynamics by following more simple qualitative estimates. The formation length in vacuum can also be written as

$$l_f^{vac} = \frac{2\gamma^2}{\omega} \quad \text{with} \quad \gamma^{-2} = 1 - v^2, \quad (2.29)$$

where γ is the Lorentz factor of the radiating particle. In considering medium polarisation, the Lorentz factor can be rewritten as $\gamma = 1 - \varepsilon v^2$, and thus the vacuum formation length (see Eq. (2.29)) is reduced to

$$l_f = \frac{2\omega}{\omega_0^2} \quad (2.30)$$

in the limit $\omega_0 \ll \omega \ll \gamma\omega_0$. This reflects the suppression of photon radiation due to the dielectrical medium effect. In Section 4.3, additional attendance is given on the formation time which is directly related to the previous in-medium formation length l_f .

Note that the TM effect³ shows a different behaviour compared with the LPM effect. The TM effect we discussed here suppresses the bremsstrahlung photon spectrum at the very soft threshold, while the LPM effect becomes operative at larger photon or gluon energies. At even larger energies one recovers the BH regime, in case of photon bremsstrahlung by electrons.

In summarising the previous discussion, one can find a reduction of the soft-bremsstrahlung spectrum off an relativistic electron passing an amorphous medium. This behaviour is caused by the polarisation of the medium.

Here, we outlined this effect only in an electrodynamical framework. Other works (cf. [Mül99, Käm00, Djo03a, Djo03b]) extend this medium effect on the QCD case for radiated gluons instead of photons. We follow the ideas from Kämpfer *et al.* [Käm00], while only taking the modified gluon on-shell condition into account and neglecting higher order effects, e.g. gluon self-energy as considered in works of Gyulassy and Djordjevic⁴ [Djo03a, Djo03b].

³It is also known as dielectrical effect or longitudinal density effect.

⁴Recently, QCD lattice data extract $\omega_0(T)$ with typical effective gluon mass of a few hundred MeV (slightly above the confinement temperature). This causes a relevance of only transverse gluon modes in contrast to [Djo03b].

3 Single Quark Scattering

The radiation amplitude is the basis for calculating the energy loss of heavy quarks. In the background of that aim, we concentrate on analytical estimations for the matrix elements in order to give an approach for this often used amplitude of the radiation process and compare the results later on with numerical computations.

Here, we consider mainly the kinematical situation for single quark scattering with induced one-gluon radiation in the QCD case, meaning that double scattering contributions and higher order diagrams are neglected. This consideration demonstrates in an impressive way the importance of the modified dispersion relation which was introduced in the previous chapter. Furthermore, we will give a brief overview on the Gunion-Bertsch radiation amplitude as one possible description of quark-quark scattering.

3.1 Kinematics for Potential Model with One-Gluon Emission

In this section, the kinematical situation is derived for a single quark scattering event with emitting one gluon in the potential model, analogue to [Wan95]. The aim is to derive a few suitable approximations for analytical evaluations. The numerical evaluation in Chapter 4, however, is performed with exact kinematics.

We start with the on-shell condition of the projectile quark, $p_i^2 = m^2$ (see Figs. 2.1 - 2.5), with a quark mass parameter m given as constant. The direction of the incident quark is chosen in z-direction,

$$p_i = (E_i, 0, 0, p_{iz}). \quad (3.1)$$

For simplicity, we use the notation $E_i \equiv E$ as the initial quark energy determined by the positive root of the on-shell condition.

It is suitable to work in light-cone coordinates due to our special choice of fixing the gauge at $A^+ = 0$ (see Appendices B and E). With this declaration one yields¹

$$p_i = \left[E + \sqrt{E^2 - m^2}, E - \sqrt{E^2 - m^2}, \vec{0}_\perp \right] \approx \left[2E - \frac{m^2}{2E}, \frac{m^2}{2E}, \vec{0}_\perp \right], \quad (3.2)$$

where the last expression assumes a small quark mass m compared to the energy E , $m/E \ll 1$.

¹Please note that the quark on-shell condition is only satisfied in order of $(1/E)^0$.

The on-shell condition for the emitted gluon, $k^2 = \omega_0^2$, leads us to one possible representation of the gluon four-momentum

$$k_\mu \equiv (k_0, \vec{k}_\perp, k_z) = \left(\sqrt{\omega^2 + \omega_0^2}, \omega \cdot \cos \varphi \sin \vartheta, \omega \cdot \sin \varphi \sin \vartheta, \omega \cdot \cos \vartheta \right), \quad (3.3)$$

where $(\varphi, \vartheta, \omega)$ denotes the usual 3-dimensional spherical coordinates. So, the momentum of the gluon is expressed in light-cone coordinates as

$$k = \left[2Ex, \frac{\vec{k}_\perp^2 + \omega_0^2}{2Ex}, \vec{k}_\perp \right]. \quad (3.4)$$

For the sake of neglecting target contributions in the total radiation amplitude we fixed the special gauge. Thus, we obtain for the polarisation four-vector

$$\epsilon = \left[0, 2 \cdot \frac{\vec{\epsilon}_\perp \vec{k}_\perp}{2Ex}, \vec{\epsilon}_\perp \right]. \quad (3.5)$$

The gluon momentum is parametrised in its plus-component by x which is defined in agreement with Eqs. (3.4) and (3.5) as

$$x \equiv \frac{k_0 + k_\parallel}{2E} = \frac{\sqrt{\omega^2 + \omega_0^2} + \omega \cos \vartheta}{2E}. \quad (3.6)$$

In association to the screening parameter ω_0 as the effective gluon mass and m as the incident quark mass one can define the parametric angles

$$\vartheta_p = \frac{\omega_0}{k_0} \quad \text{and} \quad \vartheta_d = \frac{m}{E} \quad (3.7)$$

as related quantities to the according particle energies k_0 and E . With the help of this definition we find another expression for the parameter x in the form of

$$x = \frac{k_0}{2E} \left(1 + \sqrt{1 - \vartheta_p^2} \cos \vartheta \right) \quad (3.8)$$

with the restriction $0 \leq x \leq 1$, because the maximum energy available for the gluon is $2E$. Furthermore, the limits $E \gg m$ and $E \gg q_\perp$ have to be assumed when we simplify kinematical expressions by a Taylor expansion and neglect higher orders in $1/E$.

3.1.1 Elastic Potential Scattering

At first we apply the relevant Feynman rules (see Appendix D) on the single elastic scattering process, Fig. 2.6, within the potential model approach. The process is described by the matrix element $M_{1,el}$. Therefore, the matrix element reads

$$\begin{aligned} M_{1,el} &= T_{AB}^c T_{CD}^c \cdot (-ig)(p_f + p_i)_\mu \cdot (-ig)g^{0\mu} \cdot \frac{e^{-i\vec{q}_{el}\vec{x}}}{\vec{q}_{el}^2 + \tilde{\mu}^2} \\ &= T_{AB}^c T_{CD}^c \cdot 2E(-g^2) \cdot \frac{e^{-i\vec{q}_{el}\vec{x}}}{\vec{q}_{el}^2 + \tilde{\mu}^2}, \end{aligned} \quad (3.9)$$

using the fact that the potential only imparts a spatial momentum transfer to the projectile, i.e. $q_0 = 0$. The denominator of (3.9) contains the modified Debye screening parameter $\tilde{\mu}$ and implements in this way the non-vanishing mass of the intermediate gluon in the medium.

3.1.2 Inelastic Potential Scattering

The general conservation of the total four-momentum,

$$p_i + q = p_f + k, \quad (3.10)$$

besides the on-shell condition for the emitted gluon, $k^2 = \omega_0^2$, and the Lorentz condition, $\epsilon k = 0$, constitutes the basis of the following evaluations for inelastic scatterings. We also use the proper relation for the zeroth-component of the transverse momentum, $q_0 = 0$, due to the potential ansatz.

We begin our discussion with the

PRE-PROJECTILE GLUON EMISSION.

In Fig. 2.7a, the situation is depicted for single gluon emission from the projectile line before the initial quark scatters with the static potential, associated to the matrix element $M_{1,0,0}$. The accompanying matrix element is given by

$$\begin{aligned} M_{1,0,0} &= (T^f T^g)_{AB} T_{CD}^f \cdot (-ig)(p_f + p_i - k)_\mu \cdot \frac{i}{(p_i - k)^2 - m^2 + i\epsilon} \\ &\times (-ig)(2p_i - k)_\sigma \epsilon^\sigma \cdot (-ig)g^{0\mu} \cdot \frac{e^{-i\vec{q}\vec{x}}}{\vec{q}^2 + \tilde{\mu}^2}, \end{aligned} \quad (3.11)$$

which can be reduced to

$$M_{1,0,0} = (T^f T^g)_{AB} T_{CD}^f \cdot 2(E - k_0)g^3 \cdot \frac{e^{-i\vec{q}\vec{x}}}{\vec{q}^2 + \tilde{\mu}^2} \cdot \frac{p_i \epsilon}{p_i k}. \quad (3.12)$$

Now, we have to calculate the latter ratio in the equation above. It yields with the previous kinematical approximations

$$\frac{p_i \epsilon}{p_i k} \approx \frac{2\vec{\epsilon}_\perp \vec{k}_\perp}{\vec{k}_\perp^2 + x^2 m^2 + \omega_0^2}. \quad (3.13)$$

For small effective gluon masses ω_0 compared to ω and in the limit of small gluon emission angles ϑ (forward direction) one is able to rewrite the energy pre-factor in (3.12) as $E(1-x)$ and obtains

$$\begin{aligned} M_{1,0,0} &\approx \frac{M_{1,el}}{T_{A'B'} T_{C'D'}} \cdot (-2g) \cdot (T^f T^g)_{AB} T_{CD}^f \cdot (1-x) \\ &\times \frac{\vec{\epsilon}_\perp \vec{k}_\perp}{\vec{k}_\perp^2 + x^2 m^2 + \omega_0^2}, \end{aligned} \quad (3.14)$$

i.e. , a factorisation of the elastic amplitude (3.9) and remaining part characterising the radiation. This is only possible under the important assumption

$$\vec{q}_{rad} \equiv \vec{q} = \vec{q}_{el}, \quad (3.15)$$

and is discussed further in Section 3.6 in detail. Since in the soft gluon limit with $x \ll 1$, the factor $(1-x)$ can be omitted and (3.32) is obtained.

Now, we continue with the

POST-PROJECTILE GLUON EMISSION

and start again at the application of Feynman rules in the according diagram, shown in Fig. 2.7b. The corresponding matrix element can be written as

$$M_{1,1,0} = (T^g T^f)_{AB} T_{CD}^f \cdot (-ig)(2p_f + k)_\sigma \epsilon^\sigma \cdot \frac{i}{(p_f + k)^2 - m^2 + i\epsilon} \quad (3.16)$$

$$\times (-ig)(p_f + k + p_i)_\mu \cdot (-ig)g^{0\mu} \cdot \frac{e^{-i\vec{q}\vec{x}}}{\vec{q}^2 + \tilde{\mu}^2},$$

in the same manner as (3.11) according to the appropriate diagram, and one obtains

$$M_{1,1,0} = (T^f T^g)_{AB} T_{CD}^f \cdot 2E \cdot (-g^3) \cdot \frac{e^{-i\vec{q}\vec{x}}}{\vec{q}^2 + \tilde{\mu}^2} \cdot \frac{p_f \epsilon}{p_f k}. \quad (3.17)$$

Here, it is absolutely necessary to consider the momentum transfer q due the entering of the final quark momentum. We give only the needed relations as a summary of the used expressions. The relevant quantity q in light-cone variables reads

$$q = [q_z, -q_z, \vec{q}_\perp]. \quad (3.18)$$

Later on needed relations are combinations with the momentum transfer,

$$qp_i = q_z \left(\frac{m^2}{2E} - E \right), \quad qk = q_z \left(\frac{\vec{k}_\perp^2 + \omega_0^2}{4Ex} - Ex \right) - \vec{q}_\perp \vec{k}_\perp. \quad (3.19)$$

With squaring the four-momentum conservation (3.10) we reach our aim to describe the z-component of the momentum transfer in terms of the given quantities p_i , q and the gluon momentum k . So, it yields from $p_f^2 = (p_i + q - k)^2$ the equation for q_z

$$0 = q_z^2 + 2q_z \left(E(1-x) + \frac{\vec{k}_\perp^2 + \omega_0^2}{4Ex} - \frac{m^2}{2E} \right) + (\vec{k}_\perp - \vec{q}_\perp)^2 + \frac{\vec{k}_\perp^2}{x}(1-x) + x^2 m^2 + \frac{\omega_0^2}{x} \quad (3.20)$$

with the positive root solution

$$q_z^{(+)} = -\frac{\vec{k}_\perp^2 + \omega_0^2}{2Ex} - \frac{(\vec{k}_\perp - \vec{q}_\perp)^2}{2E(1-x)} - \frac{xm^2}{2E(1-x)}, \quad (3.21)$$

while we are neglecting again higher orders in powers of $(1/E)$. We are not interested in the negative root solution, because those results for backward scattering are usually

suppressed by orders of magnitude, compared to the forward scattering event². Thus, the final quark momentum reads as

$$p_f = p_i + q - k \approx \left[2E(1-x) - \omega_0, \frac{(\vec{k}_\perp - \vec{q}_\perp)^2 + m^2}{2E(1-x)}, \vec{q}_\perp - \vec{k}_\perp \right], \quad (3.22)$$

and we can evaluate the ratio of the needed four-products

$$\frac{p_f \epsilon}{p_f k} = 2(1-x) \cdot \frac{\vec{\epsilon}_\perp (\vec{k}_\perp - x\vec{q}_\perp)}{(\vec{k}_\perp - \vec{q}_\perp)^2 + x^2 m^2 + (1-x)^2 \omega_0^2}. \quad (3.23)$$

With this ratio, the post-emission matrix element (3.17) finally becomes

$$\begin{aligned} M_{1,1,0} &\approx \frac{M_{1,el}}{T_{A'B'} T_{C'D'}} \cdot (-2g) \cdot (T^g T^f)_{AB} T_{CD}^f \cdot (1-x) \\ &\quad \times \frac{-\vec{\epsilon}_\perp \left[\vec{k}_\perp \left(1 - \frac{\omega_0}{2E}\right) - x\vec{q}_\perp \right]}{(\vec{k}_\perp - x\vec{q}_\perp)^2 + x^2 m^2 + (1-x)^2 \omega_0^2}. \end{aligned} \quad (3.24)$$

The last contributing diagram is from the non-Abelian

THREE-GLUON EMISSION.

The more complex matrix element structure exhibited in Fig. 2.8 as a Feynman graph is due to the three-gluon vertex and is written as

$$\begin{aligned} M_{1,0,1} &= (-ig)(p_f + p_i)_\mu T_{AB}^e \cdot \frac{-ig^{\tau\mu}}{(p_i - p_f)^2} \cdot \epsilon^\sigma \cdot (-ig)g^{0\rho} \cdot \frac{e^{-i\vec{q}\vec{x}}}{\vec{q}^2 + \tilde{\mu}^2} \cdot T_{CD}^f \\ &\quad \times (-ig)(if_{egf}[(p_i - p_f + k)_\rho g_{\tau\sigma} + (-k - q)_\tau g_{\sigma\rho} + (q - p_i + p_f)_\sigma g_{\rho\tau}]). \end{aligned} \quad (3.25)$$

It can be cast also in the form

$$\begin{aligned} M_{1,0,1} &= [T^f, T^g]_{AB} T_{CD}^f \cdot g^3 \cdot \frac{e^{-i\vec{q}\vec{x}}}{\vec{q}^2 + \tilde{\mu}^2} \cdot \frac{1}{(p_i - p_f)^2 - \omega_0^2} \\ &\quad \times [2k_0(p_i + p_f)\epsilon - \epsilon_0 \cdot (p_i + p_f)(k + q) + (2E - k_0) \cdot 2q\epsilon]. \end{aligned} \quad (3.26)$$

Hence, we have to evaluate firstly the denominator in Eq. (3.26) as

$$\begin{aligned} (p_i - p_f)^2 &= 2m^2 - 2p_i p_f \\ &\approx -\frac{1}{1-x} \left[(\vec{k}_\perp - x\vec{q}_\perp)^2 + x^2 m^2 \right] + \frac{\omega_0 m^2}{2E} - \omega_0^2. \end{aligned} \quad (3.27)$$

²Please note that here we consider about forward resp. backward scattering of the final quark and not the gluon, like often in previous and further investigations.

The single contributions in (3.26) are calculated to

$$I_a \equiv 2k_0(p_i + p_f)\epsilon \approx 2E \cdot \vec{\epsilon}_\perp \left[(2\vec{k}_\perp - x\vec{q}_\perp) - \vec{k}_\perp \cdot \frac{\omega_0}{2E} \right] \quad (3.28)$$

for small emission angles, $\omega \approx xE$, and $\vartheta_p \ll 1$. A further contribution, $I_b \equiv \epsilon_0(p_i + p_f)(k + q)$, can be approximated in leading order in $(1/E)$, and the last term in Eq. (3.26) reads

$$I_c \equiv 2q\epsilon(2E - k_0) \approx -2E(2 - x)\vec{\epsilon}_\perp\vec{q}_\perp + 2E\vec{\epsilon}_\perp\vec{k}_\perp \cdot \frac{\omega_0}{2E}. \quad (3.29)$$

The complete nominator in (3.26) is given by the sum of (3.28) and (3.29):

$$I_a - I_b + I_c \approx I_a + I_c = 2E \cdot 2\vec{\epsilon}_\perp(\vec{k}_\perp - \vec{q}_\perp), \quad (3.30)$$

since we take into account only orders up to $(1/E)^0$ in the second term of (3.30). Thus, the three-gluon matrix element yields

$$M_{1,0,1} \approx \frac{M_{1,el}}{T_{A'B'}T_{C'D'}} \cdot (-2g) \cdot [T^f, T^g]_{AB}T_{CD}^f \cdot (1 - x) \times \frac{-\vec{\epsilon}_\perp(\vec{k}_\perp - \vec{q}_\perp)}{(\vec{k}_\perp - \vec{q}_\perp)^2 + m^2 \left[x^2 - (1 - x)\frac{\omega_0}{2E} \right] + (1 - x)\omega_0^2}. \quad (3.31)$$

In summary, we can approximate the matrix elements (3.14), (3.24) and (3.31) in the limit of soft gluons as

$$M_{1,0,0} = \frac{M_{1,el}}{T_{A'B'}T_{C'D'}} \cdot (-2g) \cdot (T^f T^g)_{AB}T_{CD}^f \cdot \frac{\vec{\epsilon}_\perp\vec{k}_\perp}{\vec{k}_\perp^2 + x^2m^2 + \omega_0^2}, \quad (3.32)$$

$$M_{1,1,0} = \frac{M_{1,el}}{T_{A'B'}T_{C'D'}} \cdot (-2g) \cdot (T^g T^f)_{AB}T_{CD}^f \cdot \frac{-\vec{\epsilon}_\perp \left[\vec{k}_\perp \left(1 - \frac{\omega_0}{2E}\right) - x\vec{q}_\perp \right]}{(\vec{k}_\perp - x\vec{q}_\perp)^2 + x^2m^2 + \omega_0^2}, \quad (3.33)$$

$$M_{1,0,1} = \frac{M_{1,el}}{T_{A'B'}T_{C'D'}} \cdot (-2g) \cdot [T^f, T^g]_{AB}T_{CD}^f \cdot \frac{-\vec{\epsilon}_\perp(\vec{k}_\perp - \vec{q}_\perp)}{(\vec{k}_\perp - \vec{q}_\perp)^2 + m^2 \left[x^2 - \frac{\omega_0}{2E} \right] + \omega_0^2}. \quad (3.34)$$

They reduce to the relations given in [Tho05] for a vanishing effective gluon mass ω_0 . In the limit of vanishing projectile quark masses, the Eqs. (3.14), (3.24) and (3.31) confirm the estimations in [Käm00]. Now, one can combine both approximations and obeys the well-known expressions which were firstly derived by Gunion and Bertsch (cf. [Gun82], Eqs. (12a) - (12c) and Eqs. (3.59), (3.60) and (3.61) in Section 5 of this chapter).

3.2 QCD Radiation Amplitude

We are interested in the ratio of the total coherent sum of the single contributions to the full scattering process and their elastical part, considering colour factors as well. Before doing so, we investigate the φ -dependence of the radiation amplitude in general with the aim of finding a simplification for subsequent considerations.

The anticipation of φ -dependency in the total gluon radiation amplitude should show a symmetry around the projectile velocity direction, here chosen along the z-axis. But the following outline shows a weak dependence in contrast to this expectation.

In Fig. 3.1, the ratio of the total squared radiation amplitude Eq. (3.35) is exhibited for an arbitrary pair (ϑ, φ) divided by the amplitude for $\varphi = 0$. The gluon emission polar angle ϑ is fixed to $\vartheta = 2 \cdot 10^{-6}$ (upper panel) and $\vartheta = 0.1$ (lower panel) besides the fact of various tiny effective gluon masses ω_0 . The kinematical input obeys the condition $|\vec{q}_\perp| > \omega$ allowing to reduce the total amplitude R_{total} to the post-emission contribution due to the dead cone effect. If we apply this approach to the approximated matrix elements which are given in the previous section, it effectively yields for the ratio

$$\begin{aligned} \frac{R_{total}(\vartheta, \varphi)}{R_{total}(\vartheta, \varphi = 0)} - 1 &\approx \frac{R_{post}(\vartheta, \varphi)}{R_{post}(\vartheta, \varphi = 0)} - 1 \\ &= \left((\vec{k}_\perp - x\vec{q}_\perp)^2 + \mathcal{O}(m^2) + \mathcal{O}(\omega_0^2) \right)^{-1} \\ &= \frac{\omega^2 \sin^2 \vartheta + x^2 \vec{q}_\perp^2 - 2xq_x \omega \sin \vartheta}{(\vec{k}_\perp - x\vec{q}_\perp)^2}. \end{aligned} \quad (3.35)$$

Now, the calculation of the zeros of (3.35) is given by

$$\begin{aligned} 0 &\stackrel{!}{=} 2x\vec{q}_\perp \vec{k}_\perp + \omega^2 \sin^2 \vartheta - 2xq_x \omega \sin \vartheta - \vec{k}_\perp^2 \\ &= \cos \varphi + \frac{q_y}{q_x} \sin \varphi - 1. \end{aligned} \quad (3.36)$$

This relation has two solutions in the limit of small quark masses m and negligibly small screening parameters ω_0 :

$$\begin{aligned} \varphi_1 &= 0, \\ \varphi_2 &= \arcsin \left[\frac{2q_x q_y}{q_x^2 + q_y^2} \right] = 2 \cdot \varphi_m \end{aligned} \quad (3.37)$$

with the definition of a maximum angle $\varphi_m \equiv \arctan[q_y/q_x]$. Its importance is treated later on in Chapter 4 when we discuss divergences in the radiation amplitude.

Henceforth, we dedicate our attention to the radiation amplitude in QCD and firstly discuss the Abelian case.

3.2.1 Abelian Contributions

To highlight the relative importance of the triple gluon vertex diagram we consider the Abelian diagrams separately but keep the colour factors.

The Abelian total matrix element is found as sum of pre- and post-emission matrix elements

$$M_{1,rad}^{abel} = M_{1,0,0} + M_{1,1,0}. \quad (3.38)$$

If we use the approximated expressions (3.32) and (3.33) and the limit of small values of

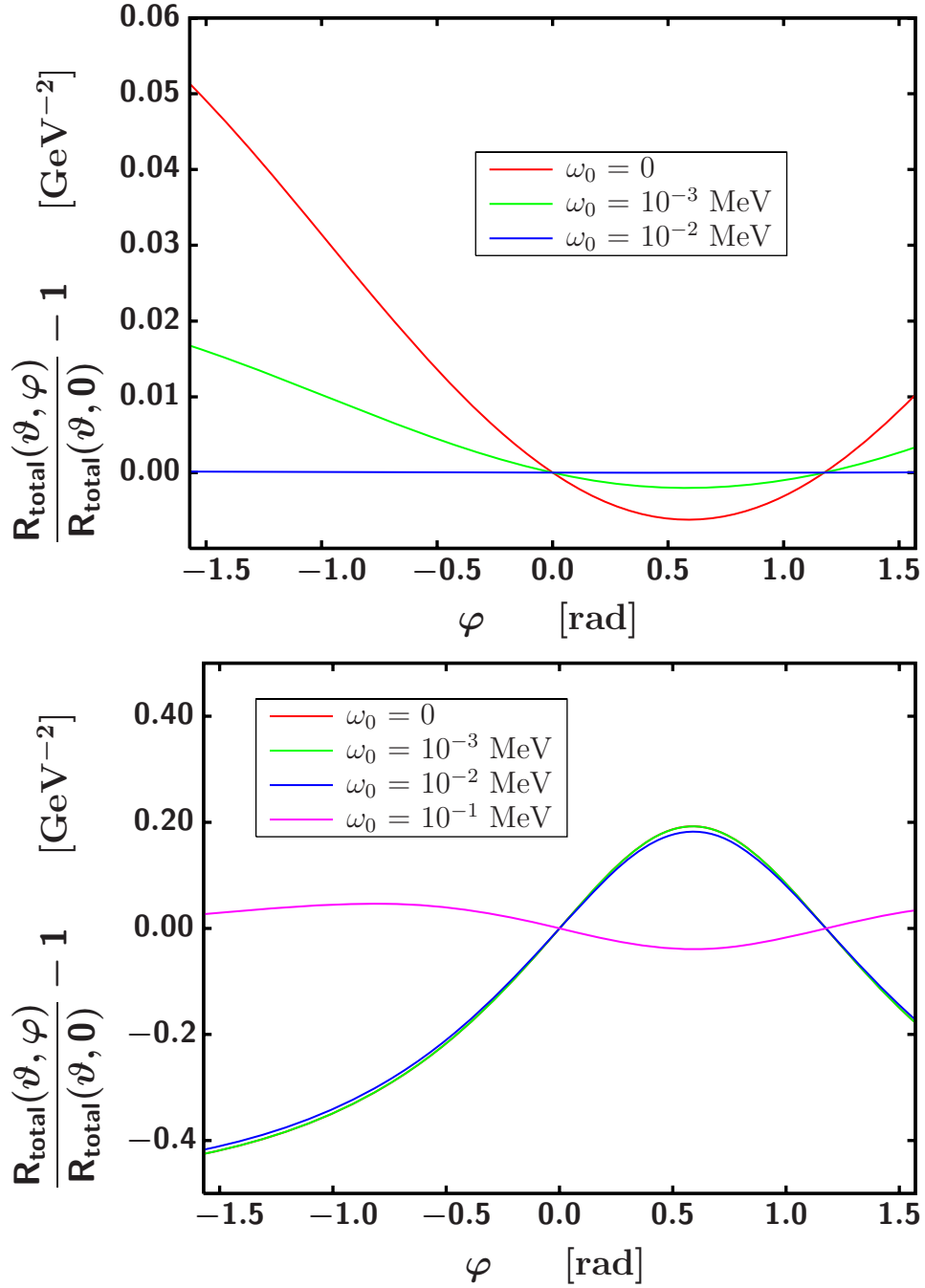


Figure 3.1: The relation $R_{total}(\vartheta, \varphi)/R_{total}(\vartheta, 0) - 1$ as a function of the azimuthal angle φ . The upper panel is calculated for $\vartheta = 2 \cdot 10^{-6}$, the lower panel its for $\vartheta = 0.1$. Both diagrams differ in the effective screening mass ω_0 . The curves intersect always at the same points, representing the initial and final quark emission angles φ . Used conditions are $\vec{p}_i = (0, 0, 10)$ GeV, $\vec{q}_\perp = (0.3, 0.2)$ GeV, $\omega = 1$ MeV, $\mu_D = 0.5$ GeV and $m = m_d$.

x , the sum of the amplitudes yields

$$M_{1,rad}^{abel} = \frac{M_{1,el}}{T_{A'B'}T_{C'D'}} \cdot (-2g) \cdot \left((T^f T^g)_{AB} T_{CD}^f \cdot \frac{\vec{\epsilon}_\perp \vec{k}_\perp}{\vec{k}_\perp^2 + x^2 m^2 + \omega_0^2} - (T^g T^f)_{AB} T_{CD}^f \cdot \frac{\vec{\epsilon}_\perp (\vec{k}_\perp - x \vec{q}_\perp)}{(\vec{k}_\perp - x \vec{q}_\perp)^2 + x^2 m^2 + \omega_0^2} \right). \quad (3.39)$$

Furthermore, the value q_\perp acts as a scale, also in form of $xq_\perp \ll k_\perp$ for small x and allows to reduce Eq. (3.39) to

$$M_{1,rad}^{abel} = \frac{M_{1,el}}{T_{A'B'}T_{C'D'}} \cdot (-2g) \cdot \frac{\vec{\epsilon}_\perp \vec{k}_\perp}{\vec{k}_\perp^2 + x^2 m^2 + \omega_0^2} \left((T^f T^g)_{AB} T_{CD}^f - (T^g T^f)_{AB} T_{CD}^f \right) \quad (3.40)$$

with a colour structure, which can be cast into a colour commutator

$$M_{1,rad}^{abel} = \frac{M_{1,el}}{T_{A'B'}T_{C'D'}} \cdot (-2g) \cdot \frac{\vec{\epsilon}_\perp \vec{k}_\perp}{\vec{k}_\perp^2 + x^2 m^2 + \omega_0^2} \cdot [T^f, T^g]_{AB} T_{CD}^f. \quad (3.41)$$

This exactly leads us to the modified dead cone factor, which will be introduced later on in this thesis in Section 3.4. Thus, we obtain for the Abelian radiation amplitude

$$R_1^{abel} \propto 4g^2 \cdot \frac{\vec{k}_\perp^2}{(\vec{k}_\perp^2 + x^2 m^2 + \omega_0^2)^2} \cdot C_A \quad (3.42)$$

with an arising colour part from Eq. (C.17) in Appendix C. It is easy to see, that in the limit of vanishing quark and effective gluon masses the radiation amplitude becomes proportional to $1/k_\perp^2$ which is nothing else than the famous infrared divergence.

In some possible cases only the pre- or post-emission diagram becomes relevant and dominates over the non-Abelian contribution. Such a scenario modifies the Abelian radiation amplitude in the previously given limits to

$$R_{1,pre/post}^{abel} \propto 4g^2 \cdot \frac{\vec{k}_\perp^2}{(\vec{k}_\perp^2 + x^2 m^2 + \omega_0^2)^2} \cdot C_F. \quad (3.43)$$

It equals for pre- and post-emission contributions due to the identity

$$\overline{|(T^f T^g)_{AB} T_{CD}^f|^2} \equiv \overline{|(T^g T^f)_{AB} T_{CD}^f|^2}, \quad (3.44)$$

which is also explicitly calculated in Eq. (C.16).

3.2.2 Non-Abelian Contributions

Let us study now the total single scattering radiation amplitude in QCD by taking the additional three-gluon vertex diagram into account.

Before we start the derivation for the total amplitude we have to ask the question, in how far the non-Abelian diagram is relevant for the full result. The answer is given in [Tho05] and is formulated, shortly summarised, by the condition $q_\perp < \omega$ which relates the

gluon radiation energy ω to the fixed transverse momentum transfer q_\perp . In this restriction the non-Abelian diagram rules over the whole range of gluon emission angles ϑ in contrast to the opposite case of $q_\perp > \omega$. In this area, the three-gluon vertex diagram is suppressed by orders of magnitude compared to the Abelian contributions.

Within the full QCD result, derived within the approximations given in Section 3.1, the complete matrix element is

$$\begin{aligned}
M_{1,rad} &= M_{1,0,0} + M_{1,1,0} + M_{1,0,1} \\
&= \frac{M_{1,el}}{T_{A'B'}T_{C'D'}} \cdot (-2g) \cdot \left((T^f T^g)_{AB} T_{CD}^f \cdot \frac{\vec{\epsilon}_\perp \vec{k}_\perp}{\vec{k}_\perp^2 + x^2 m^2 + \omega_0^2} \right. \\
&\quad - (T^g T^f)_{AB} T_{CD}^f \cdot \frac{\vec{\epsilon}_\perp (\vec{k}_\perp - x \vec{q}_\perp)}{(\vec{k}_\perp - x \vec{q}_\perp)^2 + x^2 m^2 + \omega_0^2} \\
&\quad \left. - [T^f, T^g]_{AB} T_{CD}^f \cdot \frac{\vec{\epsilon}_\perp (\vec{k}_\perp - \vec{q}_\perp)}{(\vec{k}_\perp - \vec{q}_\perp)^2 + x^2 m^2 + \omega_0^2} \right). \tag{3.45}
\end{aligned}$$

Again, one finally obtains for the sum of matrix elements in connection with the polarisation sum the radiation amplitude

$$R_1 \propto 4g^2 \cdot \frac{(\vec{k}_\perp \vec{q}_\perp + x^2 m^2 + \omega_0^2)^2}{(\vec{k}_\perp^2 + x^2 m^2 + \omega_0^2)^2 (\vec{k}_\perp - \vec{q}_\perp)^2} \cdot C_A, \tag{3.46}$$

provided $k_\perp \gg xq_\perp$. Here, one can see in the denominator of Eq. (3.46) the influence of the modified dispersion relation which cuts off the gluon spectrum at small values of k_\perp in contrast to the vacuum case ($\omega_0 = 0$), where the total radiation amplitude becomes $R_1 \propto 1/k_\perp^2$, and in the limit of $k_\perp \rightarrow 0$ the dominant contribution comes from the three-gluon vertex diagram. Within this approach we can estimate the total radiation amplitude as

$$R_1 \propto 4g^2 \cdot \frac{\vec{q}_\perp^2}{(\vec{q}_\perp^2 + x^2 m^2 + \omega_0^2)^2} \cdot C_A, \tag{3.47}$$

as long as $q_\perp > k_\perp$, i.e. Abelian diagrams can be neglected in the small- k_\perp region.

This should give us the tool for estimating the plateau of the three-gluon vertex diagram for small gluon radiation angles ϑ on a qualitative level, see Fig. 3.2. In the limits of $\omega < q_\perp < \omega_0$ and omitting the factor $x^2 m^2$, Eq. (3.47) can be written as

$$\overline{|M_{1,0,1}|^2} \propto \overline{|M_{1,el}|^2} \cdot \frac{\vec{q}_\perp^2}{(\vec{q}_\perp^2 + \omega_0^2)^2}, \tag{3.48}$$

and, with $q_z^{(+)} \approx -\omega_0$ in leading order, yields

$$\overline{|M_{1,0,1}|^2} \propto \frac{1}{(\vec{q}^2 + \mu_D^2 + \omega_0^2)^2} \cdot \frac{q_\perp^2}{(q_\perp^2 + \omega_0^2)^2} = \frac{1}{(q_\perp^2 + \mu_D^2 + 2\omega_0^2)^2} \cdot \frac{q_\perp^2}{(q_\perp^2 + \omega_0^2)^2}, \tag{3.49}$$

since we consider the z-component of the momentum transfer in the denominator of the elastic amplitude.

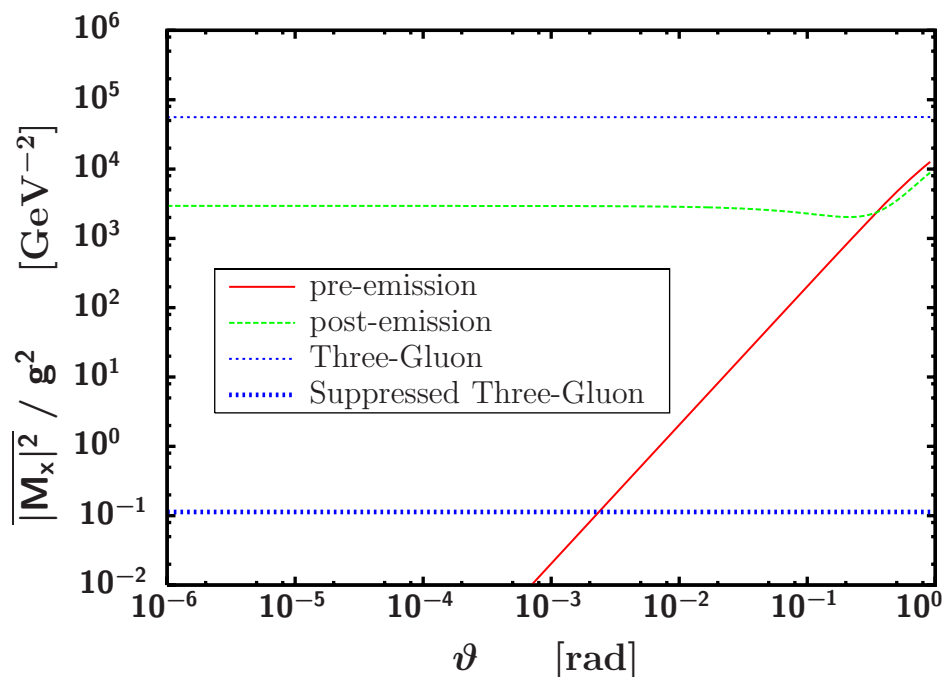


Figure 3.2: Contributions of individual diagrams to the total radiation amplitude as a function of small gluon emission angles ϑ . In the limits $\omega < q_\perp < \omega_0$, the three-gluon vertex diagram dominates and remains constant for small values of ϑ . Here, the ratio of suppression for this plateau (small blue dots) with $\omega_0^{(1)}$ is about 6 orders of magnitude larger compared to the strongly screened plateau (large blue dots) with $\omega_0^{(2)}$. This is due to the proportionality of $(1/\omega_0)^8$ (!) of the ratio in this limit. Here, we employ down-quark masses and $\omega = 1$ MeV, $\varphi = \pi/2$, $\vec{p}_i = (0, 0, 10)$ GeV, $\vec{q}_\perp = (0.3, 0.2)$ GeV, $\mu_D = 0.5$ GeV and $\omega_0^{(1)} = 0.02$ GeV, $\omega_0^{(2)} = 2$ GeV.

Now, we introduce a ratio K_1^2 as an expression for the amount of screening as comparison of non-Abelian diagram 1 to another diagram 2. It reads with Eq. (3.49) as

$$K_1^2 = \frac{\left(q_\perp^2 + \mu_D^2 + 2(\omega_0^{(1)})^2\right)^2 \left(q_\perp^2 + (\omega_0^{(1)})^2\right)^2}{\left(q_\perp^2 + \mu_D^2 + 2(\omega_0^{(2)})^2\right)^2 \left(q_\perp^2 + (\omega_0^{(2)})^2\right)^2} \approx \frac{(q_\perp^2 + \mu_D^2)^2 \cdot q_\perp^4}{4(\omega_0^{(2)})^8} \quad (3.50)$$

and, for example, one obtains in the scenario given in Fig. 3.2 a factor of $1/10^6$, which is so enormous due to the suppression of $(\omega_0)^8$ in the denominator of Eq. (3.50).

Further analysis of the complete situation for different sets of parameter relations are done in [Käm00] with vanishing quark masses m . In contrast to this, various effects of taking m into account but neglect the effective gluon mass ω_0 are discussed in [Tho03] in detail.

3.3 Dead Cone Factor with In-Medium Extension

The dead cone effect strongly reduces the emission probability in projectile direction, based on a factor which was introduced and popularised by Dokshitzer and Kharzeev [Dok01]. This dead cone factor considers the quark mass as a screening parameter and corrects the expression for the total radiation amplitude, firstly derived in the approach for massless projectile quarks in the high-energy limit by Gunion and Bertsch [Gun82]. It is also discussed for various scenarios in [Tho03].

Now, we take into consideration a surrounding medium which modifies the kinematic situation, thus screening effects by the effective parameter ω_0 become relevant. The significant term which yields the modified dead cone factor is given by the relation (3.42) for deriving the projectile emission contributions in the radiation amplitude. Thus, we take into account this dead cone factor in addition to the GB expression [Gun82] with the aim of considering finite quark- and gluon masses. Accordingly, we obtain for the dead cone factor

$$\tilde{F} = \frac{\vec{k}_\perp^2}{\vec{k}_\perp^2 + x^2 m^2 + \omega_0^2} \quad (3.51)$$

with the parameter x defined in (3.6), the projectile quark mass parameter m and the additional screening parameter ω_0 , referring to the polarisation of the medium. Expressed for arbitrary gluon emission angles ϑ the factor reads

$$F = \frac{\sin^2 \vartheta}{\sin^2 \vartheta + \frac{\vartheta_d^2}{4} \left(\cos \vartheta + \frac{1}{\sqrt{1 - \vartheta_p^2}} \right)^2 + \frac{\vartheta_p^2}{1 - \vartheta_p^2}} \quad \text{with} \quad \vartheta_p \equiv \frac{\omega_0}{k_0}, \quad (3.52)$$

where ϑ_p denotes the 'angle' with respect to the effective gluon mass, and $\vartheta_d \equiv m/E$ gives the usual form of the dead cone angle. It takes into account the quark mass and the energy E of the incident quark. Therefore, one can define an effective dead cone angle

$$\vartheta_{eff} = \sqrt{\vartheta_d^2 + \vartheta_p^2}. \quad (3.53)$$

Note that this relation is obtained in the soft gluon limit. If we assume $\vartheta_p \ll 1$ as another limit, the approximated dead cone factor alters to

$$F \approx \frac{\sin^2 \vartheta}{\sin^2 \vartheta + \vartheta_{eff}^2}, \quad (3.54)$$

which reveals the interplay of both effects. This is exhibited in the lower panel of Fig. 4.8 in Chapter 4 in which we compare with the scattering of massless quarks in vacuum, i.e. $F = 1$.

In Fig. 3.3, the probability for emitting a single gluon in dependence of different screening parameters is shown. The upper panel exhibits the influence of only the quark mass. With increasing mass the peak, and with this the dead cone, is shifted to larger angles. The other situation of decreasing masses yields a smaller magnitude of the radiation probability, which points to a reduction of the energy loss. One obtains the same suppression effect by a variation of ω_0 for light quarks, as shown in the lower panel of Fig. 3.3. Let us now inspect the influence of the screening parameter ω_0 in some detail which acts as effective gluon mass. In the upper panel of Fig. 3.4 the very important screening effect of ω_0 for radiating gluons in backward direction $\vartheta \rightarrow \pi$ is discussed. It is easy to see the relevance of a finite screening mass in this limit for the radiation angle: It reduces the divergence at $\vartheta = \pi$ due to the appearance of the denominator in Eq. (3.51). One may ask the question why the quark mass, also appearing in this denominator is not able to suppress this backward divergence. The answer is hidden in the parameter x (see Eq. (3.51)) proportional to m^2 , which equals to zero for $\cos \vartheta \rightarrow -1$ in the limit of $\vartheta_p^2 \ll 1$, meaning small ω_0 compared to the gluon energy ω . The visual proof that only the extreme cases of forward and backward gluon emission yield possibly a divergent behaviour of the total radiation amplitude is given in the lower panel of Fig. 3.4, where the whole range of ϑ is exhibited.

3.4 Kinematic Corrections

Now, the total radiation matrix element is calculated numerically and is also given an analytical approach with the same approximations as in Section 3.4. There, the latter approximation is done by a factorisation of the elastic amplitude and the inelastic contribution. This is only possible for the assumption of small components of the gluon four-momentum k , because k can be neglected compared to the momentum transfer q . Hence, in the case of non-vanishing gluon momenta, the radiation four-momentum transfer q_{rad} is given by

$$q_{rad} = (p_f|_{rad} - p_i) + k \equiv q_{el} + k. \quad (3.55)$$

If one factors out the denominator of the potential ansatz (see Eq. (2.1)) in the elastic amplitude, we add a kinematic factor

$$f_{kin} \equiv \frac{\vec{q}_{el}^2 + \tilde{\mu}^2}{\vec{q}_{rad}^2 + \tilde{\mu}^2} \quad (3.56)$$

to the total radiation amplitude in order to correct this factorisation. It contains only the spatial components of the momentum transfer due to the condition of vanishing energy transfer ($q_0 = 0$) in the Debye screened potential. Expressed in terms of transverse

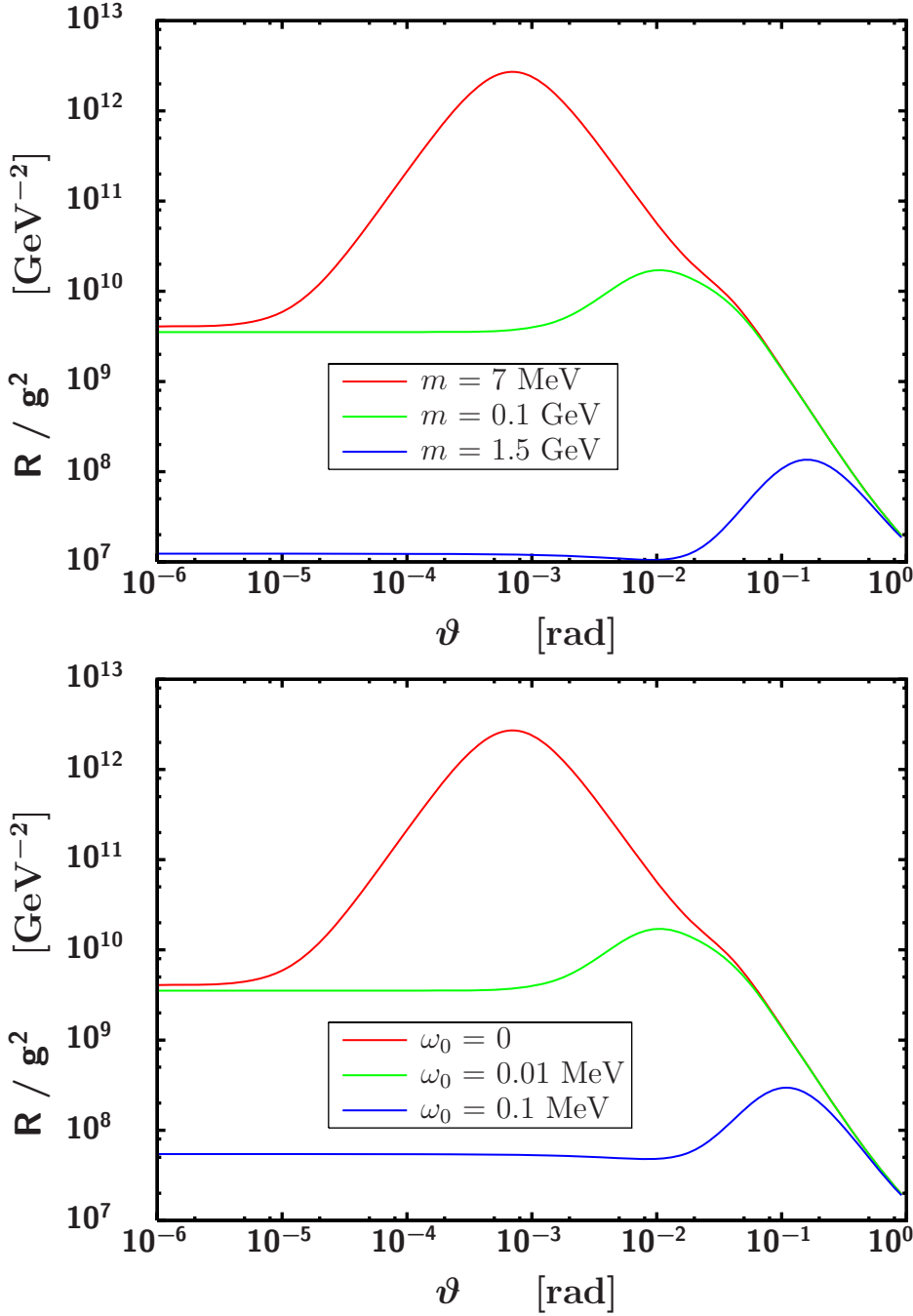


Figure 3.3: The total radiation amplitude R versus the gluon emission angle ϑ for different screening parameters ϑ_d and ϑ_p . The upper panel is calculated for different quark masses m without polarisation effects ($\omega_0 = 0$), whereas the lower panel exhibits various polarisation parameters with a fixed quark mass, $m = 7$ MeV. The radiation is suppressed at angles smaller than ϑ_{eff} - this is known as the dead cone effect. The used parameters in this figure are $\omega = 1$ MeV, $\varphi = \pi/2$, $\vec{p}_i = (0, 0, 10)$ GeV, $\vec{q}_\perp = (0.3, 0.2)$ GeV and $\mu_D = 0.5$ GeV.

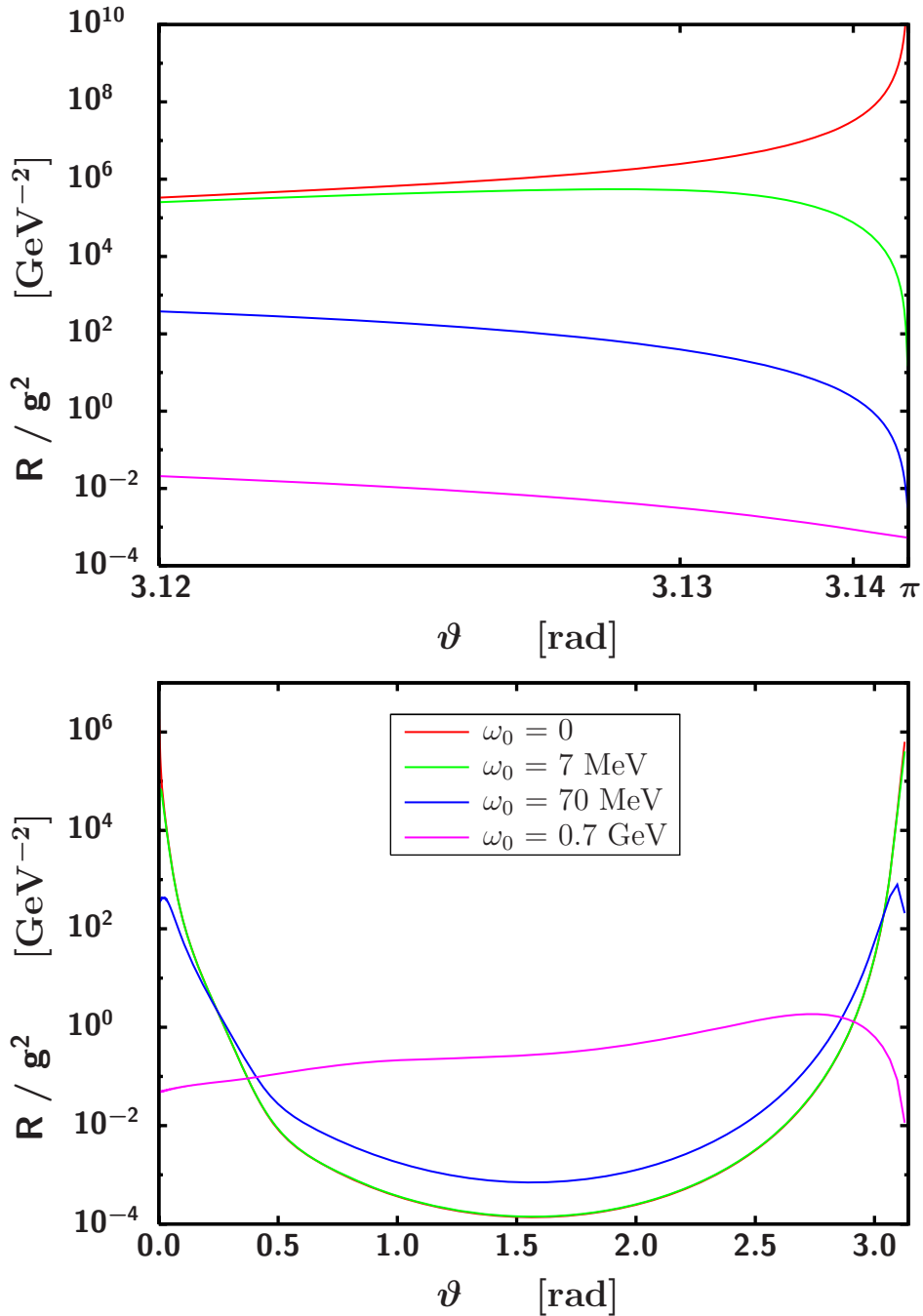


Figure 3.4: The total radiation amplitude R plotted as a function of the gluon emission angle ϑ for backward gluon radiation $\vartheta \rightarrow \pi$ (upper panel) and fixed quark mass $m = m_d$. Only for vanishing effective gluon mass ω_0 , a divergence at $\vartheta = \pi$ appears, otherwise it is screened by this effective parameter. In the lower panel the ϑ -dependence over the whole range from forward up to backward emission angles is shown. Here, we used additionally $\vec{q}_\perp = (0.03, 0.02)$ GeV and $\mu_D = 0.05$ GeV; parameters otherwise as in Fig. 3.3.

components $\vec{q}_{el} \equiv \vec{q}_\perp$ and \vec{k}_\perp , the correction factor is

$$f_{kin} = \frac{\vec{q}_\perp^2 + q_z^2 + \tilde{\mu}^2}{\vec{q}_\perp^2 + q_z^2 + \tilde{\mu}^2 + 2(\vec{q}_\perp \vec{q}_\perp + q_z k_z) + \omega^2}. \quad (3.57)$$

In the case of $\tilde{\mu}^2 > \omega^2$ the factor obeys $f_{kin} \rightarrow 1$ and no correction effect changes the radiation probability. This result is implemented in the plots in Chapter 4 for calculating numerically the relative radiated energy loss and compared with the analytical approach.

3.5 Gunion-Bertsch Limit of Quark-Quark Scattering

In this section we briefly outline the analytical results of Gunion and Bertsch (GB), who firstly discussed the problem of induced gluon radiation in the limit of high-energy quarks and soft gluon energies, based on real quark-quark scattering. Our aim in the next chapter is to compare the numerical results for quark-quark scattering with the potential model and use the extended GB approaches, which are given here, to understand our results qualitatively.

Gunion and Bertsch have used the A^+ - gauge and massless quarks with neglecting spin effects. We use the same notation as in [Gun82]³ for the momentum transfer $l = p'_f - p'_i$ only in this section. Anywhere else in this thesis, q is used as a naming for the momentum transfer. Additionally, the calculations are carried out in the CMS.

We start with the relevant expressions for the elastic quark-quark scattering, Fig. 2.2,

$$M_{elastic}^{GB} = C_{elastic} \cdot ig^2 \cdot \frac{(p_f + p_i)_\mu (p'_f + p'_i)^\mu}{(p_f - p_i)^2} = (T^f)_{AB} (T^f)_{CD} \cdot (-ig^2) \frac{2s}{\vec{l}_\perp^2}. \quad (3.58)$$

Here, the Mandelstam variable $s = 2p$ is used which holds only in the limit $m = 0$. This amplitude, obtained in absence of radiation contains of an infrared divergence, $\propto 1/\vec{l}_\perp^2$, which will be regulated by the additional effective mass ω_0 of the intermediate gluon. But it does not count for the total GB radiation amplitude due to the elastic part which is factorised out of the total matrix element.

For the inelastic contributions, the pre-projectile part reads as follows

$$\begin{aligned} M_{prePro}^{GB} &= C_{prePro} \cdot ig^3 \cdot \frac{(p_f + p_i - k)_\mu (p'_f + p'_i)^\mu \cdot (2p_i - k)_\nu \epsilon^\nu}{[(p_i - k)^2 - m^2] \cdot (p'_f - p'_i)^2} \\ &= \frac{M_{elastic}^{GB}}{C_{elastic}} \cdot (T^f T^g)_{AB} (T^f)_{CD} \cdot (-2g)(1-x) \cdot \frac{\vec{\epsilon}_\perp \vec{k}_\perp}{\vec{k}_\perp^2}, \end{aligned} \quad (3.59)$$

corresponding to Fig. 2.3. With referring to this, we obtain for the post-projectile contribution

$$\begin{aligned} M_{postPro}^{GB} &= C_{postPro} \cdot ig^3 \cdot \frac{(p_f + p_i + k)_\mu (p'_f + p'_i)^\mu \cdot (2p_f + k)_\nu \epsilon^\nu}{[(p_f + k)^2 - m^2] \cdot (p'_f - p'_i)^2} \\ &= \frac{M_{elastic}^{GB}}{C_{elastic}} \cdot (T^g T^f)_{AB} (T^f)_{CD} \cdot (-2g)(1-x) \cdot \frac{-\vec{\epsilon}_\perp (\vec{k}_\perp - x \vec{l}_\perp)}{(\vec{k}_\perp - x \vec{l}_\perp)^2}. \end{aligned} \quad (3.60)$$

³Please also be careful with relations including q_\perp . GB unusually occupied the gluon momentum with such a variable; we do so for k_\perp in common.

The expression for the non-Abelian three-gluon vertex contribution is written as

$$\begin{aligned}
M_{threeGlu}^{GB} &= C_{threeGlu} \cdot \frac{ig^3}{(p_i - p_f)^2 \cdot (p'_i - p'_f)^2} \\
&\times [(p_f + p_i)^\mu \epsilon_\mu \cdot (p_i - p_f + k)^\nu (p'_f + p'_i)_\nu \\
&+ (p_f + p_i)^\mu (p'_f - k - p'_i)_\mu \cdot (p'_f + p'_i)^\nu \epsilon_\nu \\
&+ (p'_i - p'_f - p_i + p_f)^\mu \epsilon_\mu \cdot (p_f + p_i)^\nu (p'_f + p'_i)_\nu] \\
&= \frac{M_{elastic}^{GB}}{C_{elastic}} \cdot if_{egf}(T^e)_{AB}(T^f)_{CD} \cdot (-2g)(1-x) \cdot \frac{\vec{\epsilon}_\perp(\vec{k}_\perp - \vec{l}_\perp)}{(\vec{k}_\perp - \vec{l}_\perp)^2},
\end{aligned} \tag{3.61}$$

with corresponds to Fig. 2.5.

Finally, we give the relevant expressions for gluon emission from the target line, depicted in Fig. 2.4. They read

$$M_{preTar}^{GB} = (T^f)_{AB}(T^f T^g)_{CD} \cdot ig^3 \cdot \frac{(p'_f + p'_i - k)_\mu (p_f + p_i)^\mu \cdot (2p'_i - k)_\nu \epsilon^\nu}{[(p'_i - k)^2 - m'^2] \cdot (p_f - p_i)^2} = 0. \tag{3.62}$$

Please note that in the considered case the predicted GB result in Eq. (3.62) equals zero due to the relation $p'_i \epsilon = 0$ in the limit of a target quark at rest.

The post-target contribution is

$$\begin{aligned}
M_{postTar}^{GB} &= C_{postTar} \cdot ig^3 \cdot \frac{(p'_f + p'_i + k)_\mu (p_f + p_i)^\mu \cdot (2p'_f + k)_\nu \epsilon^\nu}{[(p'_f + k)^2 - m'^2] \cdot (p_f - p_i)^2} \\
&= \frac{M_{elastic}^{GB}}{C_{elastic}} \cdot (T^f)_{AB}(T^g T^f)_{CD} \cdot (-2ig^3) \cdot \frac{\vec{\epsilon}_\perp \vec{l}_\perp (2-x)(x-1)}{x(\vec{k}_\perp - \vec{l}_\perp)^2}.
\end{aligned} \tag{3.63}$$

Within the GB approach, the contributions from radiation off the target lines to the total matrix element are neglected. With accounting the limits $m, m' \rightarrow 0$ and $x \rightarrow 0$ the total GB radiation amplitude finally yields

$$\frac{M_{total}^{GB}}{M_{elastic}^{GB}} = \frac{if_{efg}(F^e)_{AB}(F^f)_{CD}}{C_{elastic}} \cdot 2g \left(\frac{\vec{\epsilon}_\perp \vec{k}_\perp}{\vec{k}_\perp^2} - \frac{\vec{\epsilon}_\perp(\vec{k}_\perp - \vec{l}_\perp)}{(\vec{k}_\perp - \vec{l}_\perp)^2} \right), \tag{3.64}$$

coinciding with Eq. (15) in [Gun82]. A singularity is found in the equation above (but only in the absence of a surrounding medium) due to a divergent part, $(p_f - p_i)^2$, arising from the pre-target, post-target and three-gluon contributions. This agrees with the condition $\vec{l}_\perp = \vec{k}_\perp$, and Eq. (3.64) can be regularised to

$$M_{total}^{GB,reg} \propto \frac{\vec{\epsilon}_\perp \vec{k}_\perp}{\vec{k}_\perp^2 + \omega_0^2} - \frac{\vec{\epsilon}_\perp(\vec{k}_\perp - \vec{l}_\perp)}{(\vec{k}_\perp - \vec{l}_\perp)^2 + \omega_0^2}, \tag{3.65}$$

which corresponds in principle to Eq. (7) in [Käm00] and Eq. (58) in [Wan95]. Hence, the medium effect screens both divergences, $k_\perp^2 = 0$ and $\vec{k}_\perp = \vec{l}_\perp$, with the effective gluon mass ω_0 , implemented only via the fundamental dispersion relation for gluons propagating in a medium.

4 Radiative Energy Loss

The main results of the numerical code are presented in the following. We compute the radiative energy loss for various conditions and in different dependencies. Additionally, we take attention on the individual contributions to the total amplitude and appropriate integration boundaries to the numerical integration process. Comparisons to analytical approaches and results of other groups will constitute a conclusive framework of the thesis.

4.1 Divergences

A crucial treatment of radiative energy loss is to handle divergences¹ appearing in the non-Abelian contribution to the total amplitude and after all in the target gluon radiations as well.

The critical terms in form of $(p_i - p_f)^2$ in the denominator of the single three-gluon contribution Eq. (3.61) as well as the contributions of the pre- and post-target emission need special consideration, see Eq. (3.62) and Eq. (3.63) - preliminary derived in the absence of the surrounding medium. Fortunately, we can approach the relevant expression in the potential model with a Taylor expansion

$$M_{1,0,1}(\omega, \vartheta, \varphi) \propto \frac{1}{(p_i - p_f)^2} \approx -\frac{p_{i_z} - \omega}{p_{i_z}(\vec{q}_\perp - \vec{k}_\perp)^2} \quad (4.1)$$

in the limit of small projectile quark masses; ω denotes again the gluon energy. Hence, we obtain with the proper definition of the gluon four-momentum vector the maximum parameter set (φ_m, ϑ_m) as

$$\tan \varphi_m = \frac{q_y}{q_x}, \quad (4.2)$$

$$\sin \vartheta_m^{(1)} = \frac{|\vec{q}_\perp|}{\omega} \quad \text{and} \quad \vartheta_m^{(2)} = \pi - \vartheta_m^{(1)}. \quad (4.3)$$

After squaring the three-gluon matrix element, these two peaks in general are exhibited in Figs. 4.1 and 4.2 for different, but fixed values of ω and q_\perp . It is clearly to be seen, that in Fig. 4.2 the two real maxima shrink to only one maximum due to the special choice of parameters and so displaying the interplay between the gluon energy and the transverse momentum transfer, as demonstrated in Eq. (4.3).

¹A further possibility for treating divergences of the infra-red problem is the Bloch-Nordsieck trick to deal with soft divergences and the Kinoshita-Lee-Nauenberg theorem for collinear singularities, see [Kin62, Lee64].

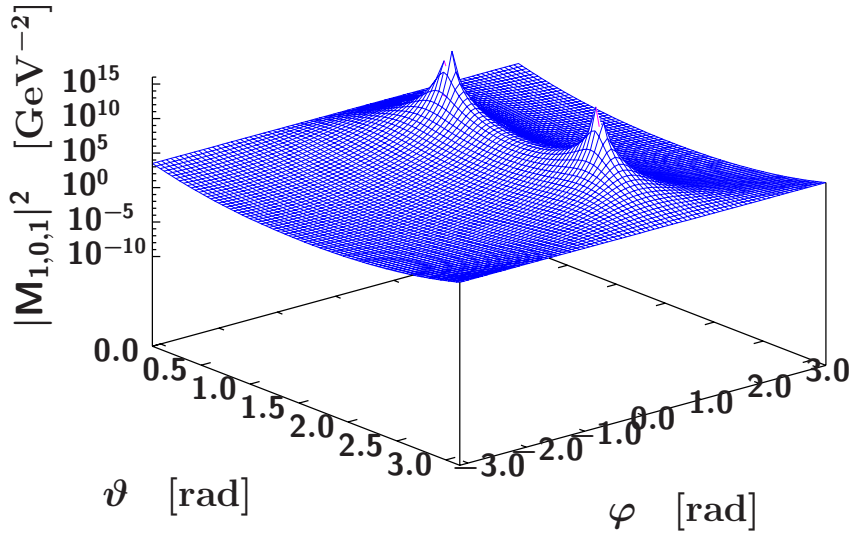


Figure 4.1: The approximated squared non-Abelian three-gluon vertex radiation amplitude as a function of the polar and azimuthal gluon emission angles ϑ resp. φ with a constant value $\vec{p}_i = (0, 0, 10)$ GeV. Here, we fix the parameter to $\vec{q}_\perp = (0.3, 0.2)$ GeV and $\omega = 0.5$ GeV. Two real peaks indicate singularities at $\vartheta_m^{(1)}$ and $\vartheta_m^{(2)}$ are obvious on a special φ_m -line, symmetric to $\vartheta = \pi/2$.

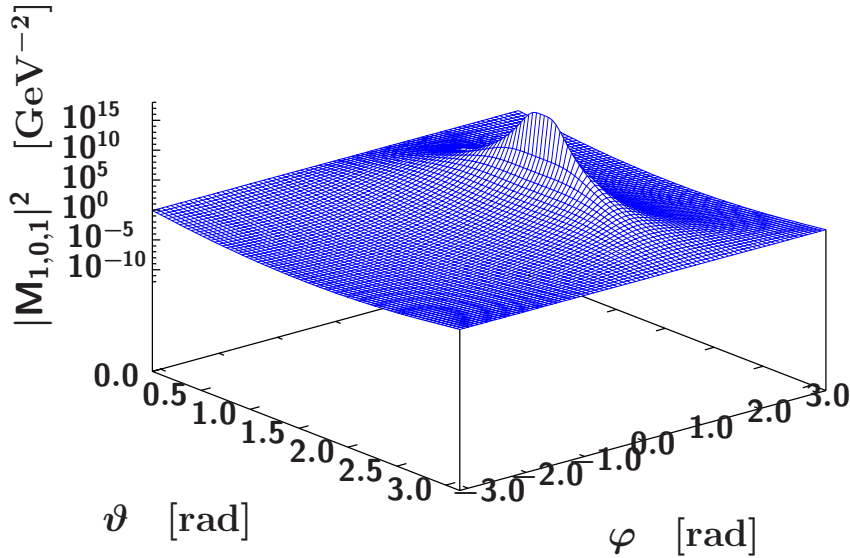


Figure 4.2: The same representation as in the Fig. 4.1, but for $\vec{q}_\perp = (0.6, 0.8)$ GeV and $\omega = 1$ GeV. This special set of parameters yields only a single peak pointing to a divergence at $\vartheta_m^{(1)} = \vartheta_m^{(2)} = \pi/2$, as expected.

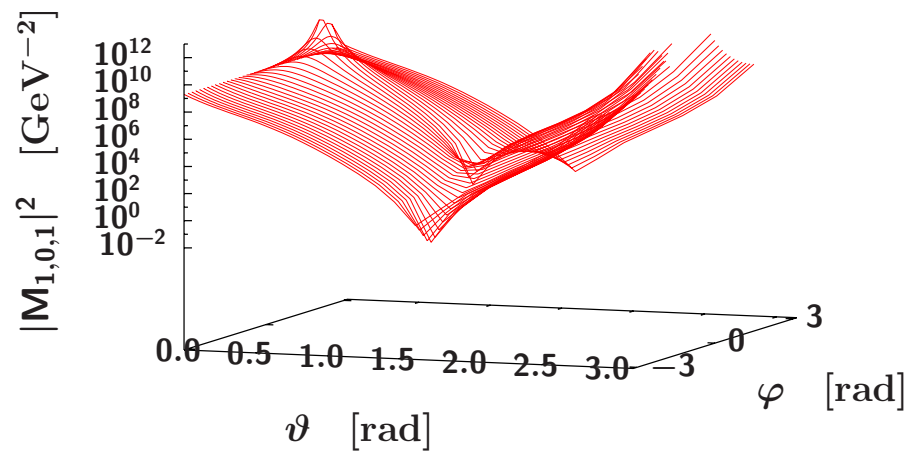


Figure 4.3: The 3d-performance of the numerically computed three-gluon vertex amplitude as a function of the gluon emission angles ϑ and φ for a fixed value of $\omega = 1.17$ GeV but without a screening parameter ω_0 . Despite the complex structure of the exact non-Abelian contribution, it is easy to verify at least one of the two real singularities in the expected point. Again, we calculate with $\vec{p}_i = (0, 0, 10)$ GeV, $\vec{q}_\perp = (0.3, 0.2)$ GeV and $\mu_D = 0.5$ GeV.

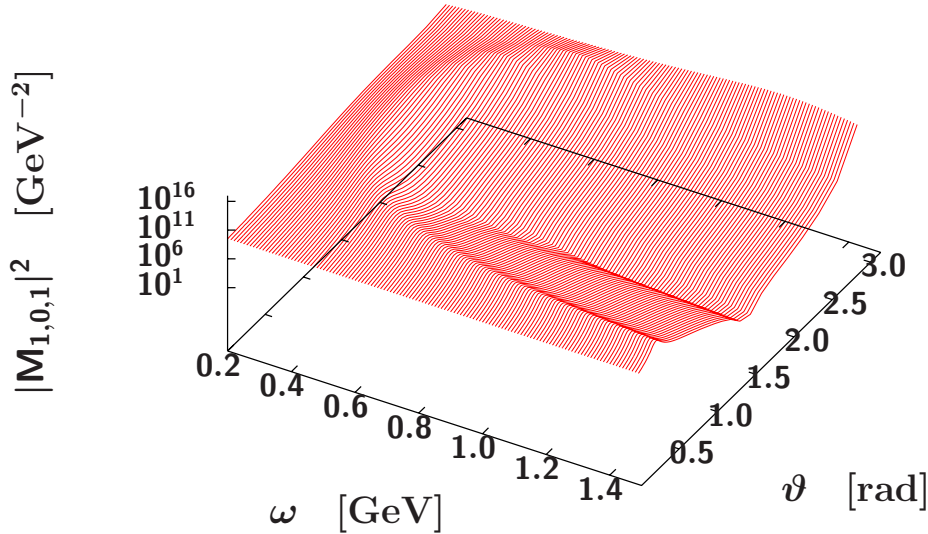


Figure 4.4: Similarly to Fig. 4.3, the same numerically calculated amplitude is shown but now as a function of the gluon energy ω and the gluon emission angle ϑ for an identical set of parameters. Here, the fixed value is $\varphi = \varphi_m = 0.98$, and one can see that the divergences in 4.1 finally fall together at a gluon energy of $\omega = |\vec{q}_\perp| = 0.36$.

Of course, we have to testify the analytical predictions with our numerical code. This is confirmed in the Figs. 4.3 and 4.4 impressively, but no effects of quark mass and effective gluon mass are taken into account, yet.

Our aim should be handling and avoiding singularities. Subsequently, we consider an effective gluon mass and additionally quark masses. It is not a surprise that with these screening parameters the divergences vanishes and become suppressed effectively due to the additional appearance in the denominator of Eq. (3.47). Another power of ω_0 is a small peak-shift to higher gluon frequencies in the limit of $\omega_0 < q_\perp$, while the transverse momentum transfer accounts again as a scale. In spite of this, much smaller changes are effected by the quark mass m . It is also implemented in the denominator of Eq. (3.47), as anticipated. In contrast to ω_0 , the quark mass is combined with the parameter x which simply explains this tiny effect of suppression and shift of the regularised divergence.

4.2 Gluon Distribution

It is essential to the integration over phase space to clarify the role of the integrand function. Firstly, we focus on the gluon distribution itself which is represented in gluon rapidities and transverse momenta, in agreement with literature [Mus97, Wan95, Xia04].

In light-cone coordinates the definition of the rapidity reads

$$y \equiv \frac{1}{2} \ln \left(\frac{k^+}{k^-} \right) = \frac{1}{2} \ln \left(\frac{k_0 + k_z}{k_0 - k_z} \right) = \frac{1}{2} \ln \left(\frac{1 + \sqrt{1 - \vartheta_p^2} \cos \vartheta}{1 - \sqrt{1 - \vartheta_p^2} \cos \vartheta} \right), \quad (4.4)$$

with $\vartheta_p = \omega_0/k_0$ and the proper representation of k_μ . Please note that negative boost parameters refer to backward gluon scattering, whereas rapidities greater than zero are accompanied at forward gluon emission.

The probability of radiating a single gluon is simply expressed as an invariant radiation spectrum

$$R \equiv \omega \frac{dn_g}{d^3k} \approx x \frac{dn_g}{dx d^2k_\perp} = \frac{dn_g}{dy d^2k_\perp}, \quad (4.5)$$

for small values of x , where x is the fractional momentum carried by the radiated gluon relative to the maximum available in the way of confining the radiation to a uniform (central) rapidity region, which represent the most important zone in relativistic heavy-ion collisions. Note, that this midrapidity-plateau is in sharp contrast to the QED case where the radiation amplitude strongly depends on rapidity.

Subsequently, the relation above is used as the integration function, acting like the phase space distribution which has to be integrated. According to Eq. (4.5), Gunion and Bertsch delivered in [Gun82] a well-known analytical expression (see also explanations to Eq. (3.64) in Chapter 3) for gluon bremsstrahlung from quarks, assuming a factorisation of the elastic matrix element. The same holds true for our expanded GB radiation amplitude Eq. (3.65), while the different kinematical situation for elastic and inelastic scattering is recovered by the formal introduction of the kinematical correction factor f_{kin} in Section 3.6 in a medium.

Of course, we also encounter factorisation in our integration function computed with the numerical code. It is questionable if one is allowed to factorise out the elastic part of the amplitude from the inelastic part, meaning pre- and post emission diagrams from projectile- and target lines as well as the non-Abelian three-gluon contribution. We just follow the analytical representation of the radiation amplitude Eq. (3.46) and normalise to the elastic amplitude because the inelastic process can not happen without an elastic event, i.e. a mixture of both effects².

Possible problems of normalisation referring to the radiative energy loss are also discussed in the following section.

4.3 Average Energy Loss

4.3.1 Definition

It is not trivial to give a convincing concept for the radiative energy loss. Clearly, we have to weight the gluon distribution function and integrate over phase space. While going this way we orientate on work of Mustafa *et al.*, Gyulassy *et al.* and Wang *et al.* [Mus97, Gyu01, Wan95]. In order to find an estimate for the radiative energy loss per unit length we multiply the interaction rate $\Gamma = 1/\tau$ and the average energy loss per collision, Ω , which is calculated in terms of rapidity as

$$\Omega \equiv \langle n_g k_0 \rangle = \int dy d^2k_\perp \left(\frac{dn_g}{dy d^2k_\perp} \right) k_0 \Theta(\tau - \tau_f) \quad (4.6)$$

²This total separation of elastic- and inelastic contributions is discussed in Section 4.5 as well where higher orders in the collisional energy loss becomes relevant.

where Θ denotes the Heaviside function: $\Theta(x) = 0$ for $x < 0$ and $\Theta(x) = 1$ for $x > 0$. This further corrects the LPM effect by including a formation time restriction through the step function $\Theta(\tau - \tau_f)$. It automatically restricts the phase space of the emitted gluon in which the variable formation time $\tau_f(k_\perp)$ has to be smaller than the interaction time τ , requiring a separation between the radiated gluon and the parton from which it is emitted.

The average process in the definition of Eq. (4.6) refers to the average momentum transfer³ of the scattering event, which is defined as

$$\langle q_\perp^2 \rangle \simeq \langle q^2 \rangle \equiv \langle t \rangle = \frac{\int_{k_\perp^{min^2}}^{k_\perp^{max^2}} dt t \left(\frac{d\sigma_{el}}{dt} \right)}{\int_{k_\perp^{min^2}}^{k_\perp^{max^2}} dt \left(\frac{d\sigma_{el}}{dt} \right)}, \quad (4.7)$$

meaning that we try to find a relevant input parameter of the momentum transfer within its range. Hence, we have to specify the k_\perp -thresholds for this integration by following ideas in [Mus97]. Therefore, we choose the Debye screening mass of a pure gluon gas restricting the lower k_\perp boundary as

$$k_\perp^{min} = \mu_D \equiv \sqrt{4\pi\alpha_s T}, \quad (4.8)$$

where T is the system's temperature. Note, that the infrared divergence is also removed when we screen with an effective gluon mass ω_0 , as discussed in previous sections; but here, only the Debye mass as an effective parameter is used. Now, an expression for the maximum value of k_\perp is searched for. So, we compute the Mandelstam variable s with its definition as

$$s \equiv (p + p')^2 = (p_1 + p'_1 + k)^2 = m_Q^2 + 2k(p_1 + p'_1) \quad (4.9)$$

for quark scattering with one-gluon emission. We use the quark on-shell condition and vacuum gluon dispersion relation, $k^2 = 0$, i.e. put $\omega_0 = 0$. The average values are

$$\begin{aligned} \langle s \rangle &\approx m_Q^2 + 6ET, \\ \langle 1/s \rangle &= \frac{1}{2} \int \frac{d \cos \vartheta}{m_Q^2 + 2EE' - 2(E^2 - m_Q^2)E' \cos \vartheta} \\ &\approx \frac{1}{4(E^2 - m_Q^2)} \ln \left(\frac{m_Q^2 + 2EE' + 2(E^2 - m_Q^2)E'}{m_Q^2 + 2EE' - 2(E^2 - m_Q^2)E'} \right), \end{aligned} \quad (4.10)$$

where E and p are the energy and the four-momentum of the incoming heavy projectile quark and $p' \propto 3T$ is the average momentum of the light quark or gluon being a constituent of QGP. Then, k_\perp^{max} finally becomes

$$(k_\perp^{max})^2 = \frac{3ET}{2} - \frac{m_Q^2}{4} + \frac{m_Q^2}{48pT} \ln \left(\frac{m_Q^2 + 6ET + 6pT}{m_Q^2 + 6ET - 6pT} \right). \quad (4.11)$$

³In further relations the approximation $\langle q_\perp^2 \rangle \approx \langle q_\perp \rangle^2$ is used, according to the average squared momentum transfer. The expressions are not equivalent due to a generally distributed momentum transfer.

This result is obtained owing to the kinematic restriction of the transverse gluon momentum squared

$$(k_{\perp})^2 < \frac{(s - m_Q^2)^2}{4s}. \quad (4.12)$$

With the aim of an analytical integration of Eq. (4.7) the average transverse momentum transfer is expressed only in terms of integration boundaries k_{\perp}^{max} and k_{\perp}^{min} . Hence, this gives rise to the differential cross section for elastic scattering,

$$\frac{d\sigma_{el}}{dt} = \frac{|M(s, t)|^2}{16\pi [s - (m_Q + m_q)^2] [s - (m_Q - m_q)^2]}. \quad (4.13)$$

In the limits $m_q \ll m_Q$ and $|t| \ll s$, the cross section (4.13) can be approximated by

$$\frac{d\sigma_{el}}{dt} \propto \frac{1}{t^2}. \quad (4.14)$$

Thus, the analytic integration of Eq. (4.12) yields

$$\langle q_{\perp}^2 \rangle = \frac{3\alpha_s}{\pi} \frac{(k_{\perp}^{min})^2 (k_{\perp}^{max})^2}{(k_{\perp}^{max})^2 - (k_{\perp}^{min})^2} \ln \left[\frac{(k_{\perp}^{max})^2}{(k_{\perp}^{min})^2} \right], \quad (4.15)$$

with help of Eq. (4.14). Now, we are well prepared for our numerical calculation according to the momentum transfer input. We give the analytic result of Mustafa *et al.* [Mus97] for the radiative energy loss for completeness. With lots of severe approximations like, $q_0, k_{\perp} \gg q_{\perp}$ and $(k_{\perp}\tau)^2 \gg 1$, the average energy loss per collision is obtained as

$$\Omega = \frac{6\alpha_s}{\pi} \langle q_{\perp}^2 \rangle \tau \ln \left(\frac{k_{\perp}^{max}}{k_{\perp}^{min}} \right). \quad (4.16)$$

With taking into account the factor of the interaction rate Γ we finally obtain

$$\left(-\frac{dE}{dx} \right)_{rad} \approx \frac{3\alpha_s}{\pi} \frac{\mu_D^2 (k_{\perp}^{max})^2}{(k_{\perp}^{max})^2 - \mu_D^2} \ln^2 \left[\frac{(k_{\perp}^{max})^2}{\mu_D^2} \right] \quad (4.17)$$

as an approximated expression of the radiative energy loss for heavy quarks.

Now, our aim is the numerical integration of Eq. (4.6). For the sake of symmetry to the process of gluon emission as well as for a better imagination we use spherical coordinates in our code, and no rapidities. Thus, we must rewrite the energy loss per collision in the new coordinates. Using the approximation $k_0 \approx k_{\perp} \cosh y$ and an approximation for the formation time $\tau_f \approx \cosh y / k_{\perp}$, we get

$$\begin{aligned} \Omega &= \int_{\varphi_{min}}^{\varphi_{max}} d\varphi \int_{y_{min}}^{y_{max}} dy \Theta(\tau - \tau_f) \cosh y \int_{k_{\perp}^{min}}^{k_{\perp}^{max}} dk_{\perp} k_{\perp}^2 \left(\frac{dn_g}{dy d^2 k_{\perp}} \right) \\ &\approx \tau \int_{\varphi_{min}}^{\varphi_{max}} d\varphi \int_{k_{\perp}^{min}}^{k_{\perp}^{max}} dk_{\perp} k_{\perp}^3 \left(\frac{dn_g}{dy d^2 k_{\perp}} \right) \\ &= \tau \int_{\varphi_{min}}^{\varphi_{max}} d\varphi \int_{\vartheta_{min}}^{\vartheta_{max}} d\vartheta \sin^3 \vartheta \int_{k_{\perp}^{min}/\sin \vartheta}^{k_{\perp}^{max}/\sin \vartheta} d\omega \omega^4 \left(\frac{dn_g}{d^3 k} \right). \end{aligned} \quad (4.18)$$

Generically, the phase space intergal has to be three-dimensional. This seems to be not fulfilled in the second term of Eq. (4.18). Indeed, this issue is resolved by the fact that the variable pair (k_\perp, y) is not independent, in contrast to (ϑ, ω) . Admittedly, it nests the anyway complex integration structure. The restriction through the step function occurs in the integration boundaries over the special choice of the rapidity interval to the length of unity. Hence, the corresponding ϑ -restrictions read as $\vartheta_{min} = \pi/2$ and $\vartheta_{max} \approx 1/\sqrt{2}$ which refer to $y_{min} = 0$ and to $y_{max} = 1$, respectively. One interprets this restriction as a focus on the strongly peaked forward emission of gluons, as also suggested in [Djo03b] for isolating the energy of the near-side jet.

Finally, the integration procedure for the resulting radiative energy loss is based on the relation

$$\left(-\frac{dE}{dx}\right)_{rad} = \frac{1}{2(2\pi)^3} \int_0^{2\pi} d\varphi \int_{\vartheta_{min}}^{\vartheta_{max}} d\vartheta \sin^3 \vartheta \int_{k_\perp^{min}/\sin \vartheta}^{k_\perp^{max}/\sin \vartheta} d\omega \omega^4 \frac{|M_{inel}|^2}{|M_{el}|^2}. \quad (4.19)$$

We give a brief comment to the normalisation problem referring to the energy loss. A naïve definition of the total averaged gluon energy is

$$\begin{aligned} \langle k_0 \rangle &\equiv \frac{\int d^2q_\perp d^3k \frac{d\sigma}{d^2q_\perp d^3k} k_0(q_\perp, k)}{\int d^2q_\perp d^3k \frac{d\sigma}{d^2q_\perp d^3k}} = \frac{\int d^2q_\perp d^3k \left(\frac{d\sigma_{el}}{d^2q_\perp}\right) \left(\frac{dn_g}{d^3k}\right) k_0(q_\perp, k)}{\int d^2q_\perp d^3k \left(\frac{d\sigma_{el}}{d^2q_\perp}\right) \left(\frac{dn_g}{d^3k}\right)} \\ &= \frac{\int d^2q_\perp \left[\left(\frac{d\sigma_{el}}{d^2q_\perp}\right) \int d^3k \left(\frac{dn_g}{d^3k}\right) k_0(q_\perp, k) \right]}{\int d^2q_\perp \left[\left(\frac{d\sigma_{el}}{d^2q_\perp}\right) \int d^3k \left(\frac{dn_g}{d^3k}\right) \right]}, \end{aligned} \quad (4.20)$$

with the assumption of a factorisation of the elastic cross section out of the total cross section. Furthermore, we use the general independence of the gluon momentum k in the elastic scattering amplitude. Now, we fix for simplicity (instead of an integration over q_x) an average transverse momentum transfer as an input parameter which completely separates the radiation part from the elastic one. It also happens that the averaging procedure for q_\perp consists of a normalisation in the elastic contribution, see Eq. (4.7). Considering the previous ideas it follows

$$\langle k_0 \rangle = \frac{\int d^3k \left(\frac{dn_g}{d^3k}\right) k_0(q_\perp, k)}{\int d^3k \left(\frac{dn_g}{d^3k}\right)}, \quad (4.21)$$

where the denominator normalises the whole expression in the background of an arbitrary number of emitted gluons. But here only the energy loss per single emission is taken into account, i.e. the denominator is set to one and the effect of multiple collisions is totally recovered by multiplying the interaction rate Γ with Eq. (4.21), which is valid for a single collision. Indeed, we have to add a restriction of the one-gluon spectrum (LPM effect) in

the integrand referring to only a single collision which is expressed as an additional step function. Hence, we obtain for the radiative energy loss per collision

$$\left(-\frac{dE}{dx}\right)_{rad} \simeq \int d^3k \left(\frac{dn_g}{dyd^2k_\perp}\right) k_0 \Theta(\tau - \tau_f), \quad (4.22)$$

where the formation time $\tau_f(k)$ in the integration boundaries as well as the integration function enter. This expression corresponds to the definition Eq. (4.6) and lets trace back the origin of Eq. (4.17) in a better way.

4.3.2 Integration over Phase Space Distribution

Firstly, we consider another problem before special results of radiative energy loss are presented. A general point of discussion is the consideration of the input momentum transfer \vec{q} , respectively the x- and y-components of this spatial vector⁴. Usually, one has the freedom of fixing both parameters by accounting for the kinematical thresholds of the particular scattering process. To survey the dependence on $q_{x,y}$, one can use as a first simplification the special relation

$$\begin{aligned} q_x &\equiv q_x(\gamma) = |\vec{q}_\perp| \cos \gamma, \\ q_y &\equiv q_y(\gamma) = |\vec{q}_\perp| \sin \gamma, \end{aligned} \quad (4.23)$$

with a range of $0 \leq \gamma \leq 2\pi$. In this way, the true independent variables q_x and q_y are mapped to one variable γ . This behaviour is checked in Fig. 4.5, where integrated sum and squared total matrix element versus the polar angle γ is shown. This plot confirms our conjecture which leads to the fact that the total radiation amplitude only depends on terms of total transverse momentum transfer after integration in the $(\vartheta, \varphi, \omega)$ phase space. It is explained as follows: The dominating part to the radiative energy loss is delivered by the non-Abelian diagram, while integrating over a large range of gluon energies ω , e.g. the total radiation amplitude is approximated well by the three-gluon vertex. Hence, the divergences play an important role which are regulated over the screening parameter ω_0 . This occurs at a fixed emission angle $\varphi = \varphi_m$, and one obtains a dependency on $|\vec{q}_\perp|$ only instead on the single components of \vec{q}_\perp . This simplifies the kinematics in such a way that we are free in the choice of the special q_\perp -direction, for example assuming a vanishing y-component of the momentum transfer in all numerical and analytical calculations.

The induced energy loss is now investigated for quark-quark scattering processes but with neglecting target contributions. At the beginning we consider the fractional energy loss for different fixed values of the transverse momentum transfer q_\perp in a numerical computation, see Fig. 4.6. One can easily elucidate the different behaviour for different input values of q_\perp when we use Eq. (4.16). For maximum momentum transfer, the relation $\Delta E/E \propto \ln E$ is obtained what lets grow the energy loss for increasing projectile energies, whereas the minimum value leads to $\Delta E/E \propto \ln E/E$ and yields a weak suppression effect for higher energies.

A direct comparison of analytical approaches given in the previous chapter with implementing results of [Mus97] and adapted numerical calculation is exhibited in Fig. 4.7. In this figure, the quantitative dependence of the essential screening parameter ω_0 is at-

⁴The z-component does not play any role as a fixed parameter. It is calculated from the setting of q_x and q_y .

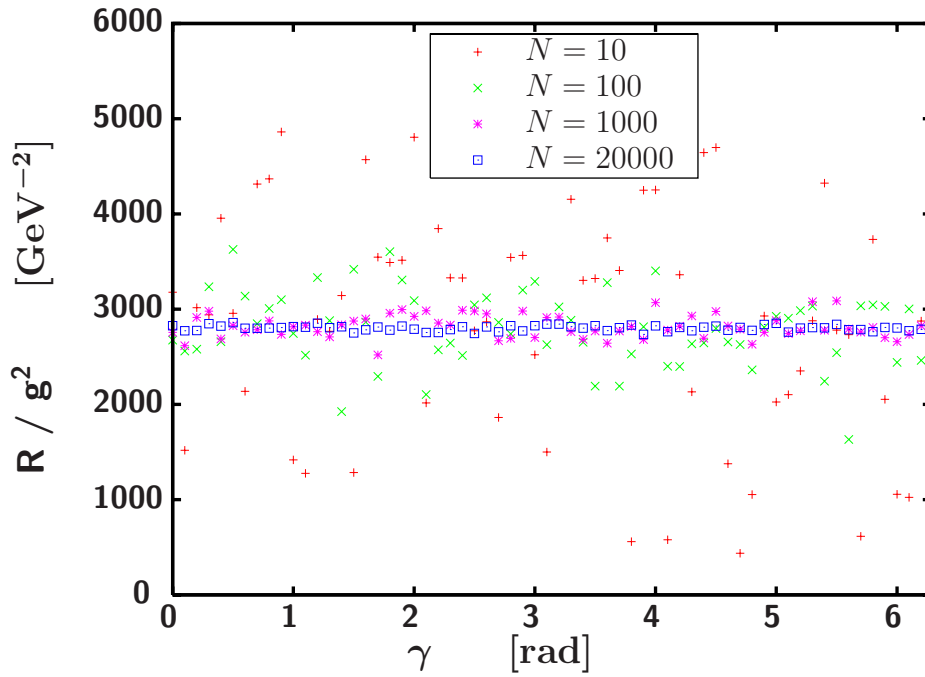


Figure 4.5: The summed, squared and averaged integrated total radiation amplitude R as a function of the polar angle γ for increasing integration accuracy determined by the number of Monte Carlo steps N at a constant value of $|\vec{q}_\perp| = 3.6$ GeV. One obtains the same result (i.e. the independence of $R g^{-2}$ of γ) with other sets of kinematical parameters, too. Calculation is done for $m = m_d$, $\omega_0 = 0.1$ GeV and $\mu_D = 0.5$ GeV. The particular choice of the integration boundaries does not influence this behaviour.

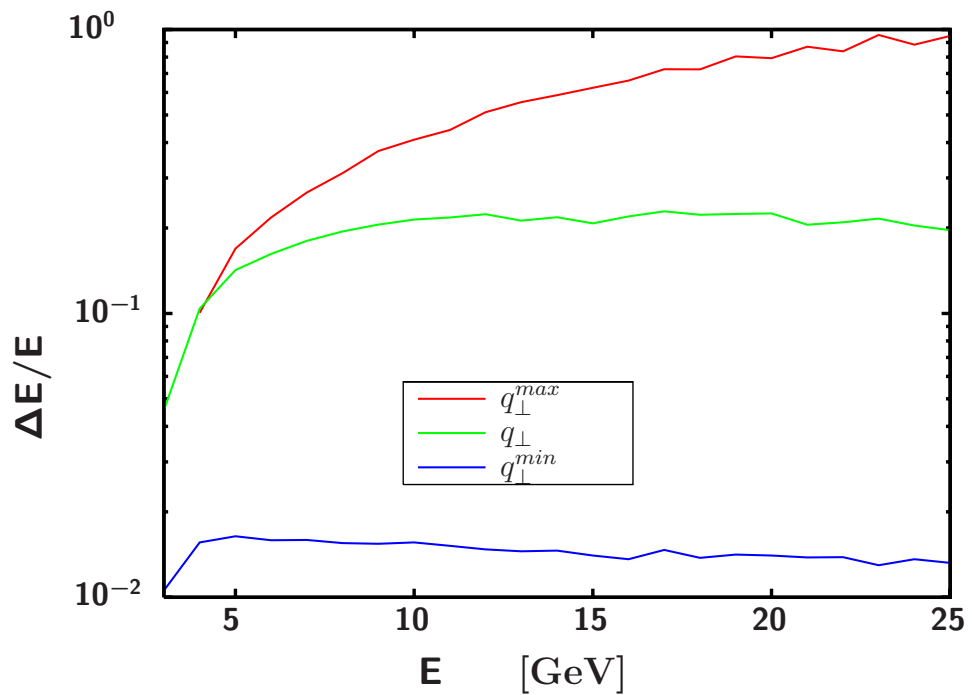


Figure 4.6: The relative energy loss in charm quark-charm quark scattering for various input parameters q_{\perp} : $q_{\perp} = k_{\perp}^{max}$ (red line), $q_{\perp} = 0.7$ (green line) and $q_{\perp} = k_{\perp}^{min}$ (blue line) as a function of the projectile quark energy. The curve standing for the maximum value of q_{\perp} shows a different behaviour due to the proportionality $k_{\perp}^{max} \propto E$ compared to the other lines. The screening parameter reads as $\omega_0 = 0.2$ GeV.

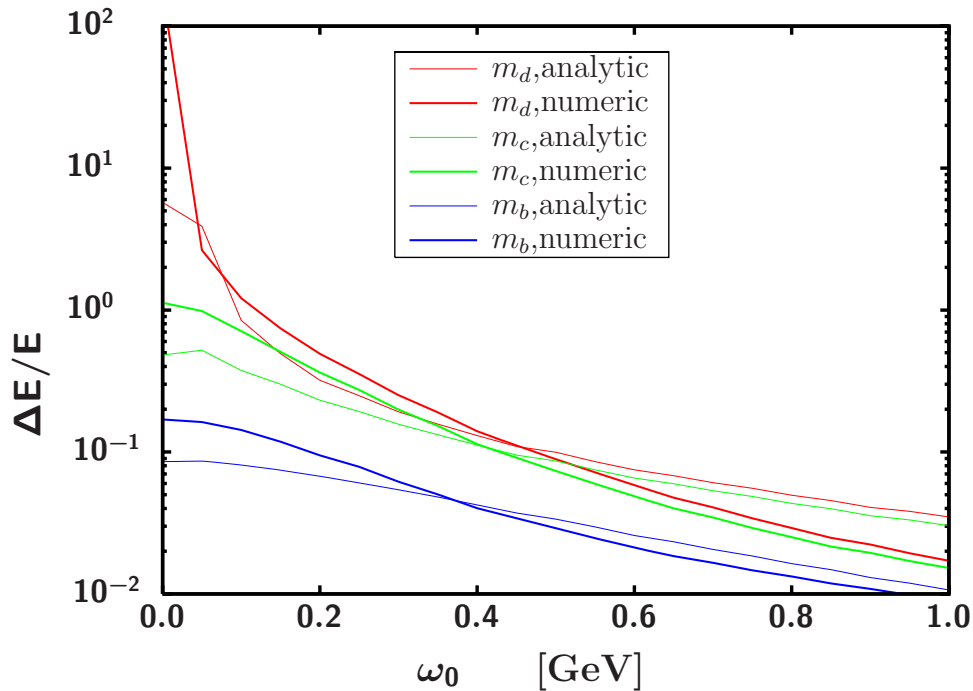


Figure 4.7: The relative radiative energy loss in potential model as a function of the effective gluon mass ω_0 . Here, numerical (thick lines) and analytical (thin lines) calculations are depicted for various quark masses and a fixed energy of $E = 10$ GeV. In the region of $\omega_0 \approx 0.4$ GeV, the analytical and numerical results meet each other.

tended, here for fixed initial quark energy E of 10 GeV in the potential model⁵. Only a small screening area of $0.2 \text{ GeV} < \omega_0 < 0.6 \text{ GeV}$ appears to be sensible according to the strength of suppression, especially the three-gluon vertex radiation amplitude. Furthermore, it confirms the assumption of a critical increase for small screenings which explains the unphysical behaviour in this region, as expected for the light quarks. For the sake of completeness, we refer the interested reader to a prediction made in Fig. 5 of [Xia04]. There, a strong suppression effect of taking into account the dead cone factor additionally compared to the result without the dead cone effect is observed. This is definitely not the case as shown in both panels of Fig. 4.8, even not if we add the modified dead cone factor for in-medium extension!

In this connection, we depict the projectile contributions compared with the Abelian ones in Fig. 4.9. The projectile diagrams dominate in this special choice of parameter set over the non-Abelian three-gluon vertex diagram and confirms the assumption of a factor $C_A/C_F = 9/4$ which has to be multiplied the pre- or post projectile diagram to yield the Abelian amplitude. This only works in the limit of small x and is based on Eqs. (3.42) and (3.43) as outlined in Chapter 3.

The choice of the integration boundaries is not trivial, in particular, the range of ϑ . This is demonstrated in Fig. 4.10 where the single contributions to the total radiation amplitude for quark-quark scattering (qq) are exhibited in form of the relative energy loss as well as a comparison between qq scattering and the potential model. It is obvious that

⁵Of course, in the analytic results we implement a kinematical correction factor as well as the medium-extended dead cone factor, as introduced in Chapter 3.

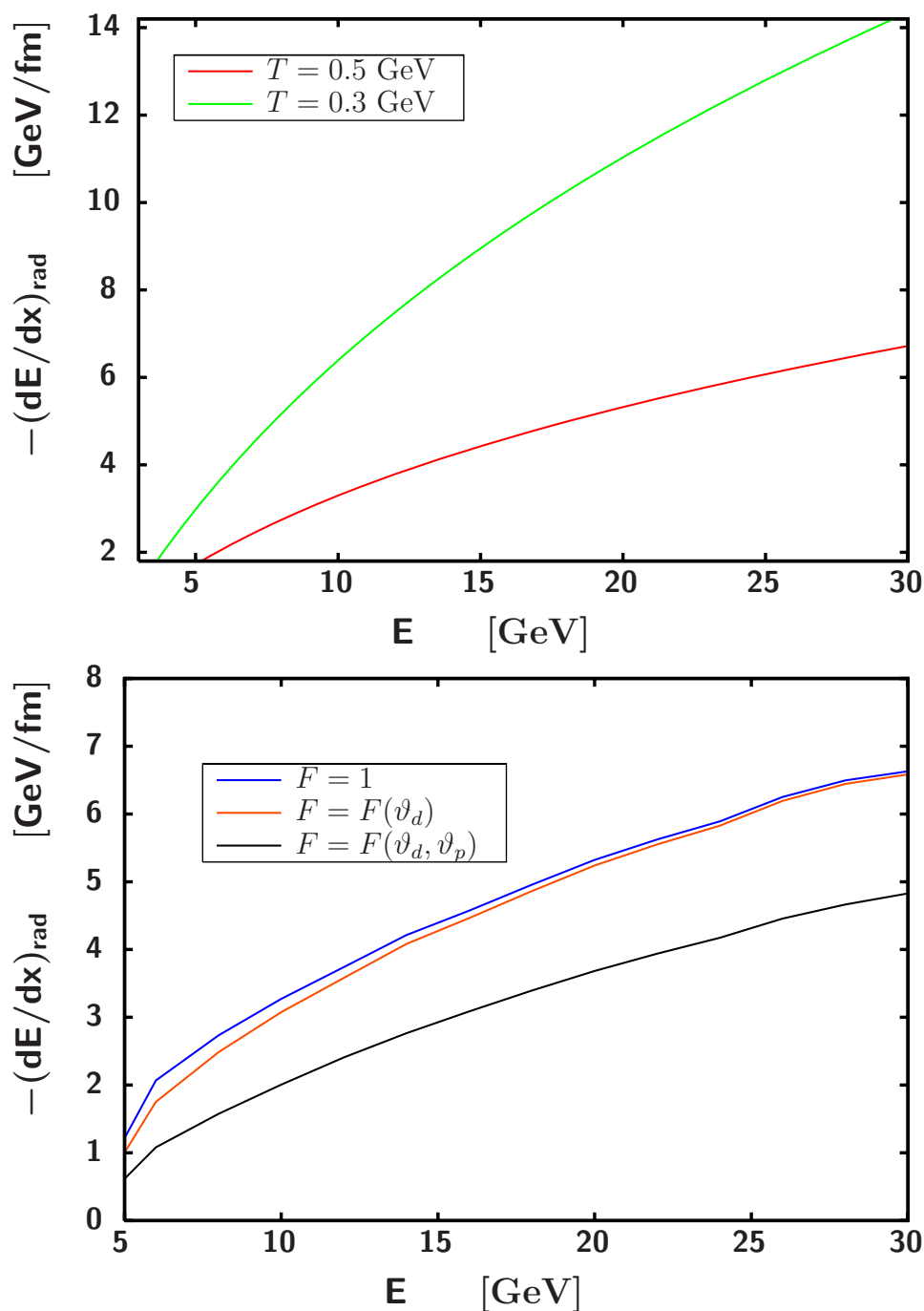


Figure 4.8: The radiative energy loss for charm quarks in potential model as a function of incidence energy. In the upper panel the energy loss is calculated analytically in the case of various temperatures $T = 0.5$ GeV (red line) and $T = 0.3$ GeV (green line) is plotted, while entering the medium temperature over the Debye mass $\mu_D(T)$. The smaller temperature yield a smaller phase space what lets decrease the energy loss. The lower panel shows the reduction of the radiative energy loss for $T = 0.3$ GeV without additional factor (blue line), with the proper dead cone factor (orange line) and with the modified dead cone factor (black line), i.e. taking into account the effective gluon mass ω_0 in addition. Here, we calculate with $\omega_0 \simeq \mu_D(0.3) = 0.58$ GeV.

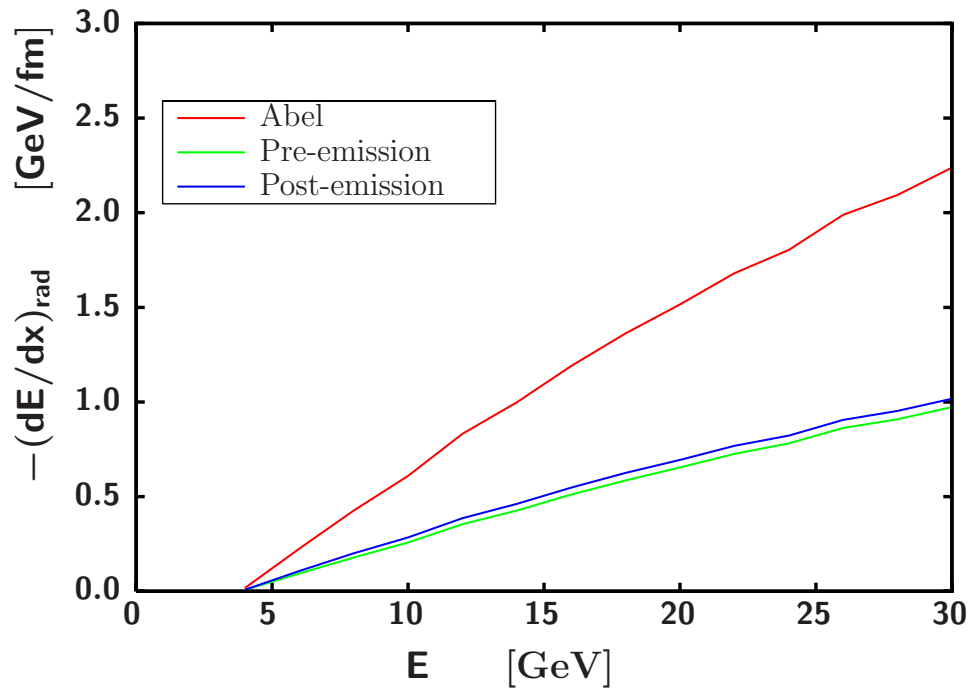


Figure 4.9: It is shown the radiative energy loss in the potential model as a function of the initial charm-quark energy E for different single contributions: pre-projectile gluon emission (green line), post-projectile gluon emission (blue line) and the coherent superposition of both diagrams which is summarised in the Abelian amplitude (red line). Impressively, one encounters a difference between the single contributions and the Abelian amplitude of a factor $C_A/C_F = 9/4$ in the case of dominating projectile contributions. We use the same set of parameters as in the lower panel of Fig. 4.8.

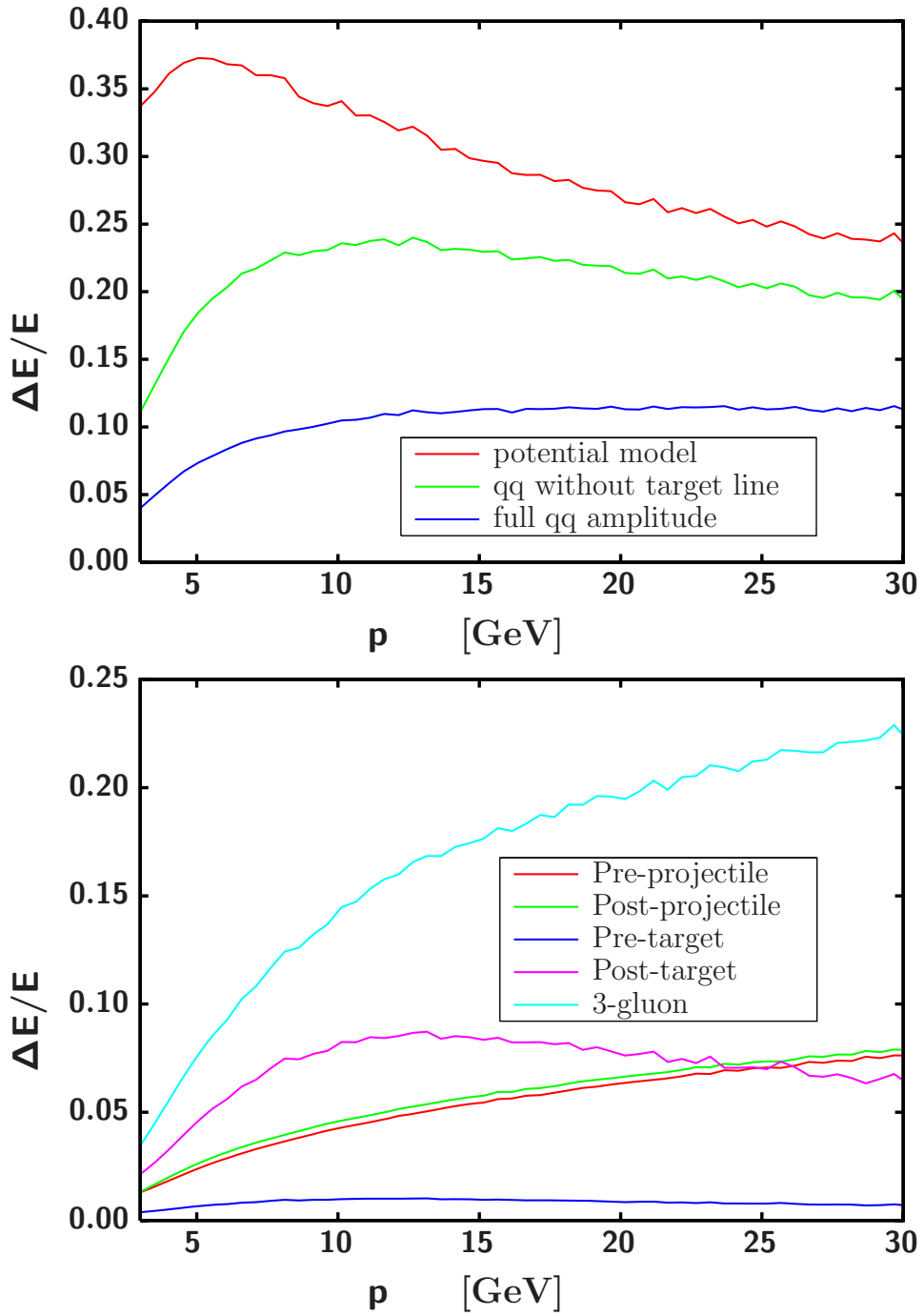


Figure 4.10: The fractional radiative energy loss of a projectile charm quark is shown as a function of various initial momenta p while scattering with a charm target quark. Upper panel: The potential model (red line) is hard to compare to the quark-quark scattering amplitude (blue line) and even not if we omit target contributions (green line). This is due to the small target mass and the non-vanishing post-target amplitude. Lower panel: The single contributions to the total radiation amplitude is exhibited. Note that the post-target diagram is important as well as the three-gluon vertex diagram and the projectile contributions, always with the phase-space restriction of $0 < \vartheta < \pi/2$. Besides this, the pre-target contribution can be neglected and confirms our prediction in this way.

the total amplitude, which consists of all single contributions, is suppressed compared to the amplitude without target gluon emission which is also observed in [Tho03] for $\vartheta \gtrsim 0.5$. This can be understood by a destructive interference between the target diagrams and the projectile- and three-gluon vertex diagrams. Actually, one expects a vanishing target quark line contribution, and so the total qq radiation amplitude should recover the potential model result in the limit of heavy and slow target quarks. The crucial point is now the range of integration over ϑ -phase space by using the analytical approximations from the previous section. There, we restrict the area to $0 < \vartheta < \pi/2$, meaning a cut-off in gluon backward emission. If we now assume $\vartheta \lesssim 0.5$, what peaked the gluon in forward direction, the target line contributions become irrelevant compared to projectile- and three-gluon vertex contributions and can actually be neglected. Indeed, the potential model well predicts the qq scattering scenario, as also mentioned in Fig. 4.11 for increasing target masses. This suppression of target gluon emission in A^+ -gauge can be understood while considering the GB approach for target contributions, as outlined in Section 3.5. The pre-target diagram has to be 0; this is easy to verify in the lower panel of Fig. 4.10. Post-target contributions are proportional to the dimensionless factor $1/x(\vartheta)$. This behaviour strictly differs from all other single contributions in qq scattering events! Hence, the smaller ϑ the bigger becomes x and so let decrease the post-target contribution.

Finally, we just stress the fact again that the target contributions must encounter to the total radiation amplitude and thus the total radiative energy loss of heavy quarks due to gauge invariance⁶. This makes it really hard to compare with other results which all based on computations within the potential model.

4.4 The Running Coupling Constant

The coupling strength of the strong interaction is known to vary considerably over the range of scales probed, e.g. in heavy-ion collisions. Thus, we study here some quantum field theoretical corrections to the tree level scattering processes by investigating the influence of a running coupling strength on radiative energy loss instead of using a constant value α_s .

In all previous calculations the strong coupling was put to $\alpha_s = 0.3$, in agreement to previous approaches to radiative energy loss, cf. [Käm00, Wie05, Gyu02, Tho03]. Now we take the self-energy contributions to tree-level processes as a divergent loop correction into account, that means the exchanged gluon is dressed by a self-energy Π^i , depending on transversal and longitudinal modes ($i = t, l$) which is expressed as a finite matter contribution f^i . This boson self-energy in a thermal medium has a generic structure, cf. [Pes06],

$$\Pi^i(p_0, |\vec{p}|) = 4\pi\beta_0 \left[(\epsilon^{-1} - \ln(-q^2/\mu_D^2)) p^2 + f^i(p_0, |\vec{p}|) \right] \quad (4.24)$$

with a Debye mass μ_D as effective infrared cut-off for the gluon radiation spectrum. The scale of the running coupling is set by the squared four-momentum transfer q^2 . Referring to previous relations and considering an absorbing of the self-energy in running coupling

⁶Of course, in other gauges, e.g. A^- -gauge the target contributions can not be neglected. This is also the reason why we chose A^+ -gauge for being able to compare qq scattering with the potential model.

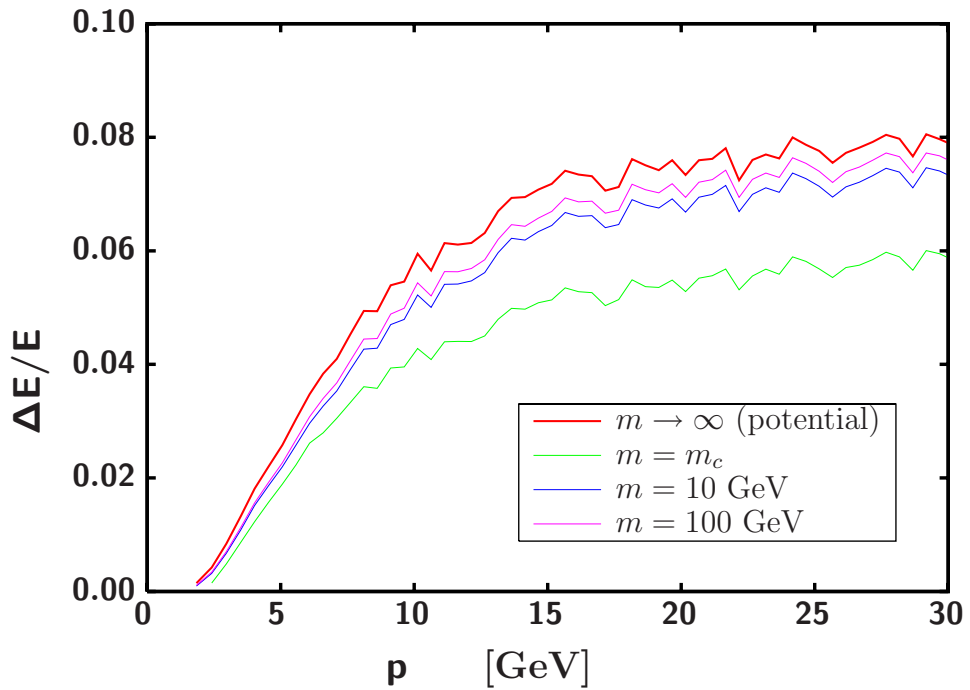


Figure 4.11: The relative energy loss of a projectile charm quark, scattering on various targets: potential (red line); charm quark $m = 1.5$ GeV (green line); hypothetical heavy quark $m_Q = 10$ GeV (blue line), and very massive quark $m_Q = 100$ GeV (magenta line) plotted for different projectile initial momenta p . One can verify a considerable approach to the case of infinite target mass (potential model) for increasing target masses. This limit is only valid for a restricted integration range of $0 < \vartheta < 0.5$ but nevertheless the same behaviour for a full-range ϑ .

in this way, the matter part of boson self-energy reads as

$$\Pi_{mat}^i = 4\pi\beta_0\alpha(q^2)f^i, \quad (4.25)$$

and we arrive at the coupling

$$\alpha_s(q^2) = \frac{1}{\beta_0 \ln(|q^2|/\Lambda)} \quad \text{with} \quad \beta_0 = \frac{11 - 2n_f/3}{4\pi}, \quad (4.26)$$

where β_0 is the leading coefficient of the beta-function corresponding to a one-loop correction. We choose the parameter $\Lambda \approx 205 \text{ MeV}^7$ for $n_f = 2$ as active number of quark flavours. The important coupling behaviour determines the dependence of the momentum scale q^2 . This strong logarithmic dependence of the four-momentum transfer q^2 is exhibited in Fig. 4.12. The usual value $\alpha_s = 0.3$ can be translated into a value for q^2 of about 1.7 GeV^2 , which confirms the choice of various free parameters in our numerical calculation; or from the opposite point of view, with the chosen average momentum transfer one directly obtains $\alpha_s \approx 0.3$.

This running coupling is implemented in numerical calculations for radiative energy loss spectra, shown in Fig. 4.13 for different projectile quark masses with a constant target charm-quark mass parameter. One can recognise in this figure only a small dependence of relative energy loss when using the running α_s compared to the constant value of 0.3. For small projectile quark energies, the transfer momentum $q^2 = q_0^2 - q_\perp^2 - q_z^2 \approx q_z^2$ increases due to the dominant relation of the z-component,

$$q_z \propto -\frac{m^2}{E^2}, \quad (4.27)$$

omitting anyway small q_0 and q_\perp contributions of the momentum transfer. Hence, a greater q_z is directly correlated to smaller values of α_s due to Eq. (4.26) and lets decrease the coupling strength.

In Fig. 4.13 is also shown an intersection where the corresponding squared momentum transfer belongs to the constant value $\alpha_s = 0.3$. With increasing projectile quark masses, this point moves to higher energies, in agreement with Eq. (4.27) on a qualitative level.

In contrast to this, it is possible that for a larger range of squared momentum transfer or complicated structures in α_s (e.g. considerable two- or three loop corrections) the running coupling effect may become more relevant at least for the radiative part of energy loss. Further recent discussions of the importance of the running coupling constant are given in [Pes06, Pro06].

4.5 Radiative vs. Collisional Energy Loss

In this last section we give a very short explanation of the idea of collisional energy loss in order to compare this results with our radiative energy loss for heavy quarks. This is simply motivated by the previous investigations [Mus05, Ala06, Adi06] which suggest that collisional rather than the radiative processes are the dominant mechanisms

⁷It appears in the QCD running coupling via dimensional transmutation as a scale parameter varying with the quark flavour number n_f .

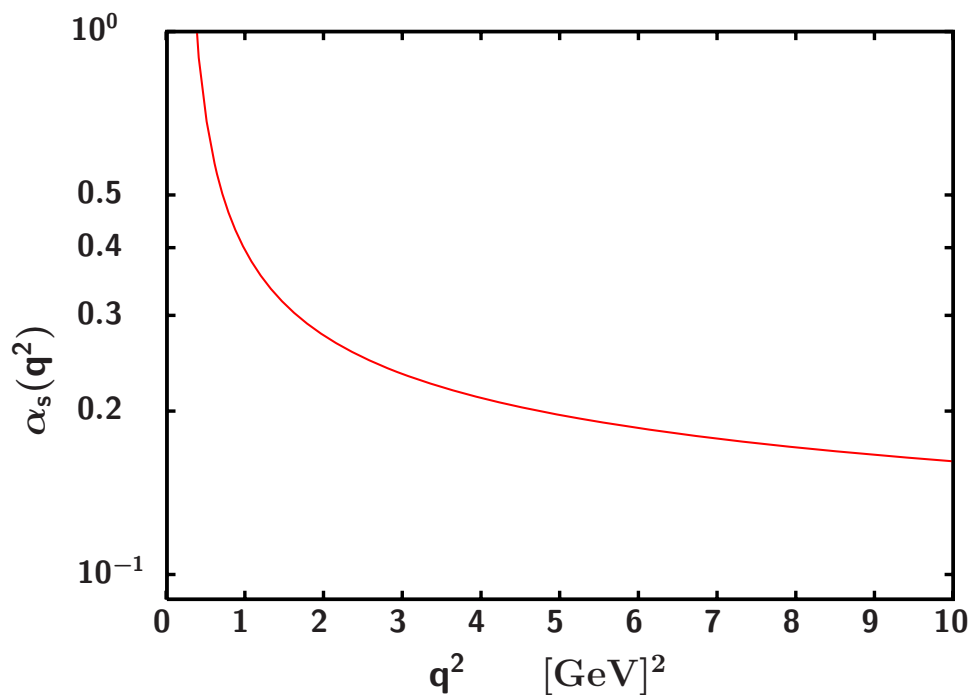


Figure 4.12: Running coupling constant in QCD according to Eq. (4.26) with $\Lambda = 205$ MeV and $n_f = 2$.

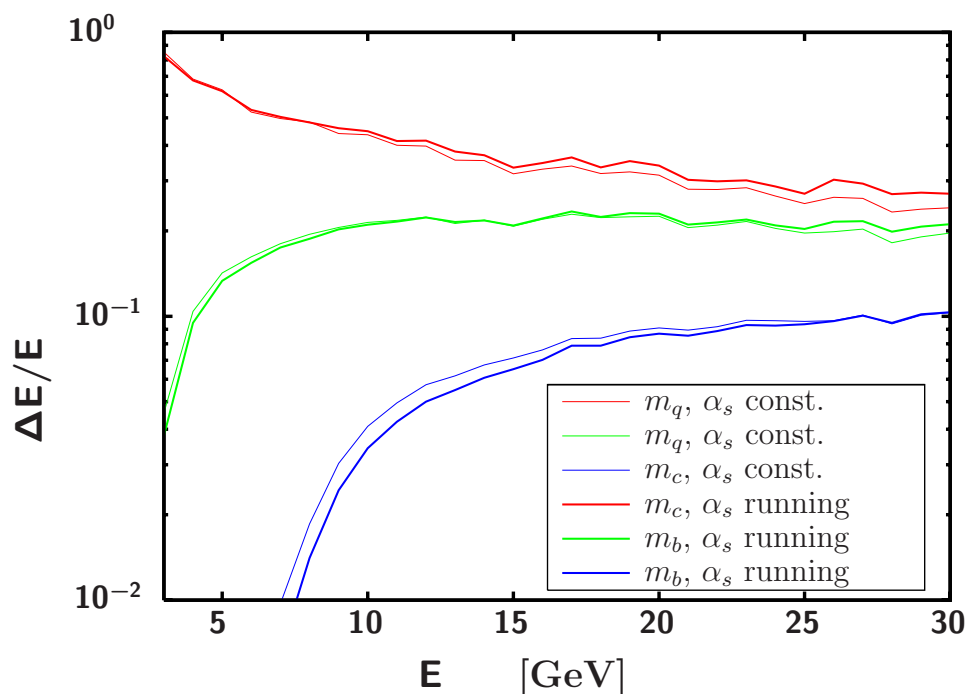


Figure 4.13: The fractional energy loss for light (red), charm (green) and bottom (blue) projectile quarks as a function of their initial energies E , scattering with a charm target quark at rest. The thin lines stand for the constant value $\alpha_s = 0.3$ while the fat lines represent the calculations with running coupling.

for the partonic energy loss in the measured p_T domain of RHIC, i.e. comparatively small transverse momenta.

The key of calculating the energy loss of an elastic scattering event is perceived on tree level but its relevant part is derived from the internal, so-called Hard-Thermal-Loop (HTL) gluon propagator and takes the production of an 'off-shell' jet into account. Considering this higher order process, Djordjevic *et al.* give a numerical approximation in [Djo06b] for the collisional energy loss in finite size QCD media, shown in Fig. 4.15 for light and heavy quarks as a function of their momenta. Additionally, they use approximations for the net radiative energy loss and compare it directly with numerical results of collisional energy loss by means of a separation between those two contributions. For small momenta (i.e. $p < 10$ GeV) the energy loss from the elastic scattering overestimates the radiative part. Thus, collisional energy loss should play an important role in the low momentum range at RHIC. In summary, one can interpret collisional energy loss and radiative energy loss as two competing effects of gain respectively induced suppression in the limit of small projectile quark momenta.

The numerical results of our program are shown in Fig. 4.14 for heavy projectile quarks. Results from [Djo06b] for radiative energy loss, as exhibited in Fig. 4.15, are confirmed in the limit of assuming only a single scattering. This could be possibly an evidence for not accounting for the crucial multiple scattering processes in comparison to the single events.

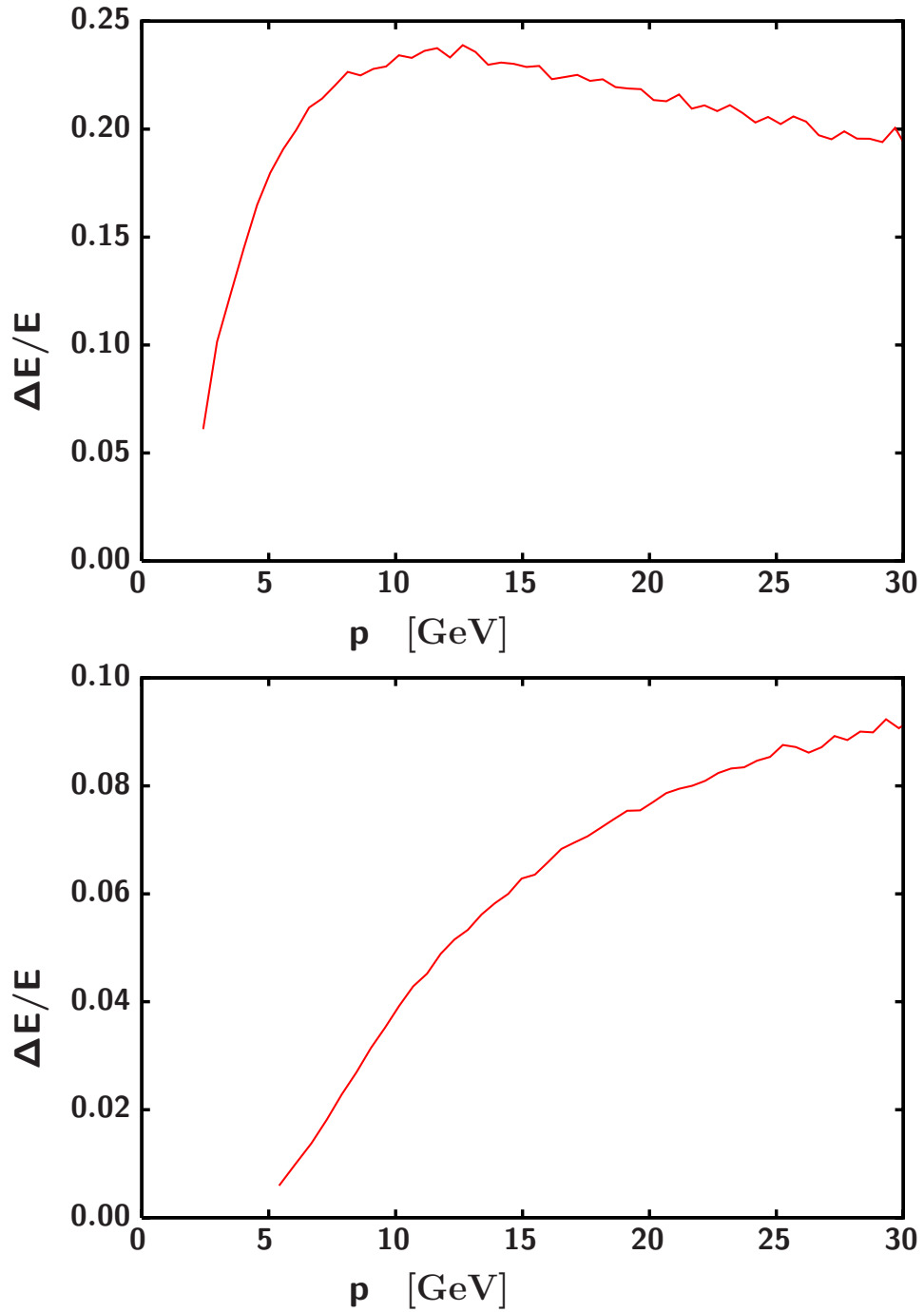


Figure 4.14: The relative radiative energy loss as a function of the momentum for charm (upper panel) and bottom (lower panel) projectile quarks which scatter with a slow and light target. It is comparable with results for the net fractional radiative energy loss of Fig. 4.15 in principle. Because of this, we use the parameter $\langle \vec{q}_\perp \rangle = 0.76$ GeV and $\omega_0 = 0.2$ GeV.

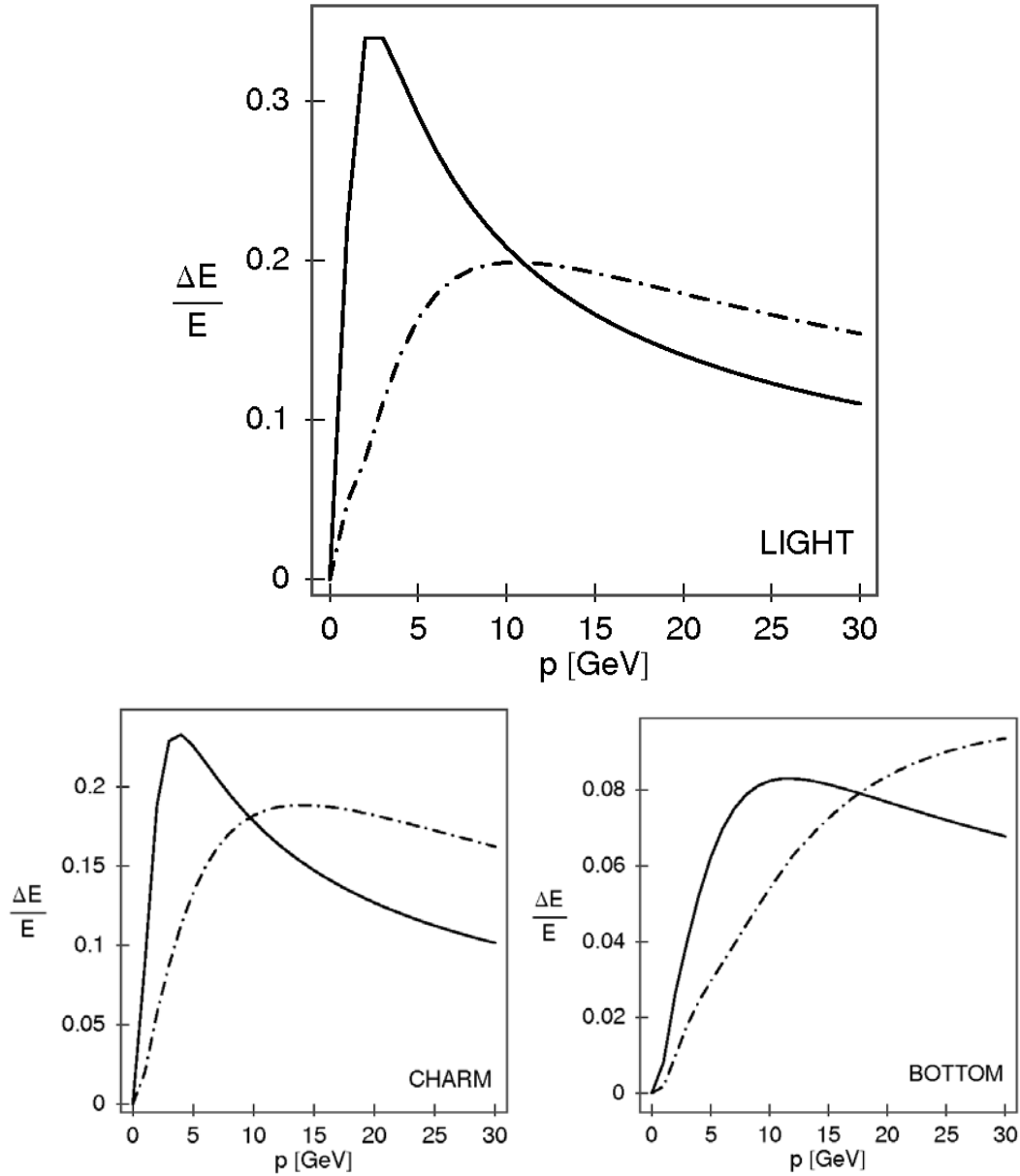


Figure 4.15: The net fractional radiative (dot-dashed line) and collisional (solid line) energy loss as a function of momentum for light quarks (upper panel), charm quarks (left lower panel) and bottom quarks (right lower panel) with an assumed medium thickness of $L = 5$ fm and $\lambda = 1.2$ fm. In the lower momentum range, the collisional energy dominates the radiative one. The figures are taken from [Djo06b, Wic06].

5 Summary and Outlook

The present thesis deals with radiative energy loss of heavy quarks traversing a hot deconfined medium. The actual relevance of this topic is provided by recent precision measurements at RHIC. While the theoretical interpretation of jet quenching, manifest itself as steepening of transverse momentum spectra of hadrons or as $R_{AA} < 1$, seems to be on a satisfying level for light-quark hadrons, the final understanding for heavy-quark mesons is not yet accomplished. It seems that besides the radiative energy loss, the collisional energy loss gives a significant contribution for the full energy loss. Nevertheless, the treatment of purely radiative energy loss of heavy quarks (charm in particular) still needs improvements.

It is the aim of the work to separate the gluon emission process of a charm quark with finite momentum and to consider this process in an isolated manner. In doing so, various further simplifications are introduced. Among them is the assumption of on-shell quarks and the restriction to one-gluon emission. The emission process is analysed in tree-level approximation. Potentially important unitary conditions, first considered in [Gyu01] in this context, are not yet accounted for. The given idealisations, however, allow a comparatively transparent treatment of the one-gluon bremsstrahlung process. Particular emphasis is put on (i) a correct kinematical treatment of the kinematics (most approaches employ the asymptotic high-energy limit for jet partons and soft-gluon limit for the emitted radiation), (ii) the use of the exact matrix elements (many approaches employ a factorisation into an elastic part and a radiation part owing to the soft-gluon approximation), (iii) comparing with the dynamical quark-quark scattering. The ultimate goal is to obtain an estimate for the phase space integrated, averaged relative energy loss. Since truncated tree-level radiation amplitudes suffer from collinear divergences, a modified gluon dispersion relation is introduced, where the effective in-medium gluon mass serves as screening parameter, in addition to a finite quark mass.

As 'working horse' we employ here a numerical code, developed by R. Thomas, which accounts for the above items (i)...(iii). The results are compared with several approximations employed in previous approaches in literature. The code calculates numerically exactly the for various radiation processes and performs the squaring of the summed amplitudes for scalar QCD. Spin effects have been previously shown to be small.

Our findings can be summarised as follows. We have extended analytical expressions for single quark scattering in medium with one-gluon emission, i.e. consider a non-zero effective gluon mass ω_0 , accounting for the in-medium dispersion relation, and finite quark masses. The interplay of both screening effects was discussed in detail, particularly the importance of ω_0 when we consider backward gluon emission, $\vartheta \rightarrow \pi$. Additionally, we have found corrections to the often used dead cone factor and treated the factorisation of the elastic amplitude in the right way by means of kinematic corrections to the proper

total radiation amplitude.

Moreover, we showed the dominance of the non-Abelian three-gluon vertex diagram over the Abelian contributions which is only due to the integration of the gluon distribution over wide phase space areas. We compared this divergent behaviour of the relevant analytically found three-gluon matrix element to the complex structure of the numerical calculated matrix element with success.

The radiative energy loss was derived with efficient phase space restrictions for the gluon momenta thresholds in the integration procedure as well as using an averaged value for the transverse momentum transfer. In this connection, we have emphasised that one is free in the choice of the single components of \vec{p}_\perp that is to say one degree of freedom can be omitted; this simplifies further relations.

We have compared the total radiation energy loss in the potential model to the case of quark-quark scattering and found crucial differences between both models in the limits of slow and heavy target quarks! This suffers from a strong restriction of the gluon emission angle ϑ - only in the case of strongly forward-peaked gluon radiation the target contributions can be neglected in A^+ -gauge and so confirms the potential model. In this context, further investigations should consider the colour structure of the radiation amplitudes in particular, i.e. one has to compare the energy loss in QED and QCD according to the validity of the potential model.

Furthermore, we have considered the importance of a running coupling strength and found no significant deviations from constant coupling here in the used range of q^2 .

Finally, we compared our numerical computations for the process of radiative energy loss to other results and found in the limit of neglecting target gluon radiation coincidental results for heavy projectile quarks.

For a realistic treatment of the energy loss of heavy quarks in a hot, deconfined medium, successively the following extensions are needed, at least. Referring to experiments at RHIC, one has to ask about double- or multiple scattering scenarios which yield to a description of dynamical thick media. Of course, one has to implement the interference with the production amplitude of the quark, meaning the quark is not 'on-shell' any more. Tree-level processes, which we take into account in the present thesis, do not consider dynamical effects of QCD, e.g. loop diagrams. The consideration of the whole possible range of the transverse momentum transfer might be a further step to a more realistic treatment of heavy quark energy loss. That means, besides the additional integration over q_\perp -phase space, the relevance in running coupling could raise.

All this previous aspects of investigations indicate the importance of further research in energy loss of heavy quarks; hopefully one day close the gap between experimental data and theoretical predictions.

Appendix A Notation and Conventions

Here, we present some declarations and conventions which are used throughout the whole thesis, as used for instand in [Gyu94], following the standard textbook from Itzykson and Zuber [Itz80].

All calculations have done in natural units $c = \hbar = 1$. For the description of an arbitrary point in space-time we use following contravariant four-vector convention:

$$x^\mu \equiv (x^0, x^1, x^2, x^3) = (t, \mathbf{x}) = (t, x, y, z). \quad (\text{A.1})$$

The covariant vector x_μ can be expressed by the contravariant vector x^μ and the fundamental metric tensor $g_{\mu\nu}$

$$x_\mu \equiv (x_0, x_1, x_2, x_3) \equiv g_{\mu\nu}x^\nu = (t, -x, -y, -z), \quad (\text{A.2})$$

where the metric tensor is given by

$$g_{\mu\nu} = \begin{pmatrix} 1 & 0 & 0 & 0 \\ 0 & -1 & 0 & 0 \\ 0 & 0 & -1 & 0 \\ 0 & 0 & 0 & -1 \end{pmatrix} \quad (\text{A.3})$$

with a negative signature. Of course, for considering dynamical space-times a variable metric tensor is also possible, but in this work we need to use a non-curved space-time (Minkowski space-time). All expressions have to be summed up over indices appearing twice (contravariant and covariant), in conformity with the Einstein sum convention. Lorentz indices are denoted by Greek letters (μ, ν, σ, \dots). In contrast to this we use small Latin letters (a, b, c, \dots) describing colour indices and capital Latin letters (A, B, C, \dots) to label the different colour states.

The considered scattering processes are based on tree-level diagrams. Correspondingly, we neglect all higher order diagrams. That means, the coupling $\alpha_s = g^2/4\pi$, considered only in first order, does not run. All calculations are done with a constant value of $\alpha_s = 0.3$ except of accounting the running coupling constant α_s in Section 4.5.

To investigate schematically different kinematic situations of scattering, we employ three quark mass parameters. As used in common the mass of the light down quark is set $m_d = 0.007 \text{ GeV}/c^2$, $m_c = 1.5 \text{ GeV}/c^2$ for charm quark mass, and the heavy bottom quark with $m_b = 4.5 \text{ GeV}/c^2$. In general, we denote light quarks (up, down) with m_q and heavy quarks (charm, strange, bottom) with m_Q .

Furthermore, we often use an abbreviation for $|\vec{k}_\perp|$ and $|\vec{q}_\perp|$, which has to be understand as shorthand expressions k_\perp and q_\perp .

Additionally, we use a system to indices the matrix elements $M_{n,m,l}$ in a clear way. This notation was firstly introduced by Gyulassy, Levai and Vitev [Gyu00b]. The label n stands for the number of scatterings. In this thesis, we concentrate on single scattering, $n = 1$, m denotes that the gluon is emitted after the m -th scattering with the restriction $0 \leq m \leq n$. l labels the final state interaction pattern after the gluon is emitted, e.g. $l = 1$ in the case of a triple gluon vertex. This procedure represents an efficient index-type, especially referring to the extension of double scattering scenarios.

Appendix B Light-cone Variables, Dirac Matrices and Spinors

B.1 Light-cone Variables

According to use of special gauges of the gluon field (see Appendix F) it is suitable to work in light-cone coordinates¹, defined for an arbitrary covariant four-vector as follows

$$x_\mu = (x_0, x_x, x_y, x_z) \equiv (x_0, \vec{x}_\perp, x_z) = [x^+, x^-, \vec{x}_\perp]. \quad (\text{B.1})$$

A customary notation for x^+ and x^- is used

$$x^+ = x_0 + x_z \quad \text{and} \quad x^- = x_0 - x_z, \quad (\text{B.2})$$

where the incident beam of the projectile is designated to the z -direction. With this definition and a modified metric tensor $g_{\mu\nu}$ the scalar product expressed in light-cone coordinates reads

$$a_\mu b^\mu = \frac{1}{2}(a^+ b^- + a^- b^+) - \vec{a}_\perp \vec{b}_\perp. \quad (\text{B.3})$$

The light-cone variables are applied especially in Chapter 3 for finding exact kinematics.

B.2 Dirac Matrices and Spinors

The numerical calculation of matrix elements with the implementation of particle spins uses γ matrices as fundamental algebraic objects. The Dirac matrices satisfy the relations

$$\{\gamma^\mu, \gamma^\nu\} = 2g^{\mu\nu} \quad , \quad (\gamma^\mu)^\dagger = \gamma^0 \gamma^\mu \gamma^0 \quad (\text{B.4})$$

with the Minkowski metric $g^{\mu\nu} = \text{diag}(1, -1, -1, -1)$ as defined in Appendix A. The four-dimensional γ matrices in Dirac representation are defined as follows:

$$\gamma^0 = \begin{pmatrix} \mathcal{I} & \mathcal{O} \\ \mathcal{O} & -\mathcal{I} \end{pmatrix}, \quad \gamma^k = \begin{pmatrix} \mathcal{O} & \sigma^j \\ -\sigma^j & \mathcal{O} \end{pmatrix}, \quad \gamma^5 = \begin{pmatrix} \mathcal{O} & \mathcal{I} \\ \mathcal{I} & \mathcal{O} \end{pmatrix}, \quad (\text{B.5})$$

¹In order to distinguish a light-cone vector between a four-vector we confine the light-cone components in edged brackets.

where the γ matrices obey the properties

$$(\gamma^0)^\dagger = \gamma^0, \quad (\gamma^j)^\dagger = -\gamma^j, \quad (\gamma^0)^2 = 1, \quad (\gamma^j)^2 = -1 \quad (\text{B.6})$$

and σ^j labels two-dimensional Pauli matrices,

$$\sigma^1 = \begin{pmatrix} 0 & 1 \\ 1 & 0 \end{pmatrix}, \quad \sigma^2 = \begin{pmatrix} 0 & -i \\ i & 0 \end{pmatrix} \quad \text{and} \quad \sigma^3 = \begin{pmatrix} 1 & 0 \\ 0 & -1 \end{pmatrix}. \quad (\text{B.7})$$

Additionally, unity- and zero matrices are given by

$$\mathcal{I} = \begin{pmatrix} 1 & 0 \\ 0 & 1 \end{pmatrix} \quad \text{and} \quad \mathcal{O} = \begin{pmatrix} 0 & 0 \\ 0 & 0 \end{pmatrix}. \quad (\text{B.8})$$

With the aim of describing the dynamical behaviour of partons we define Dirac bispinors and their adjuncture spinors as solutions of the Dirac equation

$$\bar{u}_s^{(\alpha)}(p)(i\gamma^\mu \overleftarrow{\partial}_\mu + m) = 0 \quad \text{and} \quad (\text{B.9})$$

$$(i\gamma^\mu \partial_\mu - m)u_s^{(\alpha)}(p) = 0 \quad \text{with} \quad s = 1, 2, \quad \alpha = 1, 2, \quad (\text{B.10})$$

where s denotes positive and negative spin projections along a chosen quantisation axis, and α labels the polarisation. Moreover, the arrow represents the direction of applying the differential operator. To solve equation (B.10) and to take the used relations into account, we get the spinors² normalised to $2m$ as

$$u_+^{(1)}(\vec{p}) = \sqrt{E(\vec{p}) + m} \begin{pmatrix} \begin{pmatrix} 1 \\ 0 \end{pmatrix} \\ \frac{\vec{\sigma}\vec{p}}{E(\vec{p}) + m} \begin{pmatrix} 1 \\ 0 \end{pmatrix} \end{pmatrix}, \quad (\text{B.11})$$

$$u_-^{(1)}(\vec{p}) = \sqrt{E(\vec{p}) + m} \begin{pmatrix} \begin{pmatrix} 0 \\ 1 \end{pmatrix} \\ \frac{\vec{\sigma}\vec{p}}{E(\vec{p}) + m} \begin{pmatrix} 0 \\ 1 \end{pmatrix} \end{pmatrix}$$

for positive energies. Similarly, the solution of free Dirac equation for negative energies are

$$v_+^{(1)}(\vec{p}) = \sqrt{E(\vec{p}) + m} \begin{pmatrix} \frac{\vec{\sigma}\vec{p}}{E(\vec{p}) + m} \begin{pmatrix} 1 \\ 0 \end{pmatrix} \\ \begin{pmatrix} 1 \\ 0 \end{pmatrix} \end{pmatrix}, \quad (\text{B.12})$$

$$v_-^{(1)}(\vec{p}) = \sqrt{E(\vec{p}) + m} \begin{pmatrix} \frac{\vec{\sigma}\vec{p}}{E(\vec{p}) + m} \begin{pmatrix} 0 \\ 1 \end{pmatrix} \\ \begin{pmatrix} 0 \\ 1 \end{pmatrix} \end{pmatrix}.$$

²Only the spinor u is used in the numerical calculations.

Appendix C Colour Algebra in QCD

The QCD is a non-Abelian gauge theory with underlying colour $SU(3)$ algebra. In general, the group $SU(N)$ as a object of special, unitary $(N \times N)$ -matrices satisfies the Lie algebra

$$[T^a, T^b] = if_{abc}T^c, \quad (\text{C.1})$$

where T^a ($a, b, c = 1 \dots N^2 - 1$) are the generators of the group. The structure constant, given by f_{abc} , is totally anti-symmetric in all indices. In the case of $N = 2$ it reduces to the epsilon symbol, ϵ_{ijk} , with $\epsilon_{123} = 1$ (even permutation). The generators are related to their matrix representation as

$$T^a = \frac{\lambda^a}{2}. \quad (\text{C.2})$$

For $SU(3)$ one can choose eight representations to be the (3×3) matrices of Gell-Mann, given by

$$\begin{aligned} \lambda_1 &= \begin{pmatrix} 0 & 1 & 0 \\ 1 & 0 & 0 \\ 0 & 0 & 0 \end{pmatrix}, & \lambda_2 &= \begin{pmatrix} 0 & -i & 0 \\ i & 0 & 0 \\ 0 & 0 & 0 \end{pmatrix}, & \lambda_3 &= \begin{pmatrix} 1 & 0 & 0 \\ 0 & -1 & 0 \\ 0 & 0 & 0 \end{pmatrix}, \\ \lambda_4 &= \begin{pmatrix} 0 & 0 & 1 \\ 0 & 0 & 0 \\ 1 & 0 & 0 \end{pmatrix}, & \lambda_5 &= \begin{pmatrix} 0 & 0 & -i \\ 0 & 0 & 0 \\ i & 0 & 0 \end{pmatrix}, & \lambda_6 &= \begin{pmatrix} 0 & 0 & 0 \\ 0 & 0 & 1 \\ 0 & 1 & 0 \end{pmatrix}, \\ \lambda_7 &= \begin{pmatrix} 0 & 0 & 0 \\ 0 & 0 & -i \\ 0 & i & 0 \end{pmatrix} & \text{and} & \lambda_8 &= \frac{1}{\sqrt{3}} \begin{pmatrix} 1 & 0 & 0 \\ 0 & 1 & 0 \\ 0 & 0 & -2 \end{pmatrix}. \end{aligned} \quad (\text{C.3})$$

These matrices are normalised according to

$$tr(\lambda^a \lambda^b) = 2\delta^{ab}. \quad (\text{C.4})$$

Additionally, the generators fulfil further important relations. They are traceless

$$tr(T^a) = 0 \quad (\text{C.5})$$

and hermitian¹

$$T^{a\dagger} = T^a. \quad (\text{C.6})$$

¹In $SU(3)$, both properties reduces the number from 18 needed quantities to specify (3×3) complex matrices to a set of 8 real quantities.

For general N another useful relation of T^a is as follows:

$$T_{ij}^a T_{kl}^a = \frac{1}{2}(\delta_{il}\delta_{jk} - \frac{1}{N}\delta_{ij}\delta_{kl}), \quad (\text{C.7})$$

what leads us to

$$(\overline{T^a T^a})_{il} = C_F \delta_{il}, \quad C_F = \frac{N^2 - 1}{2N}. \quad (\text{C.8})$$

Here, the C_F denotes the eigenvalues of Casimir operator. Every quadratic operator $(T^b)^2$ commuting with an arbitrary generator T^a of the group $SU(N)$ is called quadratic Casimir operator. The adjoint representation satisfies the relation

$$\sum_{c,d=1}^{N^2-1} f_{acd} f_{bcd} = \delta_{ab} C_A, \quad C_A = N. \quad (\text{C.9})$$

For $SU(3)$ we obtain for the eigenvalues

$$C_F = \frac{4}{3}, \quad C_A = 3. \quad (\text{C.10})$$

In order to evaluate matrix elements, as done in Section 3.3, we focus on an explicit calculation of colour quantities. Therefore, we take over the short hand notation from [Gyu94] to express the product of colour matrices, structure constants and colour states

$$(C_{b_1 \dots b_n}^{a_1 \dots a_m})_{AB} \equiv \chi_B^\dagger C_{b_1 \dots b_n}^{a_1 \dots a_m} \chi_A \quad \text{with} \quad A, B, C = 1 \dots N, \quad (\text{C.11})$$

where m and n are arbitrary colour indices, and N is the number of colour states. For $SU(3)$ the colour states χ_J can be written as three-dimensional unit vectors

$$\chi_1 = \begin{pmatrix} 1 \\ 0 \\ 0 \end{pmatrix}, \chi_2 = \begin{pmatrix} 0 \\ 1 \\ 0 \end{pmatrix} \quad \text{and} \quad \chi_3 = \begin{pmatrix} 0 \\ 0 \\ 1 \end{pmatrix}. \quad (\text{C.12})$$

They obey the very useful equations

$$\sum_{A=1}^N \chi_A \chi_A^\dagger = \mathcal{E} \quad \text{and} \quad \sum_{A=1}^N \chi_A^\dagger \mathcal{M} \chi_A = \text{tr}(\mathcal{M}) \quad (\text{C.13})$$

with \mathcal{E} as the identity matrix and \mathcal{M} as an arbitrary complex matrix, all in $(N \times N)$ format. Using the abbreviation (C.11), the summed and averaged colour squared matrix elements read in general

$$\overline{|C_{A_1 \dots A_s, A'_1 \dots A'_t}^{g_1 \dots g_k, g'_1 \dots g'_l}|^2} = \frac{1}{(N^2 - 1)^k \cdot N^s} \sum_{\substack{A_1 \dots A_s = 1 \dots N \\ A'_1 \dots A'_t = 1 \dots N \\ g_1 \dots g_k = N^2 - 1 \\ g'_1 \dots g'_l = N^2 - 1}} \left[C_{A_1 \dots A_s, A'_1 \dots A'_t}^{g_1 \dots g_k, g'_1 \dots g'_l} \cdot \left(C_{A_1 \dots A_s, A'_1 \dots A'_t}^{g_1 \dots g_k, g'_1 \dots g'_l} \right)^\dagger \right]. \quad (\text{C.14})$$

We use here k as the number of initial gluons and l as the number of final gluons. The number of initial quarks is denoted with s , final quarks are expressed with t . The overline at the colour structure means an average over all initial colour states and a sum over all final colours. At first we calculate the elastic colour part $C_{1,el}$ with the help of relations above,

$$C_{1,el} \equiv \overline{|T_{AB}^f T_{CD}^f|^2} = \frac{1}{N^2} \sum_{A,B,C,D=1}^N (\chi_B^\dagger T^f \chi_A \chi_D^\dagger T^f \chi_C) \cdot (\chi_B^\dagger T^g \chi_A \chi_D^\dagger T^g \chi_C)^\dagger.$$

This can be simplified by using Eqs. (C.4), (C.6) and (C.8) to

$$\begin{aligned} C_{1,el} &= \frac{1}{N^2} (\chi_B^\dagger T^f \chi_A \chi_D^\dagger T^f \chi_C) \cdot (\chi_B^\dagger T^g \chi_A \chi_D^\dagger T^g \chi_C)^\dagger \\ &= \frac{1}{N^2} \chi_B^\dagger T^f \chi_A \chi_D^\dagger T^f \chi_C \chi_C^\dagger T^g \chi_D \chi_A^\dagger T^g \chi_B \\ &= \frac{1}{N^2} \text{tr}(T^f T^g) \text{tr}(T^f T^g) \\ &= \frac{1}{2N^2} \delta^{fg} \text{tr}(T^f T^g) \\ &= \frac{C_F}{2N}. \end{aligned} \tag{C.15}$$

In the case of $N = 3$ we obtain $C_{1,el} = \frac{2}{9}$. Subsequently, the sum signs for colour indices and the indices for colour states are neglected. Thus, colour expressions from Eqs. (3.32) and (3.33) are evaluated for $SU(3)$ as

$$\begin{aligned} \overline{|(T^f T^g)_{AB} T_{CD}^f|^2} &= \overline{|(T^g T^f)_{AB} T_{CD}^f|^2} \\ &= \frac{1}{N^2} \chi_B^\dagger T^f T^g \chi_A \chi_D^\dagger T^f \chi_C \chi_C^\dagger T^g \chi_D \chi_A^\dagger T^g T^e \chi_B \\ &= C_F \cdot \frac{1}{N^2} \text{tr}(T^f T^e) \text{tr}(T^f T^e) \\ &= C_F \cdot C_{1,el} = \frac{8}{27}. \end{aligned} \tag{C.16}$$

The colour commutation structure of Eq. (3.34) can be derived in the same way as

$$\begin{aligned} \overline{|[T^f, T^g]_{AB} T_{CD}^f|^2} &= \overline{|if_{fge} T_{AB}^e T_{CD}^f|^2} \\ &= \frac{1}{N^2} f_{fge} f b g a \chi_B^\dagger T^e \chi_A \chi_D^\dagger T^f \chi_C \chi_C^\dagger T^b \chi_D \chi_A^\dagger T^a \chi_B \\ &= \frac{1}{N^2} f_{fge} f b g a \frac{1}{2} \delta_{ea} \text{tr}(T^f T^b) \\ &= C_A \cdot \frac{1}{2N^2} \delta_{fb} \text{tr}(T^f T^b) = C_A \cdot C_{1,el} = \frac{2}{3}. \end{aligned} \tag{C.17}$$

Appendix D Feynman Rules

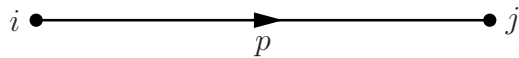
In this appendix the used propagators and vertices for the employed Feynman rules are given. Following the scheme below, colour factors appear in curly brackets, as also discussed in Appendix A. For omitting self coupling of gauge bosons, like photons do, all colour generators are set to unity. Additionally, due to the $U(1)$ symmetry of the QED structure constants f_{abc} equals to zero.

In the case of spinor QCD calculations one has to make allowance for different additional factors of bosonic or fermionic particles. Outgoing photons or gluon lines are assigned with their polarisation vector e^μ , whereas incoming fermionic spinor lines obtain a Dirac bispinor $u(p, s)$ multiplied with a colour state χ_A . In contrast to this, outgoing fermions get a factor $\chi_A^\dagger \cdot \bar{u}(p, s)$. For scalar particles¹ only the colour parts χ_A and χ_A^\dagger take into account.

The colour algebra is explained in Appendix C in detail, whereby comments to Dirac's bispinors can be found in Appendix B.

PROPAGATORS :

- quark scalar propagator $\frac{i}{p^2 - m_0^2 + i\epsilon} \cdot \{\delta_{ij}\}$

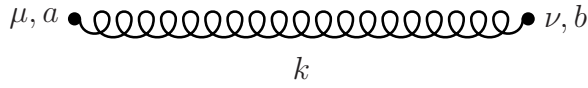


- quark spinor propagator $\frac{i}{p^\mu \gamma_\mu - m_0 + i\epsilon} \cdot \{\delta_{ij}\}$

¹In general, one has to distinct between particles or antiparticles by interchanging the spinors u and v .

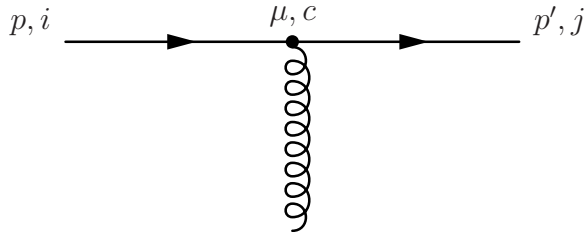
- gluon propagator $\frac{-i}{k^2 - \omega_0^2 + i\epsilon} \left(g^{\mu\nu} - (1 - \lambda) \cdot \frac{k^\mu k^\nu}{k^2 - \lambda\omega_0^2 + i\epsilon} \right) \cdot \{\delta_{ij}\}$

$\lambda \rightarrow 1$: Feynman gauge, $\lambda \rightarrow 0$: Landau gauge.



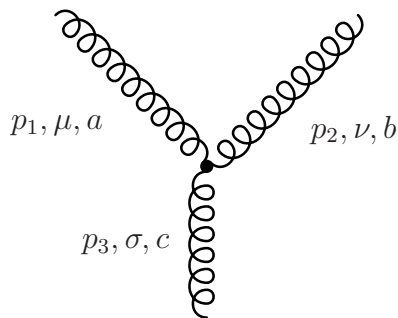
VERTICES²:

- scalar vertex $-ig(p + p')_\mu \cdot \{T_{ji}^c\}$



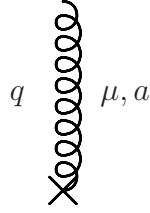
- spinor vertex $-ig\gamma_\mu \cdot \{T_{ji}^c\}$

- three-gluon vertex $ig[(p_1 - p_2)_\sigma \cdot g_{\mu\nu} + (p_2 - p_3)_\mu \cdot g_{\nu\sigma} + (p_3 - p_1)_\nu \cdot g_{\sigma\mu}] \cdot \{if_{abc}\}$



²To ensure four-momentum conservation it is essential to multiply the vertices with corresponding delta functions. For the sake of clearness it is neglected here.

- static Debye screened potential $-ig \cdot g^{0\nu} \frac{e^{-i\vec{q}\cdot\vec{x}}}{\vec{q}^2 + \tilde{\mu}^2} \cdot \{T_{CD}^a\}$



Vertices describing the Debye screened potential are introduced in Section 2.4; they are labelled by a cross in the Feynman diagram. The denominator combines two screening parameters:

$$\tilde{\mu}^2 = \mu_D^2 + \omega_0^2, \quad (\text{D.1})$$

where μ_D notes the Debye screening mass and ω_0 stands for the effective screening parameter, caused by the surrounding medium³. In the nominator of the ratio, the sign of exponent is just defined with 'minus' and does not play any role due to absolute squaring the vertex in calculating radiation amplitudes.

³Unusually, we consequently assign the intermediate gluon with an effective gluon mass ω_0 which expresses as an additional term in the denominator of Eq. (D.1) as well.

Appendix E Scalar QCD versus Spinor Calculation

The radiation amplitude, as a basic feature of calculating radiative energy loss, is derived with the help of spinor Feynman rules. If we investigate the general process of quark-quark scattering there exist sixteen different possibilities for spin configurations. The spin of the initial states for projectile and target quarks has to be compared with the final projectile and target spin; that is due to the possible spin flip for up and down states of the quarks. Computations with the program package of those spin flip effects were accomplished and it shows absolutely no effect compared with the scalar results, only in the scattering of two light or two heavy quarks with high energies, small momentum transfers and soft gluon radiation [Tho03]. The other case of light projectiles and heavy targets and vice versa yields a small dependence of the gluon emission angle ϑ in the summed and averaged squared total matrix element of the gluon radiation process. Of course, this effect also accounts for the integration over the gluon emission angles φ and ϑ at last for obtaining the radiative energy loss, but our focus is more on kinematical effects than taking into consideration spin flips in addition. The latter ones opens a door for further interesting investigations.

The whole calculation of matrix elements becomes much more complicated by accounting spinor rules, analytical derivations as well as numerical ones, compared with the results from scalar QCD. Finally because of this, we use scalar computations for the sake of the enormous time reduction in the working process of the numerical code, despite the fact that our program is powerful enough to deal with spinor rules.

Appendix F General Aspects of Gauges

Physical quantities have to be independent of gauge parameters. The calculation of quark energy loss basically uses the total summed and squared matrix element¹. Therefore we have to specify the gluon field operator $\hat{A}^\mu(x)$, respectively the not quantised field mode $A^\mu(x)$ for solving the wave equation

$$(\square + \omega_0^2) = 0, \tag{F.1}$$

derived from the Lagrangian of the Proca theory. This relation holds only for massive gluon fields with the Lorentz condition $\partial_\nu A^\nu = 0$ following from current conservation. Hence, the vector field reads as²

$$A^\mu(\vec{k}, \lambda, x) = N \epsilon^\mu(\vec{k}, \lambda) e^{-ikx}, \tag{F.2}$$

separated in planar waves. The four-dimensional transversal condition $\epsilon_\sigma k^\sigma = 0$ is obeyed automatically.

Now, the attention is on polarisation vectors in a manner of various polarisation modes. Gupta and Bleuler derived a quantisation method to cancel longitudinal and scalar polarisation modes. This formalism is based on expectation value of physical states with operator relations as

$$\langle \Phi | \partial^\mu \hat{A}_\mu(x) | \Phi \rangle = 0. \tag{F.3}$$

But the cancelling of longitudinal and scalar modes of observable gluons is not valid for intermediate³ (non-observable) gluons!

Massless gluons have only two transverse polarisation modes, but in the real massive case, which is not consequently realised in our consideration as an effective gluon mass parameter, one additional transverse polarisation appears (cf. [Gre93]).

F.1 Gauge Invariance for Polarisation Vectors

Because of Eq. (F.1) the plan wave solution (F.2) is not fixed by the Lorentz condition. Thus, we add a local gauge transformation $\Lambda(x)$ in the following manner

$$A'^\mu(x) = A^\mu(x) + \partial^\mu \Lambda(x) \tag{F.4}$$

¹It is a noteworthy fact that only the total matrix element obeys gauge invariance. Single amplitude contributions do not behave like this.

²Here, we neglect colours by treating gluons. Thus, these relations hold also for 'massive' photons ($k^2 \neq 0$).

³A formal introduction of ghost field terms in the Lagrangian cancel internal contributions forming non-transverse gluons.

obeying the homogeneous wave equation

$$\square\Lambda = 0. \quad (\text{F.5})$$

Any solution of (F.5) as $\Lambda \sim e^{-ikx}$ appears a new degree of freedom for a modification of the four-dimensional polarisation vectors

$$\epsilon'^{\mu} = \epsilon^{\mu} + \beta k^{\mu} \quad (\text{F.6})$$

with an arbitrary parameter β .

Henceforth, three different gauge conditions with respect to polarisation vectors are considered:

- $A^0 = 0$ gauge,
- $A^- = 0$ gauge,
- $A^+ = 0$ gauge.

The nature of gauge invariance is that physical observable remain invariant. For the total matrix element Fig. C.3(b) this is exhibited in [Tho05].

Here, we take our focus on the A^+ gauge. In order to compare quark-quark scattering with the potential model, target radiation can be neglected in contrast to projectile- and three-gluon contributions, as shown in [Gun82, Wan95]. This raises the A^+ gauge to our favourite class of Lorentz gauge.

The polarisation vectors follow in light-cone coordinates as

$$\epsilon^{1/2} = (\epsilon_0, \vec{\epsilon}_{\perp}^{(1/2)}, -\epsilon_0) \quad \text{with} \quad \vec{\epsilon}_{\perp}^{(1)} \cdot \vec{\epsilon}_{\perp}^{(2)} = 0. \quad (\text{F.7})$$

The transformation (F.10) allows additional conditions for gluon polarisations, given by

$$\left. \begin{aligned} \epsilon^{(j)} k &= 0 \\ \{\epsilon^{(j)}\}^2 &= -1 \end{aligned} \right\} \quad j = 1, 2. \quad (\text{F.8})$$

An implementation of the transverse condition and the gluon momentum k^{μ} yields

$$\epsilon_0^{(j)} = \frac{\vec{\epsilon}_{\perp}^{(j)} \vec{k}_{\perp}}{k_0 + k_z}. \quad (\text{F.9})$$

For completeness we note the expressions $\epsilon^{(1)}$ and $\epsilon^{(2)}$ in used spherical coordinates,

$$\epsilon_0^{(1)} = \left(\frac{\omega \cos \varphi \sin \vartheta}{2Ex}, 1, 0, -\frac{\omega \cos \varphi \sin \vartheta}{2Ex} \right), \quad (\text{F.10})$$

$$\epsilon_0^{(2)} = \left(\frac{\omega \sin \varphi \sin \vartheta}{2Ex}, 0, 1, -\frac{\omega \sin \varphi \sin \vartheta}{2Ex} \right) \quad (\text{F.11})$$

with

$$\vec{\epsilon}_{\perp}^{(1)} = (1, 0) \quad \text{and} \quad \vec{\epsilon}_{\perp}^{(2)} = (0, 1) \quad (\text{F.12})$$

as the transverse polarisations to be employed in the numerical calculations.

A possible singularity problem for backward gluon emission ($\vartheta \rightarrow \pi$) is screened by an effective gluon mass ω_0 in the denominator of expression (F.9), discussed in detail in Section 2.5.

F.2 Linear and Circular Polarisations

The introduction of an object consisting of various possible gluon polarisation states describes various degrees of polarisations. Thus, the polarisation matrix with three real so-called Stokes parameters ξ_1 , ξ_2 and ξ_3 is given by

$$\rho_{\alpha\beta} = \frac{1}{2} \begin{pmatrix} 1 + \xi_3 & \xi_1 - i\xi_2 \\ \xi_1 + i\xi_2 & 1 - \xi_3 \end{pmatrix} \quad \text{with} \quad -1 \leq \xi_i \leq 1. \quad (\text{F.13})$$

The gluon polarisation states are combined to the parameters ξ_i like

$$\xi_1 = \begin{cases} 1 & \text{linear polarisation vector} & \epsilon^{(+)} = \frac{1}{\sqrt{2}}(\epsilon^{(1)} + \epsilon^{(2)}), \\ -1 & \text{linear polarisation vector} & \epsilon^{(-)} = \frac{1}{\sqrt{2}}(\epsilon^{(1)} - \epsilon^{(2)}), \end{cases} \quad (\text{F.14})$$

$$\xi_2 = \begin{cases} 1 & \text{circular polarisation vector} & \epsilon^{(+)} = -\frac{i}{\sqrt{2}}(\epsilon^{(1)} + i\epsilon^{(2)}), \\ -1 & \text{circular polarisation vector} & \epsilon^{(-)} = -\frac{i}{\sqrt{2}}(\epsilon^{(1)} - i\epsilon^{(2)}), \end{cases} \quad (\text{F.15})$$

$$\xi_3 = \begin{cases} 1 & \text{linear polarisation vector} & \epsilon^{(1)}, \\ -1 & \text{linear polarisation vector} & \epsilon^{(2)}. \end{cases} \quad (\text{F.16})$$

Using the projection

$$p_{(e)} = \epsilon^\dagger \rho \epsilon \quad (\text{F.17})$$

as a description of a probability for special polarisations yields

$$\begin{aligned} p_{(1)} &= \epsilon^{(1)\dagger} \rho \epsilon^{(1)}, & p_{(2)} &= \epsilon^{(2)\dagger} \rho \epsilon^{(2)}, \\ p_{(+)} &= \epsilon^{(+)\dagger} \rho \epsilon^{(+)}, & p_{(-)} &= \epsilon^{(-)\dagger} \rho \epsilon^{(-)}, \end{aligned} \quad (\text{F.18})$$

implemented directly in the numerical calculations.

Due to the summed and averaged squared matrix elements in calculating gluon radiation spectra the result is shown to be invariant by a comparison between linear and circular polarisations⁴ (see Fig. C.5 in [Dok01]). The sum of each ratio pair of different polarisation contributions equals one.

F.3 Gauge Invariance of the Gluon Propagator

The internal gluon propagator is given by

$$iD(k)^{\mu\nu} = \frac{-i}{k^2 - \omega_0^2 + i\epsilon} \left(g^{\mu\nu} - (1 - \lambda) \cdot \frac{k^\mu k^\nu}{k^2 - \lambda\omega_0^2 + i\epsilon} \right) \quad (\text{F.19})$$

according to the proper Feynman-Stueckelberg Lagrangian ([Itz80, Gre93]). The gauge fixing term in the propagator introduces a gauge parameter λ , called Feynman gauge for $\lambda = 1$ and Landau gauge for $\lambda = 0$. It is possible to cover λ with arbitrary amounts, but this two special cases named historically pursue to simpler expressions in propagators.

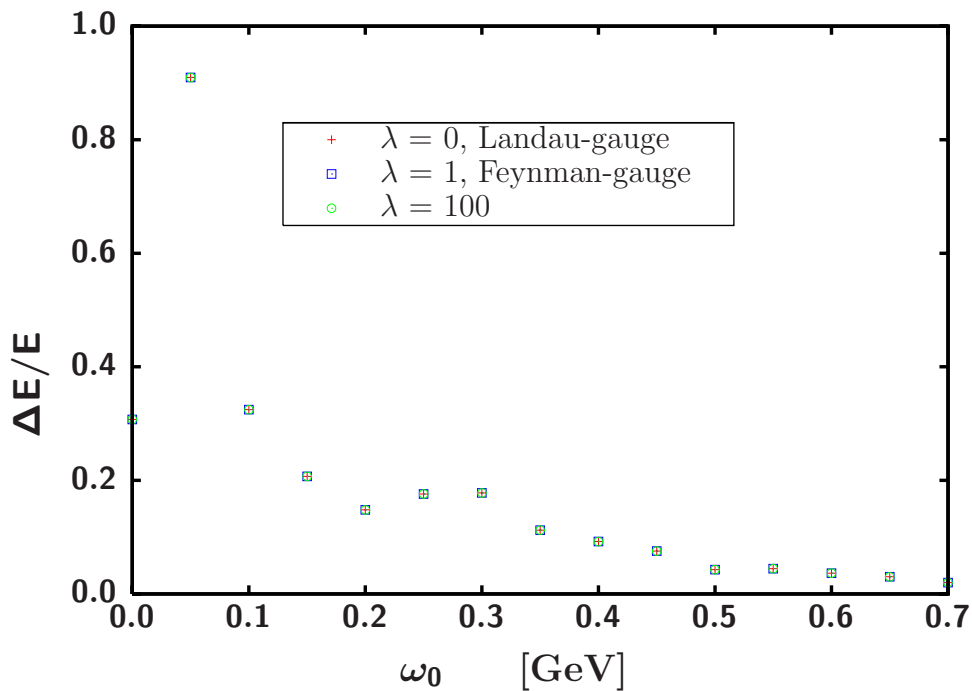


Figure F.1: The fractional energy loss for different gauge parameters λ is sketched as a function of the screening parameter ω_0 . As expected, one can verify no dependency of the gauge parameter λ for the relative charm quark energy loss.

For simple elastic quark-quark scattering one can show the disappearance of the gauge term proportional to $k^\mu k^\nu$ due to Dirac equation (B.10) for spinors u and \bar{u} (see also Section 6.1.3 in [Itz80]). Please note that for spinor calculations one obtains nearly the same results as shown in Fig. F.1.

⁴The same results yield by including spinor rules.

Appendix G Numerical Integration and C++ Code

In the following we give a short description of the structure of the numerical C++ program, which calculates the radiation amplitudes and integrates the gluon distribution over several phase space areas.

In general, the program calculates the gluon emission amplitudes for different single scattering scenarios in medium as described in Chapter 3.

Besides the variable kinematical parameters and an effective gluon mass as input parameters of the scattering processes, it is possible to evaluate matrix elements in different gauges (A^+ , A^- or A^0). Therefore, the fundamental Feynman diagrams of involved vertices are implemented. The code uses as basic objects three dimensional complex matrices for Gell-Mann matrices used for colour algebra and four dimensional matrices needed for the spinor algebra. It has also built in complex column and row vectors of same dimensions together with rules of matrix multiplication and the right behaviour of complex numbers. For all numerical calculations we take the exact kinematics into account. In general, one has to make a decision whether a calculation is performed in scalar or spinor QCD. Additionally, for some numerical tests of kinematics, on-shell and gauge conditions are introduced check boundaries on a global level.

Here, the code is aimed at avoiding the approximations of analytical or semi-analytical approaches, like in [Sor06, Bai06, Kid06]. We do not discuss technical aspects of our program in detail, but for the interested reader and the sake of reproducibility some explanations for calculations of the gluon distribution are displayed in Appendix F of [Vit05].

Now, we consider the numerical integration part. First of all one has to select an appropriate integration method. One aspect, despite some technical ones, is important in this context: What is the intrinsic statistical error of the technique and how fast converges the integration method? In general we have the choice between two different methods. On the one hand the traditional separation of integration area in simple geometric objects, on the other hand a modern integration technique, like Monte Carlo (MC)-integration with all its different versions. We choose the latter one and give a short overview of this technique in the following.

First we pick N random points x_1, \dots, x_N being uniformly distributed in a multidimensional volume V . The procedure of MC integration estimates the integral of an arbitrary function f over the multidimensional volume

$$\int f dV \approx V \langle f \rangle \pm V \sqrt{\frac{\langle f^2 \rangle - \langle f \rangle^2}{N}} \quad (\text{G.1})$$

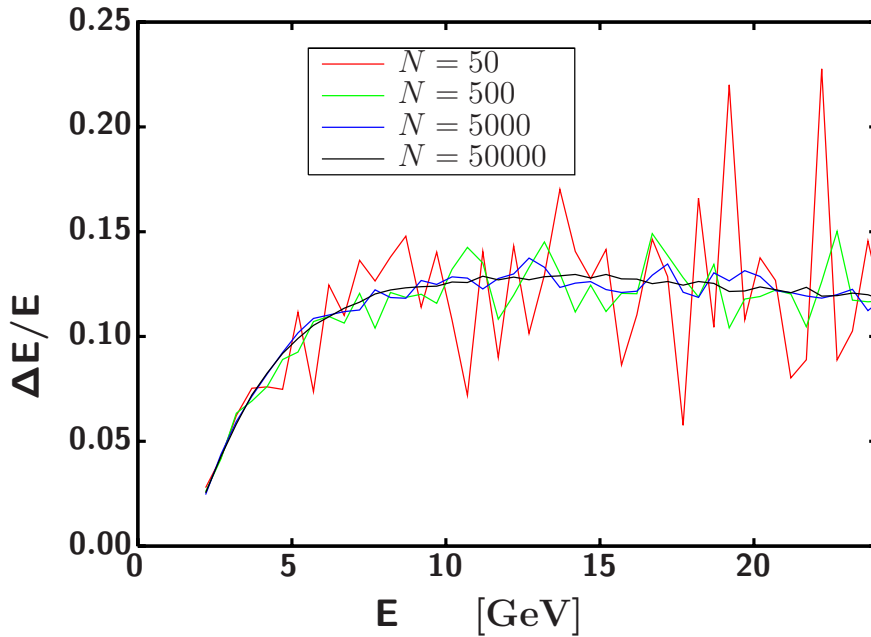


Figure G.1: Accuracy calculation of the relative radiative energy loss for quark-quark scattering with increasing N : 50 (red line), 500 (green line), 5000 (blue line) and 50000 (black line); error estimates decrease rapidly as $1/\sqrt{N}$ for MC integration methods.

with taking an arithmetic mean over N sample points according to

$$\langle f \rangle \equiv \frac{1}{N} \sum_{i=1}^N f(x_i) \quad \text{and} \quad \langle f^2 \rangle \equiv \frac{1}{N} \sum_{i=1}^N f^2(x_i). \quad (\text{G.2})$$

If one interprets the multidimensional volume in terms of the phase space (e.g. in 3D spherical coordinates) the volume integral looks like¹

$$\int f dV = \int_{\varphi_1}^{\varphi_2} d\varphi \left[\int_{\vartheta_1}^{\vartheta_2} d\vartheta \left\{ \int_{\omega_1}^{\omega_2} d\omega \tilde{R}(f_1(\varphi), f_2(\vartheta), f_3(\omega)) \right\} \right]. \quad (\text{G.3})$$

It is an incontestable fact that for multidimensional integrations the calculation time grows up dependent the number of a dimensions. Fortunately, the error estimate of MC integration decreases as $1/\sqrt{N}$ what makes a big advantage compared to conventional integration methods. There the calculation time explodes exponentially with the space dimension contrary to MC integration. With some more complicated extensions of the MC method it should be possible to break the 'barrier' of $1/\sqrt{N}$, hence gets higher accuracy.² This aspect is shown in Fig. G.1 for an increasing number of random points.

For all MC calculations a uniform distribution of the phase space points is absolutely indispensable. Thus, a random generator producing highly non-correlated numbers is necessary. We use an appropriate generator from Numerical Recipes [NUM88].

¹This is only a simplified performance of the integration over phase space. The true multidimensional integral is given in Eq. (4.19).

²Our method is precisely called simple MC integration. Unfortunately, the more accurate MC method with importance sampling is not useful due to the analytical ignorance of the integrand function \tilde{R} .

Bibliography

- [Ada06] J. Adams *et al.* [STAR Collaboration], arXiv:nucl-ex/0601042.
- [Adl06a] S.S. Adler *et al.* [PHENIX Collaboration], *Phys. Rev. Lett.* **96** (2006) 032301.
- [Adl06b] S.S. Adler *et al.* [PHENIX Collaboration], *Phys. Rev. Lett.* **96** (2006) 032001.
- [Adl06c] S.S. Adler *et al.* [PHENIX Collaboration], arXiv:nucl-ex/0601037.
- [Adi06] A. Adil, M. Gyulassy, W. Horowitz, S. Wicks, arXiv:nucl-th/0606010.
- [Akh96] A.I. Akhiezer, N.F. Shul'ga, *High-Energy Electromagnetics in Matter*, Gordon and Breach Publishers, Luxembourg, 1996.
- [Ala06] J. Alam, A.K. Dutt-Mazumder, P. Roy, arXiv:nucl-th/0608058.
- [Bai98] R. Baier, Yu.L. Dokshitzer, A.H. Mueller, D. Schiff, *Phys. Rev.* **C58** (1998) No.3.
- [Bai06] R. Baier, D. Schiff, arXiv:hep-ph/0605183.
- [Bie05] J. Bielcik *et al.* [STAR Collaboration] arXiv:nucl-ex/0511005.
- [Djo03a] M. Djordjevic, M. Gyulassy, *Nucl. Phys* **A733** (2003) 265 [arXiv:nucl-th/0310076].
- [Djo03b] M. Djordjevic, M. Gyulassy, *Phys. Rev.* **C68** (2003) 034914.
- [Djo06b] M. Djordjevic, arXiv:hep-ph/0603066.
- [Dok01] Yu.L. Dokshitzer, D.E. Kharzeev, *Phys. Lett.* **B519** (2001) 199 [arXiv:hep-ph/0106202].
- [Dok06] Yu.L. Dokshitzer, F. Fabbri, V.A. Khoze, W. Ochs, *Eur. Phys. J.* **C45** (2006) 387.
- [Gal64] V.M. Galitsky, I.I. Gurevich, *Il Nuovo Cimento*, (1964) 396.
- [Gal01] K. Gallmeister, B. Kämpfer, O.P. Pavlenko, *Phys. Rev.* **C66** (2002) 014908 [arXiv:hep-ph/0101095].
- [Gre93] W. Greiner, J. Reinhardt, Theoretische Physik, Band 7A, *Feldquantisierung*, Verlag Harri Deutsch, Frankfurt am Main, 1993.

- [GSI1] Gesellschaft für Schwerionenforschung, GSI, <http://www.gsi.de>
- [Gun82] J.F. Gunion, G. Bertsch, *Phys. Rev.* **D25** (1982) 746.
- [Gyu94] M. Gyulassy, X.N. Wang, *Nucl. Phys.* **B420** (1994) 583 [arXiv:nucl-th/9306003].
- [Gyu00a] M. Gyulassy, P. Lévai, I. Vitev, *Phys. Rev. Lett.* **85** (2001) 26.
- [Gyu00b] M. Gyulassy, P. Lévai, I. Vitev, *Phys. Rev. Lett.* **B571** (2000) 197.
- [Gyu01] M. Gyulassy, P. Lévai, I. Vitev, *Nucl. Phys.* **B594** (2001) 371 [arXiv:nucl-th/0006010].
- [Gyu02] M. Gyulassy, P. Lévai, I. Vitev, *Phys. Lett.* **B538** (2002) 282.
- [Itz80] C. Itzykson, J.B. Zuber, *Quantum Field Theory*, Advanced Book Program, Saclay, 1980.
- [Jac98] J.D. Jackson, *Classical Electrodynamics, 3rd ed.*, Wiley-Interscience, New York, 1998.
- [Käm00] B. Kämpfer, O.P. Pavlenko, *Phys. Lett.* **B477** (2000) 171.
- [Kid06] N. Kidonakis, arXiv:hep-ph/0606280.
- [Kin62] T. Kinoshita, *J. Math. Phys.* (1962) 650.
- [Kov03] A. Kovner, U.A. Wiedemann, arXiv:hep-ph/0304151.
- [Lan86] L.D. Landau, E.M. Lifschitz, *Lehrbuch der theoretischen Physik*, Bd. IV, Quantenelektrodynamik, Akademie-Verlag, Berlin, 1986.
- [Lee64] T.D. Lee, M. Nauenberg, *Phys. Rev.* **133** (1964) B1549.
- [Mig56] A.B. Migdal, *Phys. Rev.* **103** (1956) 1811.
- [Mül99] W. Müller, *Untersuchungen zum Landau-Pomeranchuk-Migdal-Effekt in QED und QCD*, Diplomarbeit, Dresden, 1999.
- [Mus97] M.G. Mustafa, D. Pal, D.K. Srivastava, M. Thoma, *Phys. Lett.* **B428** (1998) 234 [arXiv:nucl-th/9711059].
- [Mus05] M.G. Mustafa, *Phys. Rev.* **C72** (2005) 014905.
- [NUM88] *Numerical Recipes in C: The Art of Scientific Computing*, Cambridge University Press, 1988.
- [Pav97] O.P. Pavlenko, copies of a talk at the Forschungszentrum Rossendorf, 1997.
- [Pes06] A. Peshier, arXiv:hep-ph/0605294.
- [Pro06] G.M. Prosperini, M. Raciti, C. Simolo, arXiv:hep-ph/0607209.

- [Sor06] P. Sorensen, X. Dong, arXiv:nucl-th/0512042.
- [Ter72] M.L. Ter-Mikaelian, *High-energy electromagnetic processes in condensed media*, Wiley-Interscience, New York, 1972.
- [Tho03] R. Thomas, *Energy Loss of Quarks by Gluon Radiation in Deconfined Matter*, Diplomarbeit, Dresden, 2003.
- [Tho05] R. Thomas, B. Kämpfer, G. Soff, *Acta Phys. Hung.* **A22** (2005) 83.
- [Vit05] I. Vitev, *Phys. Lett.* **B630** (2005) 78 [arXiv:hep-ph/0501255].
- [Wan95] X.N. Wang, M. Gyulassy, M. Plümer, *Phys. Rev.* **D51** (1995) 3436 [arXiv:hep-ph/9408344].
- [Wic06] S. Wicks, W. Horowitz, M. Djordjevic, M. Gyulassy, arXiv:nucl-th/0512076.
- [Wie00] U.A. Wiedemann, *Nucl. Phys.* **B588** (2000) 303 [arXiv:hep-ph/0005129].
- [Wie05] U.A. Wiedemann, *et al. Phys. Rev.* **D71** (2005) 054027.
- [Wie06] U.A. Wiedemann *et al.*, *Phys. Lett.* **B637** (2006) 362.
- [Xia04] W.C. Xiang, H.T. Ding, D.C. Zhou, *Chin. Phys. Lett.* **2** (2005) Vol.22.
- [Zak98] B.G. Zakharov, *Phys. Atom. Nucl.* **61** (1998) 838.

Danksagung

Hiermit bedanke ich mich bei Herrn Prof. Dr. R. Schmidt für die Aufnahme in das Institut für Theoretische Physik und die damit verbundene Möglichkeit, die Thematik zu bearbeiten.

Desweiteren gilt mein Dank insbesondere Herrn Prof. Dr. Burkhardt Kämpfer für die Bereitstellung des interessanten Aufgabengebietes dieser Arbeit und die freundliche Aufnahme in seine Arbeitsgruppe. Die intensive Betreuung sowie eine Reihe von Gestaltungsvorschlägen und motivierender Gespräche prägten das Gesamtbild dieser Arbeit nachhaltig.

Besonders danken möchte ich auch Dipl. Phys. Ronny Thomas für die vielen anregenden und fruchtbaren Diskussionen, vor allem aber für die Bereitstellung seines numerischen Codes.

Schließlich danke ich Ronny, Marcus, Daniel, Thomas und Robert für ihre Unterstützung und ihre zahlreichen inspirierenden sowie motivierenden Worte, besonders in schwierigen Phasen dieser Diplomarbeit.

Selbständigkeitserklärung

Ich erkläre, die vorliegende Arbeit selbständig und ohne die unzulässige Hilfe Dritter angefertigt zu haben. Dabei wurden nur die von mir explizit angegebenen Hilfsmittel verwendet. Alle aus fremden Quellen direkt oder indirekt übernommenen Gedanken sind als solche gekennzeichnet. Die Arbeit wurde bisher weder im Inland noch im Ausland in gleicher oder ähnlicher Form bei einer anderen Prüfungsbehörde eingereicht.

Dresden, den 9. Oktober 2006

Henry Schade